Controlling the air-water behavior of phenolic surfactants and their ω-thiolated derivatives using subphase modification: towards deposition of functional thin films.

Renaud Miclette Lamarche

A Thesis
In the Department
of
Chemistry and Biochemistry

Presented in Partial Fulfillment of the Requirements
for the Degree of
Doctor of Philosophy (Chemistry) at
Concordia University
Montréal, Québec, Canada

December 2019

CONCORDIA UNIVERSITY

School of Graduate Studies

This is to certify that the thesis prepared

By: Renaud Miclette Lamarche

Entitled: Controlling the air-water behavior of phenolic surfactant and their ω-thiolated derivatives using subphase modification: towards deposition of functional thin films.

and submitted in partial fulfillment of the requirements for the degree of

Doctor Of Philosophy (Chemistry)

complies with the regulations of the University and meets the accepted standards with respect to originality and quality.

Signed by the final examining committee:

_____ Chair
Dr. Selvadurai Dayanandan

_____ External Examiner
Matthew Paige

_____ External to Program
Pablo Bianucci

_____ Examiner
Heidi Muchall

_____ Examiner
Cameron Skinner

_____ Thesis Supervisor
Christine DeWolf

Approved by _____
Chair of Department or Graduate Program Director

January 16 2020 _____
Dr. André Roy, Dean Faculty of Arts and Science

ABSTRACT

Controlling the air-water behavior of phenolic surfactants and their ω-thiolated derivatives using subphase modification: towards deposition of functional thin films.

Renaud Miclette Lamarche, Ph. D.

Concordia University, 2019

Polyphenolic compounds have the ability to selectively bind metals and certain proteins, properties that can be harnessed for sensing applications. Their analyte binding affinity is partially influenced by the proximity and conformational freedom of the individual phenol moieties. This makes the ability to control the organization of phenol groups an important consideration for the development of phenolic-functionalized thin film coatings. We investigated the approach of using a Langmuir monolayer, pre-organized at the air-water interface to control the lateral spacing upon deposition onto a solid surface. The self-assembly of phenolic surfactants is determined by the strong headgroup interactions: the hydroxyl groups can hydrogen bond with neighboring phenols and the aromatic ring can form π-interactions. We find that the strong, directional interactions lead to the creation of very rigid films that we attribute in large part to the presence of an organized and crystalline phenol headgroup layer. Modification of the subphase pH caused deprotonation of the phenol hydroxyls, which disrupt the organization of the monolayer in two ways: first by increasing the inter-domain charge repulsion and, at high pH, by disrupting the hydrogen bond network yielding a new lateral organization.

In order to deposit the film onto solid support for chemisorb to the surface using gold-thiol chemistry, an ω-thiolated phenolic surfactant was used. The impact of the ω-thiolation on the

behavior of the phenol film was investigated. The thiol-terminated surfactant initially forms a film with the same structure and organization as the methyl-terminated surfactant but this phase was found to be metastable and convert to a bent conformation, with both the phenol and the thiol tethered to the water surface, over time. The rate of this interconversion between the condensed phase and bent phases could be controlled using the subphase pH, however high pH can also induce multilayer formation. We demonstrated that spreading the film over a subphase that contains binding analytes of interest, such as poly-L-proline and copper ions, can be used as a strategy to pre-organize the surfactants into the optimal lateral spacing for subsequent binding.

ACKNOWLEDGEMENTS

I am extremely grateful to my supervisor, Dr. DeWolf, for accepting me as a student and for her constant support and discussion throughout the years. I am particularly grateful for the immense amount of time she spend reading and re-reading what might generously have been called my writing and for adding all those pesky “s” that were missing.

I would not be the researcher and experimentalist I am today if it was not for the counsel of Dr. Rolf Schmidt, every aspect of my research depended on him in some way (including the template for this thesis). I have no idea how I would have made any of it without his help.

My committee member, Dr. Heidi Muchall and Dr. Cameron Skinner for supporting and reviewing my work over years and teaching me as undergraduate student.

This work is the continuation of previous member of our group, including Arison Rajasingam and Ying Zhao and many others. It will continue through the work of Janet Gaba and hopefully many others.

Many people helped me throughout my research. Dr Wei Bu and Dr. Binhua Lin, beamline scientist at APS, were instrumental in the gathering and analysis of the X-ray data, I thank them for their patience in answering my innumerable questions. Violetta Toader for synthesizing the ω-terminated surfactant, saving me years of work. Eric Dionne, from Antonella Badia group, for his help with various technique and for donating some gold for my research.

I thank everyone that has worked in our lab and become friends, including but not limited to Abdullah, Daisy, Erum, Hala, Janet, Javier, Jennifer, Jocelle, Sahana, Ruxandra, Shirin. Labs are first and foremost made of the community that work in them, ours would not have been the same without them and I hope our new students, Dalia and Mashid, will create one just has wonderful to work in.

Finally I thank my family for supporting me, after a long time of telling them I was almost done, I am now done.

Contribution of authors

Author contributions: I conducted all of the experimental work, data analyses, and prepared the manuscript. My supervisor, C. DeWolf, assisted with experimental design, data interpretation and manuscript writing.

Chapter 2 provides an overview of the techniques used in this thesis. Chapter 3 was published as R. Miclette Lamarche and C. DeWolf, Strong Headgroup Interactions Drive Highly Directional Growth and Unusual Phase Co-Existence in Self-Assembled Phenolic Films, *ACS Applied Materials and Interfaces*, 2019, 11 (48) 45354-45363 (doi: 10.1021/acsami.9b16958). Chapter 4 is currently under review. It has been submitted to *Langmuir* as R. Miclette Lamarche and C. DeWolf, ω-Thiolation of phenolic surfactants enables controlled conversion between extended, bolaform and multilayer conformations, (Manuscript ID: la-2019-03670g). Chapter 5 will be submitted to *Langmuir* as R. Miclette Lamarche and C. DeWolf, Phenolic monolayers exhibit strong binding with copper and proline causing chain-independent re-organization of the headgroups. All three manuscripts comprise data collected and analyzed by me and were co-written by myself and my supervisor.

Table of Contents

List of Figures

List of Tables

List of Abbreviations

AFM	atomic force microscopy
BAM	Brewster angle microscopy
DPPC	dipalmitoylphosphatidylcholine
FWHM	full width at half maximum
GIXD	grazing incidence X-ray diffraction
LB	Langmuir-Blodgett
LDG	lauryl gallate
LDGSH	12-sulfanyldodecyl 3,4,5-trihydroxybenzoate
LE	liquid expanded
MD	molecular dynamics
Nd:YAG	neodymium-doped yttrium aluminum garnet
NN	nearest neighbor
NNN	next nearest neighbor
ODG	octadecyl gallate
ODG SH	18-mercaptooctadecyl 3,4,5-trihydroxy benzoate
PPII	poly-proline II helix
QCMD	quartz crystal microbalance
SAM	self-assembled monolayer
GISAXS	grazing incidence small-angle x-ray scattering

SPR	surface plasmon resonance
XPS	x-ray photoelectron spectroscopy
TRXF	total reflection x-ray fluorescence

Chapter 1. Introduction

1.1. Motivations

Tannins exhibit antioxidant, protein binding and metal chelating properties[1,2], key to their behavior are the phenol moieties (Figure 1-1). Tannins are also well known for having specificity toward binding proline-rich and histidine-rich proteins[3,4], which contributes to the astringent sensation experienced when consuming wine. It is thought that one of the roles of tannins in plants is a form of dietary defense against herbivores since the precipitation caused by tannins deactivates some of the proteins present in saliva necessary for digestion thus limiting the absorption of both proteins and iron containing compounds[5]. In turn, herbivores secrete proteins and peptides that have a strong affinity for polyphenols, by for example being rich in proline, to counter this and overwhelm the phenols. These proline rich proteins have also been linked to various diseases, such as diabetes[6], caries[7] and cancer[8] and due to their large presence in saliva, make for an attractive biosensor target since saliva is an easily accessible, although complex, biological matrix and collecting it is less invasive than drawing blood. Furthermore, their large presence in saliva can also impede the detection of other proteins, therefore an easy way to selectively remove them from a sample is an attractive alternate use.

1.2. Polyphenol protein binding

When small molecules possessing only a single phenol moiety interact with proline rich protein they tend to bind to every exposed proline. The strength of that binding is weak but it tends to be strongest when the proline residue is immediately followed by another proline[9]. As the size and complexity of the

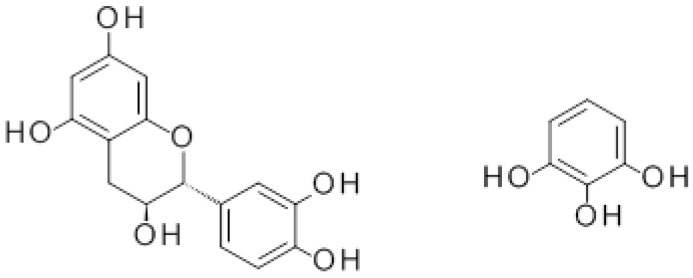

Figure 1-1 Examples of phenols, catechin and pyrogallol

polyphenol increase the number of binding site tends to go down; this is due to the increasing steric hindrance constraining the polyphenol from properly interacting with most proline sites. Larger polyphenols therefore bind to specific sites and, if the number of binding sites is quantified, it tends to be

similar to the number of locations with multiple prolines in close proximity[10]. Though the number of sites decreases, the strength of the interaction with the few proline rich sites still capable of accommodating the polyphenol increases[9]. When one of the phenol moiety binds to a proline, in a proline rich site, it causes the other nearby phenols moieties to be in close proximity to the nearby proline, leading to cooperative binding, see Figure 1-2 for example. This however depends on the other phenols being able to properly orient themselves[11] without being obstructed for steric reasons, either by other nearby amino acid or part of the polyphenol.

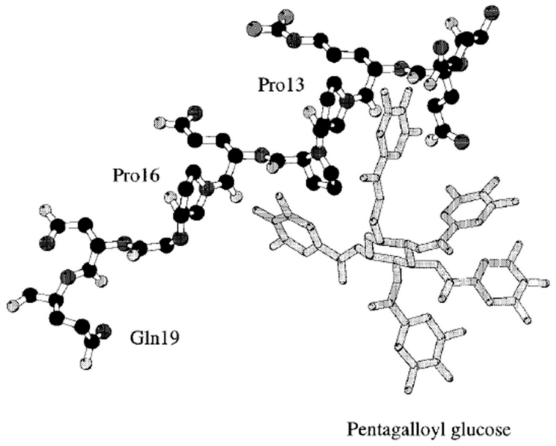

Figure 1-2 Binding interaction between a polyphenol and a proline rich site, from ref[9]

Phenol affinity for proline arise from many possible interactions, both hydrophobic and hydrophilic[11,12], but also because of their ability to disrupt the formation of helix structure[13], which makes binding to the resulting extended conformation easier for polyphenol. Other nearby residues in the protein can also contribute to a stronger bonding even in proline rich protein, for example, arginine is often found in an adjacent or nearby position to the proline and strengthens the overall binding of the proline-rich protein with a phenol by hydrogen bonding to the π system of a phenol ring[14,15]. Furthermore, these conditions also exist for other residues and polyphenol can also form strong bond with histidine[16] rich protein.

1.3. Polyphenol-metal ions binding

Similarly to proteins, polyphenol metal binding has accrued attention because of their influence on nutrient absorption[17], it is also considered for removal of metal contaminants[18]. They also help limit oxidative damage by chelating metal species in vivo[19], limiting the damage they can do. Tannins have

good affinity for a variety of metals[2], but still display selectivity and different polyphenols will have different affinities[20]. The ability of polyphenol to bind metals comes from the close proximity of the hydroxyl groups, as such a phenol moiety with a single hydroxyl, cannot bind a metal, multiple hydroxyls are needed[21]. The planarity of the phenolic moieties, due to the presence of the aromatic ring, also help the binding by positioning the hydroxyl in the right orientation for multidentate binding. Binding to metals can take the form of binary complex[22] or ternary complex[21], with water occupying the other positions. This thesis will mostly contrast zinc and copper, which both can be found in the M^{2+} states, but nonetheless show different affinities. This has been attributed to the different complexes they adopt, zinc favoring tetrahedral and copper planar[23].

1.4. Exploiting the properties of phenols

It would be useful to transfer some of polyphenol properties onto solid support (to be discuss later) for further use in, for example, lab on a chip design[24]. But since those properties are dependent on the proximity and steric freedom of the phenol groups, any deposition technique would need to afford some control over the final organisation. One approach would be to control the distance by synthesizing polyphenols with specific arrangements, but synthesizing new molecules for every application would be time and resource consuming. Ideally, the surface coating would use the same phenolic building blocks but only change the transfer conditions as to obtain distinct surface organization and distance. To that end, an alternative method would be to control the intermolecular distance in self-assembled films using phenolic-derived building blocks. This thesis will mainly focus on tri-hydroxyl gallate single chain surfactant (see Figure 1-3) and their ω-thiol derivatives.

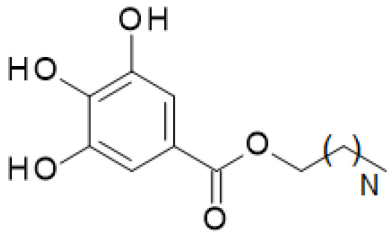

Figure 1-3 Gallate surfactant used throughout this thesis, N = 10 Lauryl gallate, N = 16 Octadecyl gallate

Lauryl gallate is notable because it is approved by the FDA (US Food and Drug Administration) and the World Health Organisation as an antioxidant additive for food. As such, a large body of research has been carried out with lauryl gallate and its analogues with different chain lengths, including octadecyl gallate and different hydroxyl substitution patterns. This includes research into their membrane binding properties[25], surface tension as a function of chain length[26], anti-cancer[27], anti-fungal[28], anti-bacterial[29], anti-viral[30] and, of course, anti-oxidant[31] abilities.

Furthermore, the air-water interface behavior of lauryl gallate has been studied, specifically its impact on phospholipid monolayers, often used as a model for biologically relevant membrane[32–36]. The research mainly focused on the modification of the phospholipid behavior and morphology. They have found that the lauryl gallate helps protect the film from oxidative damage due to its anti-oxidant properties. They also compared the impact of the phenolic surfactant on the monolayer to the impact of cholesterol, with the phenolic lipid being mostly located in a more fluid region and helping the different phospholipids to mix due to the smaller headgroup.

Our own group researched the air-water behavior of a double chain variant, DPGG[37], which formed highly rigid monolayers at the air-water interface. Subsequently, double chain variants with differences in the number and placement of the hydroxyl moieties have been studied and all showed high degree of aggregation at high molecular areas (nominally the gaseous phase)[38], highlighting the contribution of π-stacking.

1.5. Phenolic films on solid supports

Most of the previous work on phenolic films has concentrated on modifying the phenolic moiety and measuring the impact on the properties of the monolayer. For example, Taylor *et al.*[39] used single hydroxy substituted *meta*- or *para*-phenolic surfactants to study the effects of the position of the hydroxyl group on self-assembled monolayer (SAMs) formed using gold-thiol chemistry. They found that these structural isomers led to very different surface behavior. The *para*-hydroxyl surface was hydrophilic and showed an increased hydrophilicity as the pH was increased. In contrast, the *meta*- hydroxyl surface exhibited a hydrophobic surface that was almost unaffected by pH and had a much lower surface coverage. They attributed these differences to the orientation of the hydroxyl group, with the *para*-version being normal to the surface and the *meta*- version oriented into the monolayer or lying parallel to the surface.

This demonstrates well the versatility of the phenolic group. With both hydrophobic and hydrophilic moieties in the same structure and in close proximity, the behaviour can easily be altered with small changes in structure. Also, the rigidity and relative bulkiness of the ring allows for specific arrangement to be created and locked in place.

Differential binding as a function of the position of the hydroxyl moieties on a phenolic surfactant was also previously studied. Azmi *et al.*[40] showed that monolayer coatings of two ω-thiolated phenolic surfactants (3,4 dihydroxybenzene and 3,5-dihydroxybenzene surfactants) self-assembled on gold surfaces, showed different affinity toward phosphate groups using chemical force spectroscopy. The two SAMs had different pH dependences, i.e. different binding affinities for monoprotic and diprotic phosphate groups. In the case of the monoprotic phosphate, the phenol with two *meta*- hydroxyls (3,5-dihydroxybenzene) showed weaker interaction, attributed to its hydrogen bond with its SAM neighbor, thus lowering its capacity to hydrogen bond with the phosphate groups. This suggests that the binding interactions of the monolayer coating could be tuned by modifying the intermolecular distance, i.e. if the distance was increased, neighboring surfactants may no longer be capable of forming hydrogen bonds with each other increasing binding capacity. The interactions with the diprotic phosphate were more complex and pH dependent since deprotonation of the phenolic hydroxyls will lead to the formation of ion-dipole (O^- - HO) interactions, both between neighboring surfactant and between surfactant and phosphate. These charge-assisted hydrogen bonds are potentially stronger than hydrogen bonds[41] that occur at lower pH values. It is noted that this could also be exploited at the air-water interface by changing the subphase pH which will deprotonate some of the headgroup hydroxyls. Azmi *et al*. concluded that the monolayer comprising both *para*- and *meta*- hydroxyls (3,4-dihydroxybenzene) has a maximal attraction with phosphate at low pH (5) whereas the one with only *meta*-hydroxyls *(*3,5-dihydroxybenzene) exhibited a maximal attraction at high pH (10), attributed to the differences in phenol steric hindrance. Specifically, the *para*-hydroxyl is able to freely bind at all pH values and the strongest interaction occurs if one of the phosphate hydroxyl groups is deprotonated. On the other hand the *meta*-hydroxyls are involved in hydrogen bonding with their neighbors and therefore have little ability to bind with the phosphate until the phenols begin to deprotonate at higher pH values. This induces a re-organization due to the ion-dipole interactions between the neighboring phenols, the extent of which is limited by their chemical attachment to the substrate. It is therefore possible for some of the *meta*-hydroxyl to bind to the

phosphates as the film cannot maximize the potential of the inter phenolic interactions. This points to one of the potential problems that may encountered, namely if the phenolic surfactants bind too strongly within the film, they might be unable to strongly interact with the analyte of interest.

While this illustrates the attractive prospect of phenolic coating, it also demonstrates the potential problem with relying on modifying the phenolic compound structure, any modification will not only change the surface behavior but also the organisation once deposited, which may change the surface properties in an undesirable way. But the traditional way of forming self-assembled monolayers affords very little control over the resulting film. Zhao *et al.*[42] deposited phenolic films onto silicon substrates and then subsequently chemically modified the phenol group, replacing a methoxy with an hydroxyl group. This created a chemically distinct surface, yielding a different contact angle measurement. However when they compared the two surfaces bearing the same group but made through two different routes (direct deposition versus post deposition modification), these had distinct properties. The self-assembly route followed by chemical modification is limited by the necessity to use a building block that can be subsequently modified at the air-solid or liquid-solid interfaces.

Pre-organising the film at the air water interface prior to deposition is an attractive alternative, since it may allow different organisations to be reached with the same surfactant, i.e. without any synthetic modification. But, before any deposition can occur, the surface behavior of phenolic films need to be studied.

1.6. Phenolic films at the air water interface

There are few reports of phenolic monolayers at the air-water interface. The first report of monolayer film of phenolic surfactant found was published in 1923[43], they calculated a rough surface area of p-hexadecyl phenol to be 24 $Å^2$/molecule which indicates very close packing. Some work was later carried out on the azobenzene analogue of phenol[44], for potential applications in dye photosynthesis and adsorption. A more modern study was carried out by Peikert *et al.*[45], studying the effect of modifying the position of the hydroxyl group in phenolic surfactants at the air-water interface. They compared 1-(4-hydroxyphenyl)-octadecane (with a *para*-hydroxyl) and 1-(3,4-hydroxyphenyl)-octadecane (with both a *para*- and a *meta*-hydroxyl). They found that the additional hydroxyl impacted both the organization of the headgroup and as a result the chain organization, leading to an increased chain tilt angle at the air-

water interface. Based on X-ray measurements of the chain region, they proposed a corresponding model organization of the headgroups that was heavily influenced by the π-π interactions, with the aryl rings being in an edge-to-face organization, highlighting the importance of these interactions, in addition to hydrogen bonds and the hydrophobic/hydrophilic interaction. Their proposed model for close-packed headgroups was based solely on chain-chain packing constraints and headgroup bond lengths rather than direct X-ray evidence of the headgroup lattice organization. This may mean that the orientation order for a mono- and di-hydroxyphenol is not strong enough to restrict the free-rotation of the headgroup. Headgroup orientation and freedom of motion will be an important aspect of the organization to be studied, as the headgroup will need enough freedom to adopt an appropriate orientation to bind the desired analyte, yet too much conformational freedom may limit the specificity of the binding. If a headgroup possesses more than one *meta*-hydroxyl group there is the possibility of forming a hydrogen bond network (Figure 1-4) which can rigidify the headgroup arrangement and could prevent it from changing conformation, limiting its ability to bind to analytes.

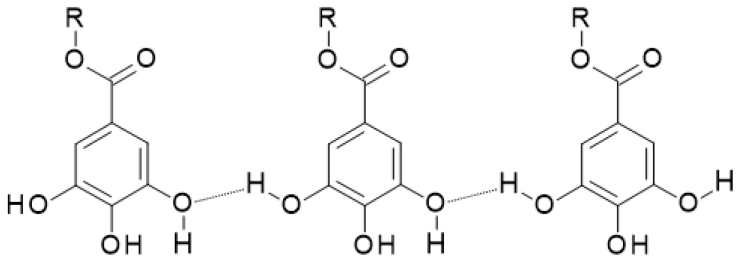

Figure 1-4 Hydrogen bond network example

1.7. Hydrogen bonding in monolayers

Inter-surfactant hydrogen bonding can have large effects on the behavior of the monolayer at the air water interface. Brezesinski *et al.*[46] studied an amine derived surfactant whose alkyl chain was untilted, i.e. perpendicular to the surface of the water. An untilted chain should not not favor a specific growth direction. Despite this the morphologies showed a strong linear tendencies, forming large dendritic domains at the surface of water, indicating that some aspect of the surfactant favor linear assemblies. They attributed this to hydrogen bonding between amine and carboxy group, forming large network, this was confirmed by IR spectroscopy. This strong tendency to hydrogen bond leading to the formation of large

linear assembly has also been observed for other systems[47,48]. Furthermore, hydrogen bonding is not limited to interactions between neighboring surfactants as the headgroups can also interact with species dissolved in the subphase, providing the interaction is strong enough to overcome the interaction with the water. For example nucleic acids interacting with surfactants derived from nucleic acids have been shown to reproduce base pair interactions at the air-water interface[49].

Subphase pH can also substantially modify the hydrogen bonding interactions present at the air-water interface. Once deprotonated, the headgroup hydrogen bonds can be replaced by ion dipole interactions which can be stronger. For example arachidic acid[50] was found to have the strongest inter-surfactant bonding at subphase pH of 9, which corresponds to a state when 50% of the headgroup would be deprotonated. Schultz *et al.*[51] studied the systemic modification of eicosanephosphonic acid behavior by subphase pH, such that its headgroup possesses 0, 1 or 2 charges both experimentally and computationally. Without a charge, the monolayer tends toward small circular domains, the result of line tension (2D equivalent of surface tension); these are visible both at the air-water interface and also through molecular dynamics studies. As the subphase pH is raised, inducing partial deprotonation, the surfactant initially tends toward a more packed system, contrary to what would be expected from the increase in charge repulsion. This was attributed to an increase in cohesive energy[52], most likely brought about by the increased interactions between neighboring surfactants due to replacing some hydrogen bonds by stronger ion-dipole interactions. But further increases, toward an average charge of 1+ lead to a less packed system. This also cause the appearance of dendritic domains, attributed to a reduction in line tension. Once the system is close to an average charge of 2+ there is a noticeable lack of long range ordering seen in the simulations, which agrees with the lack of domains seen at the air-water interface. This less ordered state is also visible in the z-direction, with the headgroups not aligning and instead shifting up or down from the plane of the monolayer to avoid charge-repulsion.

1.8. π-interactions in monolayers

Due to the presence of an aromatic ring in the phenol moiety, π-stacking interactions will affect the monolayer behavior. While the name may suggest that stacking interaction involves ring structure being aligned (sometime called sandwich conformation[53]), two other pairwise motifs are also recognized: the parallel displaced, where the rings are stacked but off-centered and the edge-to-face alignment, where

one of the rings is rotated so that the side of the ring interact with the face of the other ring (this orientation does not require a full 90° orientation and can results in partial rotation still being favorable[54]).

These interactions can greatly modify the organisation of the monolayer. For example, the self-assembled monolayer of anthracene derived molecule[55] shows a very strong tendency to orient in a way that maximizes the parallel displaced orientation when scanned using scanning electron microscopy. These tend to make a regular array of interdigitated rings, but when a group capable of forming strong hydrogen bond is added to the molecule, atop the ring (pointing away from the surface), and sufficient time is given to allow reorganisation to proceed, these regular arrays can be replaced by small clusters, organised in such a way to maximize both π-stacking interactions and hydrogen bonding, demonstrating that the interplay between the various forces present in a molecule are important in determining the final structure.

The studies of alkyl cyano-*p*-biphenyls and cyano-*p*-terphenyls at the air-water interface by Zhang *et al.*[56] offer some interesting insights, even if they were not directly interested in studying π-π stacking interactions. In this work they compare the air-water behavior of the cyano-*p*-terphenyl with a 5-carbon alkyl chain (5CT), wherein the p-isomer means that the cyano, the phenyl rings and the chain are all in a linear arrangement, to a biphenyl version with either a 5 carbon (5CB) or an 8 carbon (8CB) alkyl chain, wherein the longer chain version has an equal molecular length to the terphenyl version, thus compensating for the loss of hydrophobic interaction due to having one less ring. The terphenyl version was shown to have a smaller critical areas compared to the biphenyl versions, indicative of stronger cohesive forces. It was also shown to have a stronger tendency to self-interact when co-spread in a mixture with other non-phenyl surfactants. This stronger cohesion resulted in a more close-packed layer that does not allow for water to penetrate deeply into the monolayer, leaving the hydrophilic group less solvated and making the monolayer behavior more dependent on the π interactions.

1.9. Self-assembled monolayer film on solid support

Self-assembled monolayers (SAMs) are typically prepared by immersing the substrate into a low concentration solution of organic molecules containing a group that will react with the substrate, see Figure 1-5.

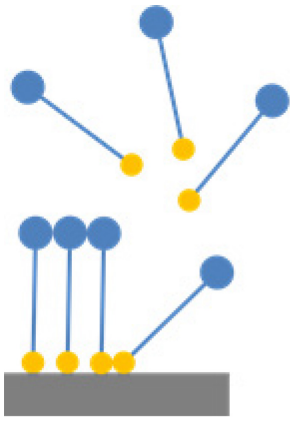

Figure 1-5 Representation of self-assembled monolayer of a molecule possessing a group (yellow circle) that will adhere to the substrate (grey).

One common functional group used to form a strong rapid bond with the substrate is the silane group. It has been shown to bind to a large range of surfaces, from silicon to glass and even metal oxides. However, they are incompatible with water, which causes cross-linking of silane [57], which makes them unsuitable for deposition from the air water interface.

Thus gold-thiol chemistry may be a better candidate[58]; the bond is formed very quickly, requires no special conditions, such as heating or catalysts and is compatible with water. SAM formation involves the immersion of the cleaned gold surface into a dilute solution of thiol in a solvent, typically ethanol[59]. The deposition is a multi-step process[58]; first the surface of the gold becomes covered by molecules in as little as two seconds, at this step the molecules are not fully upright, instead lying flat on the surface, giving a very small thickness when measured. This is followed by an uprighting of the chains as the surface becomes saturated by the thiols, giving thicknesses close to the final maximum thickness. This step is still fairly fast, occurring over the span of a few minutes. Finally the step that take the longest amount of time is the re-organization of the monolayer into its final conformation to maximize the interactions between neighboring chains. This step can take multiple hours. However at the air water interface, the chain will naturally organize in their optimal conformation at the surface of water once spread and before deposition. Therefore, the only relevant step is the gold-thiol bond formation which can happen very quickly and may allow us to "trap" the conformation present at the water without giving it enough time to reorganize.

Different gold surface preparations can result in different surface properties. Gold freshly cleaned using oxidative means is hydrophilic and will therefore have a significant meniscus when in contact with water, this is thought to be due to the formation of a thin oxide layer[60]. But, following oxidative treatment, it is possible to reduce gold back to metallic gold by immersing the gold in ethanol, giving a hydrophobic surface[61], which is also somewhat autophobic with ethanol. Both gold surfaces can chemisorb with thiol and the resultant gold thiol bond is reasonably strong, 40-50 kcal/mol[62], however there is still significant debate on whether or not deposited thiolated molecule can dynamically move on the surface. It has been known for some time that molecules in a low density monolayer can move on the surface, allowing the surface to be fully covered and the chain to become upright. Evidence for displacement on the surface after deposition was provided using an unsymmetrical disulfide (which can also chemisorb on gold and in the process cleaves their S-S bond), where the resulting different chains segregated into different domains[63]. However it is unclear if the molecule can move in fully covered surface[64] of equivalent molecules. Furthermore gold surfaces are considered soft and there is evidence that the underlying gold can move, which can results in movement of the adsorbed layer[65,66], this is due to the weakening of the Au-Au bond once molecules bind to the gold[67]. But these phenomena may only involve displacement of large assembly of molecules (orders of tens of nanometers) in a concerted fashion and thus preserve the molecular organization.

1.10. Functional film formation strategy

Over the years various methods have been proposed for patterning films with some even making it to commercial application for example photolithography. But even the state-of-the-art version of this technique, capable of creating features in the sub 10 nm range[68], still cannot modify the intermolecular distance. Similarly micro contact printing[69] can also be used to create patterns using a stamp to imprint a surface, either by depositing an “ink” or patterning a surface, but the technique is limited by the stamp resolution, which is often itself created using photolithography.

Ultrathin organic sheets can also be formed directly at the air water interface through *in-situ* polymerization of the surfactant. Ponzio *et al.*[70] showed that dopamine dissolved in water will naturally adsorb to the surface. There they can polymerize, into a thin film and be subsequently deposited onto a surface. In this case the film formed was a multilayer, but a similar approach was employed using a

polymer spread directly at the air water interface to obtain monolayer. For example UV light can be used to polymerize an anthracene-based monomer into a 2D polymer following spreading at the air water interface[71].

A related technique that uses polymerization to prepare functional materials with specific binding sites is molecular imprinting[72] (see Figure 1-6). Analytes of interest are brought in contact with a ligand with which it can bind; those ligands are also either attached to monomers or are themselves monomers which can polymerize. Once proper contact is achieved between the analytes and ligands the monomers are polymerized (silica can also be used[73]) and the analytes are washed out. Ideally, the polymer will retain pores which have the correct size for the analyte but also have ligands in the correct position and orientation to maximize interactions with the analyte. This strategy works for a wide range of targets from larger cells, to proteins and smaller molecules and ions. There are several examples in which phenols are used in molecular imprinting, generally as the target analyte[74,75] but also as the ligand[76]. While this technique can be used to control the molecular distance for specific target recognition, it suffers from needing the ligand to polymerize with sufficient porosity for analytes to be able to diffuse in and out.

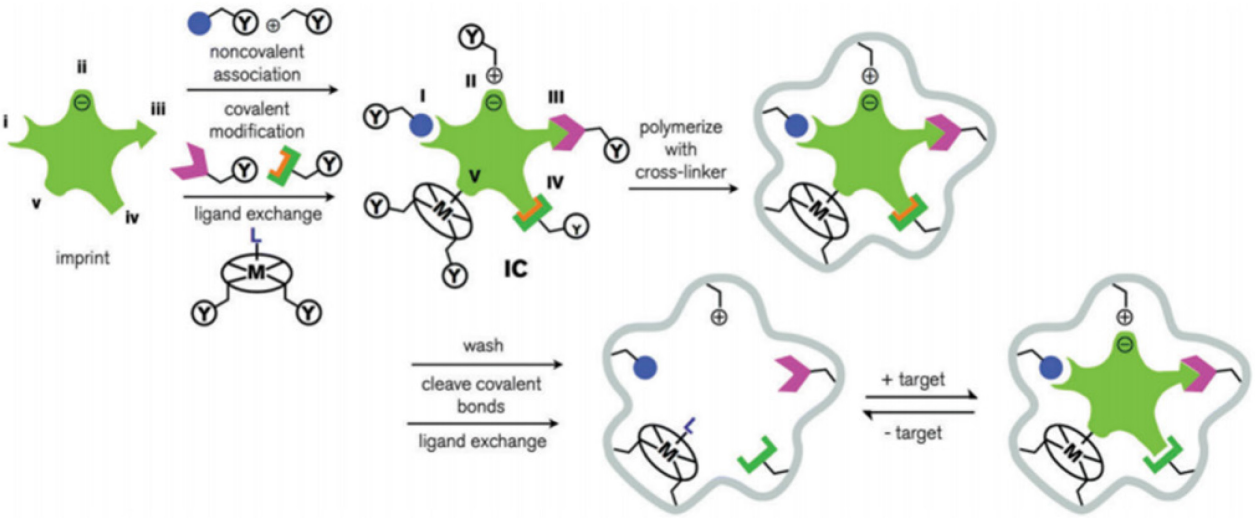

Figure 1-6 Schematic representation of molecular imprinting formation[71]

In this work we seek to combine the concept of molecular imprinting with film pre-organization at the air water interface by introducing the analyte in the subphase before spreading of the film at the air water interface. If these analytes bind with the phenolic surfactants they should force the phenols to be in the

optimal orientation and organization for maximal binding. If this organization can be preserved after transfer, it should be uniquely suited for the analyte of interest.

1.11. Monolayer modification

Monolayers can also be modified pre or post deposition trough various strategies. They can be directly modified and patterned using beams, either ions[77] or X-ray[78], which can modify the chemical make up of the adsorbed molecule or even desorb them to expose the bare substrate, which can be further treated. These techniques are however time consuming and have low output. Other strategies exist to directly modify the surface of the deposited film using chemical means and a wide range of chemical reactions have been reported for films both deposited on gold and silicon, using molecules terminated with chemically reactive groups such as bromine or amides[79]. These modifications not only allow for customization of the terminal group of a monolayer but they can also be used to attach some larger macromolecules like proteins[80]. Using this technique some limited control over the spacing can be obtained by depositing mixed monolayers. Molecules that do not posses the group to be chemically modified can be used as spacers, to force the target molecules away from each other. This however requires immersing the substrate in a solution containing both types of molecule, spacer and target, in the right amount so that both deposit in the required proportion. It also requires that both spacer and target molecules to freely intermix in the monolayer rather than segregate into domains, which is not always possible[81] without additional steps. A similar technique is to instead deposit molecules with terminal groups that can subsequently be cleaved off[82], allowing a new functional group to be exposed and potentially obtaining an organisation that would not be attainable by directly depositing the molecule sporting the final terminal group.

A film can also integrate non-surfactant species if those have a strong affinity for the film. This can be useful when the species are not stable in the spreading solvent, for example proteins that can denature. Medina-Plaza *et al.*[83] integrated enzymes into a film after spreading by injecting them in the subphase and letting them absorb into the film. The film was subsequently deposited onto glass plate, although only physisorbed rather than chemisorbed, and the film was used to discriminate different species of grape by cyclic voltammetry. The electron mediator was included in the spreading film allowing the reaction to proceed.

Monolayers can also be used to create pattern through deposition. Tang *et al.*[84] showed that by transferring films made from mixtures of methyl terminated and disulfide terminated surfactants they could create striped patterns with control over the distance between the stripes. They transferred those stripes onto silicon wafers and further exposed the film to gold vapor, which subsequently reacted with the exposed disulfide group to form a metallic film which conserved the striped pattern.

1.12. Air-water depositions

There are a few reports in the literature of depositing chemisorbed films from the air-water interface using surfactants. Some work used the hydrophilic headgroup as the chemical linker to be chemisorbed onto the surface. For example Gyepi-Garbrah *et al.*[85] used long chain thiols to form films at the air water interface before deposition onto gold. They tested the electrical properties of the film and compared it to film deposited in traditional SAM technique, where the thiol is adsorbed from solution. They found that the films behaved similarly but that the air water deposited film was more organized. Slowinski *et al.*[86] showed that it was possible to transfer surfactants possessing a hydrophilic headgroup distinct from the chemisorbing group, namely a hydroxyl headgroup with a ω-thiol functional group. Using a long, C22 carbon chain, they were able to obtain a monolayer in which the chains stand upright with the thiol oriented towards the air. They showed that they could obtain coating similar to that obtained with a SAM, but in only a few minutes compared to hours.

The monolayer at the air-water interface could also be formed from a mixture of both thiolated and non-thiolated surfactants. Only the thiolated surfactants would chemisorb to the gold such that the non-thiolated surfactant could subsequently be removed by washing[87]. In this work, the two surfactants selected phase separated. As a result, the space left after removal of the non-thiolated surfactant were backfilled with other surfactants to generate a patterned surface. Kageyama *et al.*[88] used mixed monolayers comprising surfactant with and without an ω-terminal silane for chemisorption onto silicon wafers. The monolayer was spread onto water, compressed to the desired organization before being deposited onto the solid substrate. The substrate was then sonicated in solvent, allowing for the removal of the physisorbed surfactant. The exposed, bare surface could then be filled with a surfactant comprising a different functionality. In this case, the surfactants did not mix and removal generated relatively large empty surface areas. In principle, the same approach can be applied to monolayers comprising fully

miscible surfactants, wherein the backfilling could be used to induce full chain extension and exposure of a terminal functional group.

An alternate approach for using mixed thiolated and non-thiolated surfactants involved using the thiol containing surfactant as an anchoring group while the non-thiolated surfactant bears the exposed functional group[89], with non-covalent interactions holding the film together. While this allows some flexibility, it requires the thiol surfactant and the functional surfactant to be miscible in a monolayer. Moreover, the film created may be less robust since only some of the surfactants are chemisorbed.

None of the work surveyed showed much attempt to control the resulting monolayer created via modification of the deposition conditions, nor are there comparisons between similar surfactants that form different phases at the air-water interface.

1.13. Research goals and thesis organization

The goal of this research was to control the intermolecular distances of phenol surfactants via compression in Langmuir monolayers at the air-water interface and to subsequently deposit such films onto solid substrates as functional coatings. This was done in three steps. First, the behavior of phenolic surfactants at the air water interface will be characterised and the extent to which this organization can be modified using pressure and subphase pH was to be studied (Chapter 3). Second, the impact of adding an ω-thiol at the end of the alkyl chain of the phenolic surfactant on the air water interface behavior was to be investigated as well as the impact on deposition (Chapter 4). Finally, to demonstrate its potential for detection applications, the interaction of the phenolic film with representative poly-proline peptides and metal ions was to be studied (Chapter 5). Note that the theoretical background for all experimental techniques employed in the characterization of such films is presented in Chapter 2, prior to the manuscript chapters.

Chapter 2. Theoretical background for experimental methods

2.1. Langmuir monolayers

A Langmuir monolayer is a one molecular thick film made of a single layer of molecules at the air-water interface, these are generally made of surfactants. Surface-active agents[90], more commonly referred to as surfactants, are compounds that reduce the surface tension of water by accumulating preferentially at the air-water interface. In this thesis, traditional amphiphilic surfactants possessing both a hydrophilic headgroup and a hydrophobic tail (long alkyl chain) are studied (see Figure 2-1 for the schematic representation that will be used throughout the thesis). In addition, a special class of surfactants called bola surfactants will be discussed, which possess two headgroups attached at each extremity of the alkyl chain. True Langmuir monolayers are insoluble in the subphase, however, in some cases a small amount may dissolve in the subphase, and the experiment conditions may cause this dissolution to become important. The reverse effect, where dissolved surfactants accumulate at the air-water interface, is called Gibbs monolayer[91] and will not be covered in this thesis.

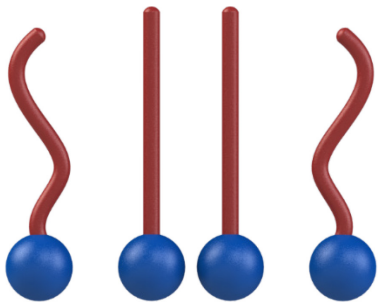

Figure 2-1 Representation of surfactant, with the headgroup in blue and tail in red.

2.2. Langmuir-Blodgett film balance

Monolayers are generally formed and studied using a Langmuir-Blodgett film balance (often referred simply as a Langmuir trough). This technique can also be used in combination with many of the techniques that will be explained later in this chapter. The basic form has changed relatively little since first proposed by Irving Langmuir in 1917[92]. In its simplest form, it consists of a trough, preferably made of Teflon, filled with water. Surfactants are deposited on this water surface, called spreading, by dissolving them in a liquid that possesses two attributes: a propensity to spread at the surface of water[93],

as opposed to forming a drop (lenses), and the ability to quickly evaporate without dissolving in the water, leaving the surfactant on the surface. For all experiments carried out for this thesis the spreading solvent used was HPLC grade chloroform.

One or two movable barriers can be added to the trough, these are used for lateral compression of the film, by reducing the available area that surfactant can occupy and a sensor is used to monitor the change in surface tension. When spread at the surface of water, the surfactant will disperse across the surface and the area available will dictate the phase that the monolayer will adopt, this, in turn, will reduce the surface tension of water. Bare water has a surface tension of 72.8 mN/m at room temperature[94] (sometime express in dyne/cm, which are equivalent to mN/m), and the surface pressure is defined as follows:

$$\pi = \gamma_0 - \gamma$$

where π is the surface pressure and γ_0 denote the surface tension of pure water and γ is the surface tension in the presence of a film. The surface pressure sensor is therefore a balance that measures the amount of force exerted by the water surface on a Wilhelmy plate, for the experiments carried out in this thesis a rectangular piece of filter paper is used. When surfactants are spread at the surface in sufficient quantity they will reduce the surface tension of water, by covering the water, which reduces its ability to interact with the Wilhelmy plate. This in turn reduces the force exerted on the plate and can be measured as a reduction in force measured by the surface pressure sensor, see Figure 2-2 for full representation of the Langmuir-Blodgett trough balance.

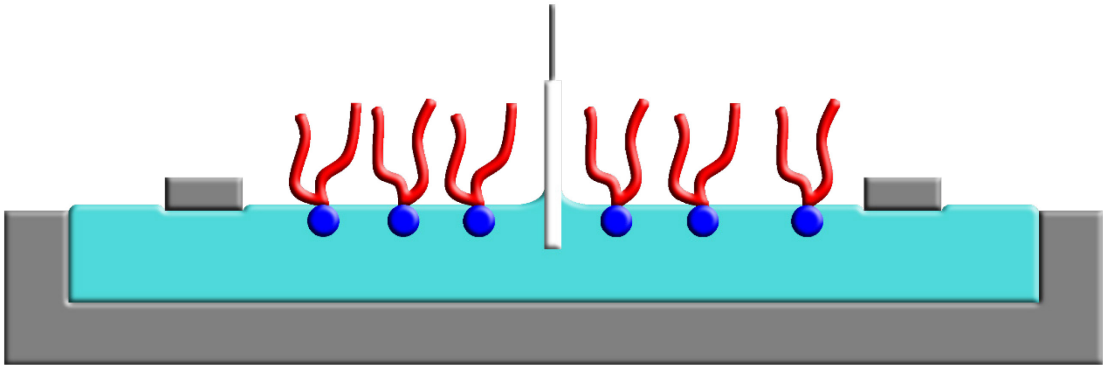

Figure 2-2 Langmuir-Blodgett trough balance, with representation of surfactants.

2.3. Surface pressure molecular area isotherms

The Langmuir film balance is often used to measure the surface pressure-molecular area isotherm[95], see figure 2-3 for schematic. At the surface of water, the monolayer can be considered as a pseudo 2-dimensional system, and the phase adopted by the monolayer can be compared to the phases found for the bulk, 3-dimensional material. When the available surface area is very large the surfactant may adopt a phase reminiscent of gas phase, called the gaseous phase, where every surfactant is lying flat (horizontally) on the surface and the surfactants are sufficiently distant from each other so as to not be required to interact. The barriers may be used to reduce the available area, this is measured as molecular area, defined as the surface area of the trough enclosed by the barriers divided by the number of surfactant molecules, with units of $Å^2$/molecules. Reducing the molecular area available, compressing the monolayer, will cause phase transitions to occur by forcing the surfactant in close proximity. The molecular area where the surface pressure begins to increase is called the critical area and corresponds to the formation of a coherent film covering the surface. This film can adopt a different phases, depending on the chemical structure. In many cases, the phase that is initially formed is the liquid expanded (LE) phase, analogous to a liquid phase for bulk material. In this phase, the chains interact but have a high degree of conformational freedom due to the relatively large molecular areas. As they are compressed, the chain begin to extend into the z-direction, i.e. out of plane. With sufficient reduction in surface area, a first-order phase transition can take place, which in the isotherm is represented by a plateau in the surface pressure. In this region there is co-existence of two phases, namely the LE and a condensed phase. At the

end of the plateau, the film if fully converted into the condensed phase, analogous to the transition to a 3-dimensional solid phase. In these condensed phases, the surfactants are in a liquid crystalline state, with a defined arrangement in a repeating organization. A rich polymorphism of different phases can be formed which are defined by differences molecular tilt directions, chain orientational and translational order[96]. Although discussion of all of these phases is outside of the scope required here, it is important to note the distinction between tilted and untilted phases, which depends on whether or not the tail tilt compared to the normal of the subphase, even though not every system will change its tilt due to compression. One of the aspect that may cause the tilting of the tail of a surfactant is the relative size of the headgroup versus tail cross-sectional areas. If an headgroup area is larger than the cross sectional area of the tail, then the tails of neighboring surfactants will not be able to interact with each other when fully upright, through Van der Waal interactions, as such they will naturally tilt to maximize those interactions. Eventually, the film cannot be compressed further and remain as a monolayer leading to collapse, which is the point where the system cannot keep acting as a pseudo 2-dimensional system. This can manifest itself as the formation of multilayer, aggregate at the surface or the dissolution of the surfactant into the subphase.

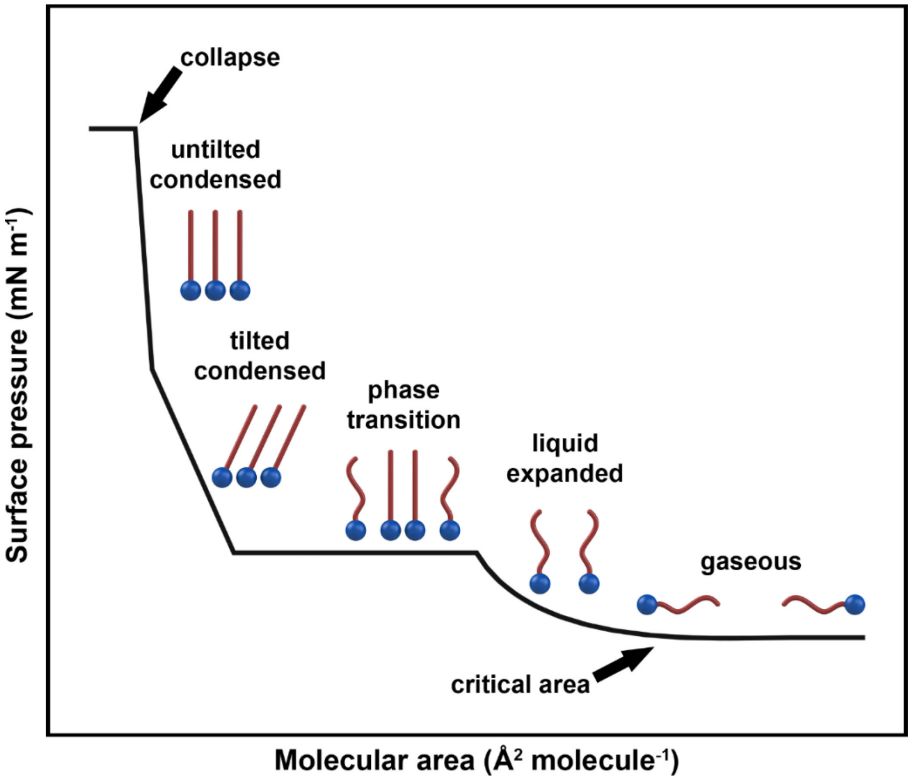

Figure 2-3 Schematic representation of a surface pressure-molecular area isotherm with the associated phases that can be formed.

The isotherm shown in Figure 2-3 is highly idealized. Not all monolayer isotherms will exhibit every phase, for example, a surfactant spread on a large area may have sufficiently strong interactions with itself that it will favor being in a condensed phase even at high molecular areas. Similarly, a system may collapse before reaching a condensed phase, e.g. a chain comprising one or more units of unsaturation can prevent condensation at room temperature. Furthermore, as the films is undergoing a dynamic compression, it is not always at equilibrium. In the case of rigid or viscous films, this may cause local differences in organization and compression state, e.g. the surface pressure will be higher next to the barriers. Local collapse may occur even while the surface pressure continues to increase (generally manifesting itself as a decrease in the slope while the surface pressure is still rising). In some cases, it is possible to mitigate these problems by slowing down the rate of compression. Finally, once spread at the surface of the water the surfactant will not necessarily initially adopt their most stable conformation. In general, the time required for evaporation of the chloroform is usually sufficient for equilibrium to be reached while others require a longer equilibration period. However long equilibrations times and

extremely slow compression rates, on the scaled of hours, generate additional problems: the water will slowly evaporate which alters the surface tension measurement, and atmospheric carbon dioxide will slowly dissolve in the subphase, potentially changing the pH.

2.4. Brewster angle microscopy

Brewster angle microscopy (BAM) is a visualization technique at the air-water interface[97,98], used in conjunction with a Langmuir trough. This is relatively new technique, first proposed in 1991[99]. Previously morphological features at the air-water interface were visualized using fluorescence microscopy, but this requires adding a small amount of fluorescently-labeled surfactant or a fluorescent probe to the monolayer, which could modify its phase behavior. BAM works by exploiting the properties of polarized light[100] and as such requires no probe. The Brewster angle is the angle at which p-polarized is perfectly transmitted through the medium and as such does not produce a reflection. It is dependent on the refractive index of the two media (here air and water) and will therefore vary based on the wavelength used. For the air-water interface at a wavelength of 532 nm (Nd:YAG laser) the Brewster angle is 53.13°[101]. A film spread at the air-water interface will have a different refractive index than the underlying water and therefore will reflect some of the light. As such, a film can be visually distinguish from bare water, even when this film thickness is on a much smaller scale than the wavelength of the light used, see Figure 2-4a. This is however, of limited use in a system that are in either the gaseous or the liquid expanded phase, as these will naturally cover the surface and will give a uniformly bright surface with little information as to the phase and behavior (the related technique of ellipsometry will be discussed below). The main use of this technique is to visualize the morphology of the condensed phase, since condensed phase domains can have distinct shapes[102] and exhibit a strong contrast to the surrounding gaseous or liquid expanded phase[103]. Furthermore, internal anisotropy can be visualized[97]; if a domain comprises of surfactant that tilts in different direction the light will encounter different environment based on whether the tail tilt is parallel or perpendicular to the incoming light beam, this will manifest itself as alternating areas of bright and dark, see Figure 2-4b. The shapes, morphology and internal anisotropy of condensed phase domains have been related to surfactant orientation, organization and intermolecular interactions[102].

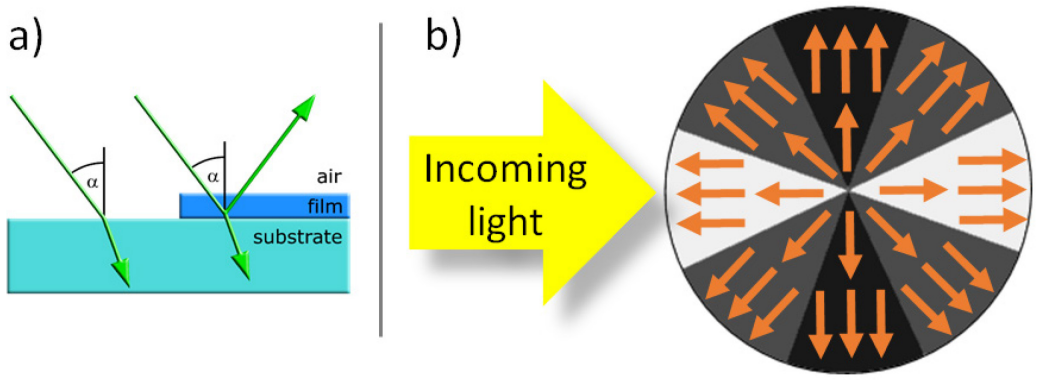

Figure 2-4 a) Representation of the Brewster angle of water when striking a bare water surface and a water surface covered with a monolayer, b) Representation of the impact of anisotropy on the reflected polarized light observed in BAM. Chain tilt direction is represented by the orange arrows. Note that the effect can present itself in many different patterns: the domain may not be circular, the tilt change does not have to originate from the center and the boundary may or may not be sharp. A review of the different internal anisotropies can be found in reference[102].

2.5. Ellipsometry

Ellipsometry, specifically nulling ellipsometry for the experiment carried out in this thesis, is a technique that also use a polarized light[104,105], similar to BAM. When light reflects from a medium, its polarization will change depending on the optical properties of the medium. If the medium is covered by a thin film, then the optical properties will depend on the physical attributes of the film, including the film thickness. Changes in polarization reflect changes in optical properties and, assuming a uniform film, these can be correlated to changes in thickness. A schematic of the setup employed is given in figure 2-5, light from the laser first goes through a linear polarizer, creating linearly polarized light of known polarization. The light then goes trough a retarder, usually called compensator, this is generally set at 45°, creating circular polarized light. The light then strikes the medium and the reflected light will have a linear polarization. This allows a second polarizer to act as an analyzer, by rotating it such that it is at a 90° to the light polarization, where the light will be fully extinguished. Thus, the difference in polarization due to the medium can be determined. This difference in polarization manifests itself as changes in the polarization angles, Δ and Ψ, where Δ is the phase difference and Ψ is the ratio of the amplitudes.

Extracting information from the changes in Δ and Ψ requires fitting the data to a multi-box model. For a 2-box model representing a film atop a subphase, some assumptions are required. The subphase, whether

solid or liquid, is considered infinite and the thin film is considered homogenous, smooth (roughness below 50 Å[106]) and isotropic. In the case of films at the air-water interface, for which vibrations play a significant role, this is a non-trivial process the data is generally presented as $\delta\Delta$, in other words the changes in change of phase between different measurement (Ψ is assumed to be constant). The two most common reasons for a change in Δ are the increase in film thickness with compression and changes in phase of the film, which may or may not be accompanied a changes in thickness. It is important to note that the beam footprint is of several μm^2, therefore the measurement represents an average of the surface. If the domains are sufficiently small, as in the case of nanodomains and early nucleation aggregates, it may not be possible to select a region of interest which corresponds solely to one phase and the measurements therefore represent the weighted average for the phases in the field of view. The ellipsometer employed here is an imaging ellipsometer which enables the user to view the film real-time and select the region of interest.

Measurements are also made at the air-solid interface. In this case, the data are fit with a 3-layer model, namely gold-film-air. The film is considered to be uniform with a constant refractive index throughout the vertical z-axis direction. While this is not quite accurate due to the differences in the headgroup and alkyl chain regions, these differences are considered negligible for most Langmuir films[58]. For an accurate measurement of the thickness, both the refractive index, n, and the extinction coefficient, k, of the substrate must be known. In the case of gold, the substrate used in this thesis, those values are extremely sensitive to the nature of the gold substrate (thickness, grain size and crystallinity[107]) and thus have to be determined for each individual substrate before sample deposition, which is also done using nulling ellipsometry.

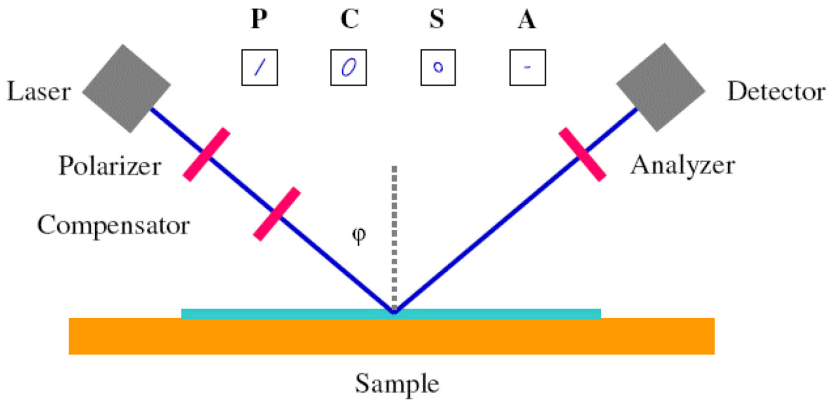

Figure 2-5 Ellipsometer component used at the air solid interface, note that the setup is also shared with BAM.

2.6. Atomic force microscopy

Atomic force microscopy (AFM) is an imaging technique that can obtain topological information about a sample deposited on a solid support. The measurements in this thesis were carried out in tapping mode, using a very fine tip vibrating above the surface. Because of the forces exerted on the tip by the surface, such as van der Waals or dipole interactions, the amplitude of the tip oscillation will change. A feedback loop is used such that the tip to surface distance is varied using a piezoelectric actuator, such that the amplitude is kept constant. In this way, the surface topology is scanned and at the same time, information about the nature of the surface is obtained from the phase change of the oscillation. AFM however does not measure the true height of the film or features (in reference to the bare substrate), it only measure the difference between features seen at the surface; in most cases the bare substrate is not exposed. Furthermore the roughness of the background will have very significant effects on the topography measurement of thin films, especially when the roughness is of the order of magnitude or larger than the film thickness. For this reason, whenever possible mica is used as a substrate, since it is atomically flat with roughness value of 0.054 nm over 1 μm^2 [108]. For comparison the roughness of the gold substrates used in this work is on the order of 0.8 nm over 1 μm^2. Measurement of some features can be tip limited, for example if the tip radius is larger than the width of a hole or crevice, the true depth may be underestimated.

2.7. Langmuir deposition methods

Films spread at the air water interface can be transferred onto a solid support using a mechanical arm to push or pull the substrate trough the monolayer at the air water interface. Herein films are deposited using the Langmuir-Blodgett (LB) geometry[109], where the solid substrate is perpendicular to the surface of water, see Figure 2-6, in contrast to Langmuir-Schaefer depositions which are made in a parallel orientation. The depositions are carried out at constant surface pressure, where the barrier continuously compresses the film while material is being removed from the interface. The barrier compression speed and the transfer speed, vertical movement of the substrate, are important parameter to control, generally those are set as low as possible to avoid modifying the morphology of the film to avoid transfer artifacts. To ascertain the quality of the deposition the transfer ratio is measured, which is the ratio of the surface area of the film removed during the transfer over the surface area of the substrate, a ratio between 0.8 and 1.2 is considered to indicate a good transfer.

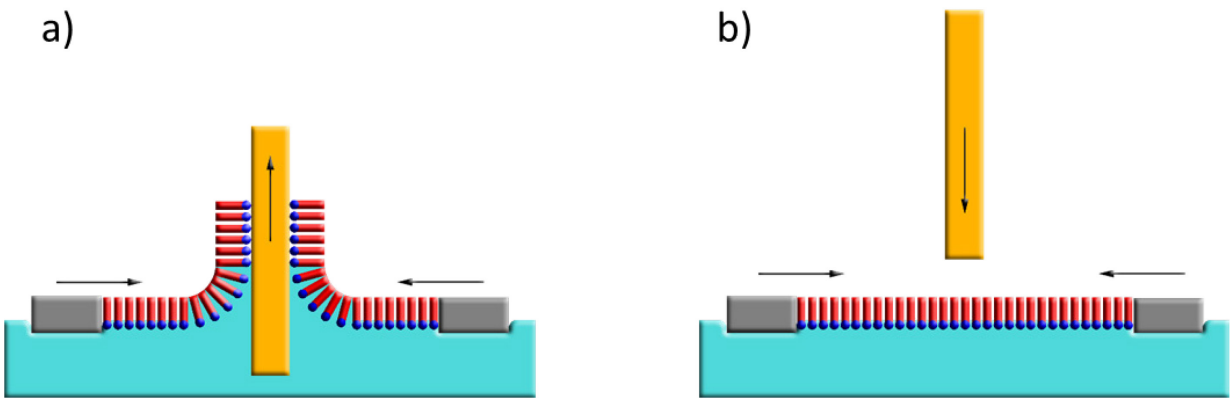

Figure 2-6 Langmuir-Blodgett transfer onto a solid support, a) upstroke, b) downstroke.

2.8. Grazing incidence X-ray diffraction

Grazing incidence X-ray diffraction (GIXD) is a crystallographic technique carried out at the air-water interface using short wavelength X-ray from a synchrotron source ($\lambda \approx 1$ Å)[110,111]. When X-rays strike the surface of water below the critical angle (around 0.13°) total external reflection will occur. This

also creates an evanescent wave, a wave whose intensity decrease exponentially with depth, at the surface of the water, which makes it surface specific. If an ordered, liquid crystalline film is present at the surface of water, the constructive interference of diffracted X-rays will generate a diffraction pattern according to Bragg's Law. Condensed monolayers at the surface of the water comprise many small domains, in effect micro crystals, this is therefore a powder-averaged X-ray diffraction, one that is limited to a 2D plane. This create a few differences compared to single crystal crystallography; it is not possible to distinguish between the Q_x and Q_y components of the scattering vector, thus the in-plane Q_{xy} component is obtained. GIXD also does not produce Bragg points but rather Bragg rods, which extend into the Q_z direction, perpendicular to the plane, see Figure 2-7a for schematic representation of a contour plot of the raw data obtained. Furthermore, the crystalline domains are fairly small and as such only the strong first order peaks are generally observed. As the monolayer forms a 2-dimensional powder crystal, analysis of the data provides information on the relative the positions of the surfactant (usually the chains) rather than the exact location of atoms. The surfactant chains can be approximated as cylinders pointing upward or tilting. The packing is hexagonal or distorted hexagonal, in a top down view see Figure 2-7b, with the chains untilted or tilting toward either nearest neighbor (NN), next nearest neighbor (NNN) or an intermediate direction. Because of the (distorted) hexagonal arrangement, every surfactant is surrounded by six other surfactants, giving rise to six potential reflections. However some of the reflections are partially or completely obstructed by the water at the bottom of the trough. This limits the detector to only seeing all reflections when those are all in plane (Q_z=0) at which point only half a peak is seen, see Figure 2-7a "untilted" for an example with two in-plane half peaks, the other half of the peak(s) being below the surface. Peaks can also be out-of-plane, Q_z above 0. This gives three possible scenarios. In the first, a single peak is detected at Q_z=0, representing a combination of all six degenerate reflections which occurs when the surfactants in the monolayer are untilted and all sides of the hexagonal are equal, figure 2-7b where a=b=c and γ=120. In the second, two peaks are observed (either both at Qz=0, one at Qz=0 and one at Q_Z>0 or both at Qz>0, see Figure 2-7a first three cases) wherein one peak is degenerate and the other is non-degenerate, represented in figure 2-7a by more contour lines (stronger intensity). This scenario occurs when one of the axes of the hexagon is unequal to the other one, a≠b=c leading to a centred rectangular unit cell. This can occur without tilting of the tail (7a "untilted") but is most often associated with tail tilting towards either NN or NNN. The third possible scenario yields three peaks, in

which case a≠b≠c, this indicates that the tail is tilted in an intermediate direction, i.e. in between an NN and NNN tilt.

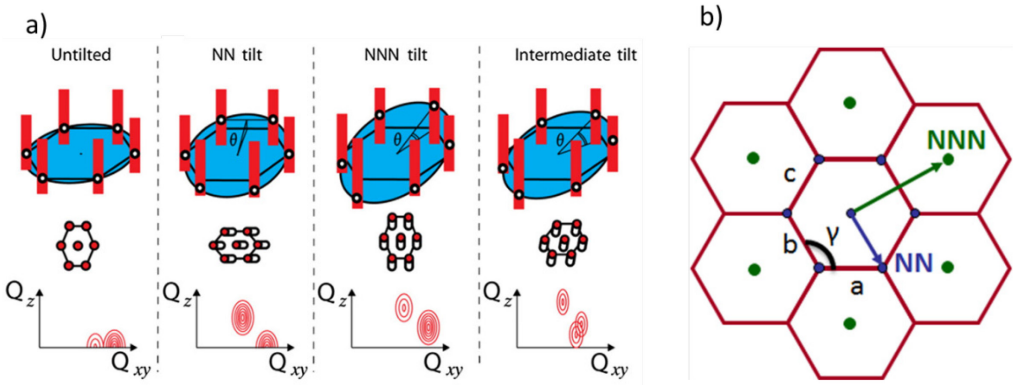

Figure 2-7 a) Potential diffraction pattern depending on the chain tilt with a side view along with the reciprocal disc (top) a top down view of the packed chains (middle) and the resulting diffraction pattern (bottom)[112], b) top down view of a representative monolayer in hexagonal pattern, blue and green circle represent chain location, with the arrow potential tilt direction.

These schematic shows well-separated peaks and properly identifying the location of peaks or even the number of peaks is often non-trivial. The fitting is guided by the following selection rules. The location in Q_z of the peaks must follow $Q_z1+Q_z2=Q_z3$, in other word; the location of the highest peak in Q_z must be equal to the sum of the location of two lower peaks [113]. Furthermore information can be obtained from the full width at half maximum (FWHM), or coherence length, of the peaks, in both Q_{xy} and Q_z, using an equation derived from the Scherrer formula[110,111]:

$$L \approx 0.9 \left[\frac{2\pi}{FWHM}\right]$$

which when used with the FWHM in Q_{xy}, this gives the coherent length of the domains, the average length of the crystallites. Note that different peaks can give different coherent lengths, which will indicate that the the crystallinity in different crystallographic planes differs. When used with FWHM in Q_z the information obtained is the length of the scattering rod which correlates to the thickness of the crystalline phase. It therefore follows that all peaks must have the same FWHM in Q_z, if they all originate from the same crystalline structure, since a crystalline monolayer would have uniform thickness. If some peaks

have different FWHM in Q_z it is indicative that they must either be combination of multiple peaks at different Q_z but same Q_{xy} or be from different crystalline phases. Furthermore, because the thickness is limited by the length of the alkyl chains, a value of L_z that is too long or short compared to the maximum length of the chains indicate that the fit obtained must be from multiple overlapping peaks. In most cases only the alkyl chains needs to be considered, headgroups are generally not crystalline since they are surrounded by water and can easily rotate, preventing them from organising in a repeating unit, although examples of large headgroup (larger than the alkyl chain(s)) being crystalline in a different organisation than the tail region can be found in the literature[114,115]. Diffraction peaks from molecular lattices that include larger assemblies and multiple headgroups can also arise producing far more complex patterns. It should be noted, although not applicable to this thesis, when surfactant or lipid possesses multiple tails, such as naturally occurring phospholipids, the diffraction pattern obtained represents the lattice for the alkyl chains and not the whole lipid.

To convert from diffraction pattern into real space coordination the following formula can be used[110]:

$$d = \frac{2\pi}{Q_{xy}} = \left[\frac{h^2}{a^2} + \frac{k^2}{b^2} - 2\left(\frac{hk}{ab}\cos\gamma\right)\right]^{-\frac{1}{2}} \sin\gamma$$

where d is the d-spacing, Q_{xy} is the location of the peak in Q_{xy}, h and k are miller indices of the peaks, these will have integer value between 0 and 2 since only the first order peak are seen (more on miller indices later), a and b are the distance between the surfactant (refer to 7b) and γ is the angle between a and b. While the miller indices are not known, because they are restricted to integers, it is possible to determine the value a, b and γ using only three peaks (fewer if there are degenerate peaks) despite there being five unknowns (a, b, γ, h, k). Note that those values are dependent on the unit cell chosen to do the calculation, in this thesis both the hexagonal and the centered rectangular unit cells are used, see figure 2-8 for comparison of the two. Note that the reflections are due to the Bragg plane rather than points, which do not always coincide.

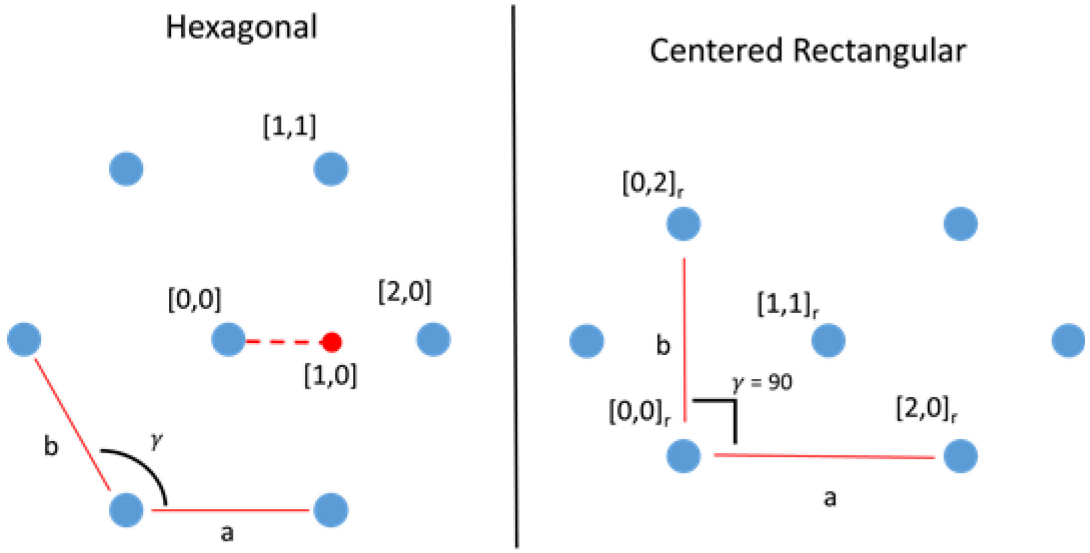

Figure 2-8 Comparison of hexagonal and centered rectangular unit cell, representation of the tail organisation in top down view, along with the miller index, the blue circle denote the location of a surfactant tail, note that the red circle is provided as a reference point and does not indicate the location of a surfactant

In the case of a NN tilt, the tilt angle of the surfactant can be obtained using the following formula[111]:

$$Tan\ \theta = \frac{Q_{zd}}{\left[Q_{xyd}^2 - (\frac{Q_{xyn}}{2})^2\right]^{\frac{1}{2}}}$$

where θ is the tilt angle relative to the normal of the surface, Q_{zd} is the location in Q_z of the degenerate peak, Q_{xyd} is the location in Q_{xy} of the degenerate peak and Q_{xyn} is the location in Q_{xy} of the non-degenerate peak.

For the case where the tilt is in the NNN direction, the following formula is used:

$$Tan\ \theta = \frac{Q_{zn}}{Q_{xyn}}$$

Until now, only cases where every surfactant is equivalent were considered, but a special case need to be introduced for this thesis, namely the herringbone packing, where the tails are related to each

other by glide symmetry, see figure 2-9. Tails are typically considered as rods because in the rotator[116,117] phase, they are able to rotate freely around there long axis. This is not the case in a herringbone phase[118], where the tails are locked into place by the steric interaction of the hydrogens. This causes non-equivalency between the tails, and give rise to an additional diffraction peaks, seen at slightly higher Q_{xy} values.

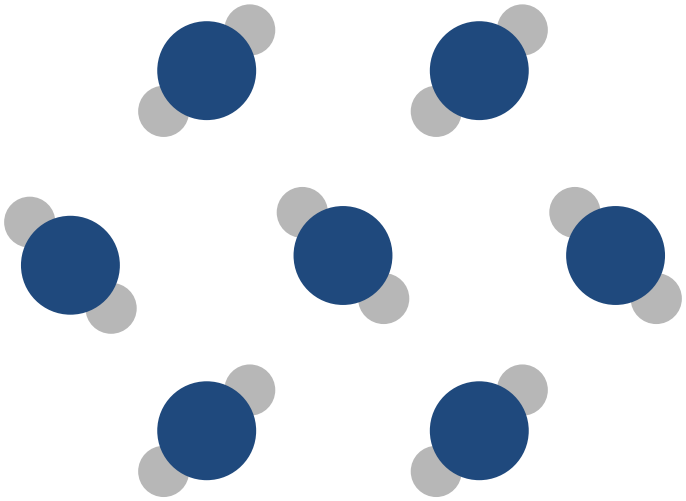

Figure 2-9 Cross sectional area of surfactant tails in a herringbone arrangement.

2.9. Total reflection X-ray fluorescence

Total reflection X-ray fluorescence (TRXF) is another synchrotron based X-ray technique. X-rays are capable of ejecting core electron from atoms. These electrons leave behind holes in the orbital which can subsequently be filled by higher orbital electrons falling down in energy, emitting a photon as fluorescence. The energy of the emitted photon will depend on the energy difference between the orbitals involved, which is element specific. This enables identification of elements from their characteristic fluorescence emission lines. Furthermore, the intensity of the emission is proportional to the quantity of the element present, assuming the concentration is low enough for self-absorption effects to be ignored, allowing for quantification.

When X-ray are reflected off the surface of water, the depth of penetration in the water is dependent on the angle at which the light hit the interface, particularly around the critical angle[119–122]. Below the critical angle the depth penetration is on the order of a few nm, above it is on the order of µm (see figure 2-10).

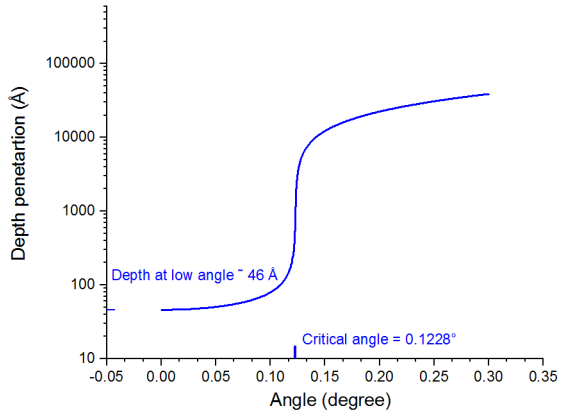

Figure 2-10 Depth penetration of X-ray at the air-water interface as a function of the incident angle for pure water, X-ray at 10 keV, y-scale is logarithmic

Therefore by taking measurements above the critical angle, information about the bulk concentration and identity of elements (in this case solvated counter ions) is obtained. Below the critical angle, only the counterions located in the vicinity of the interface are detected. Normally, the quantity of

ions at the interface is too low to be detected, but if the ions are attracted to a spread monolayer at the air-water interface, it is possible to get a drastic enrichment in ion concentration near the interface.

The experiment in this thesis were carried out using a beam of 10 keV (wavelength of 1.24 Å). For both elements used, copper and zinc, the $K\alpha_1$ line and $K\alpha_2$ ($K\text{-}L_3$ and $K\text{-}L_2$ in IUPAC notation) were used to quantify the ions. The $K\alpha_1$ line and $K\alpha_2$ are indistinguishably close (Cu $K\alpha_1$= 8 047.78 keV, $K\alpha_2$= 8 027.83 keV, Zn $K\alpha_1$= 8 638.86 keV, $K\alpha_2$= 8 615.78 keV)[123] (Figure 2-11) and so are considered together. The copper $K\beta_1$ ($K\text{-}M_3$, 8 905.29 keV) was also detectable but was not used for analysis.

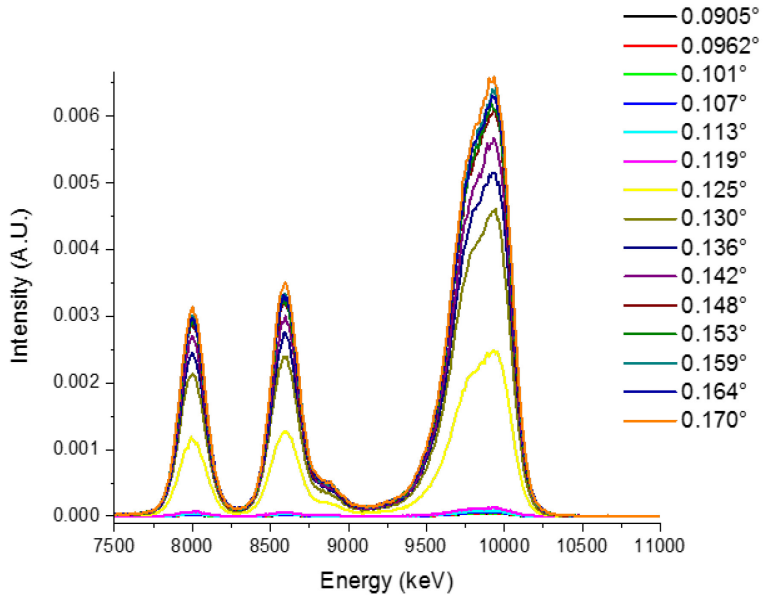

Figure 2-11 X-ray spectra for calibration over a solution of Cu and Zn (20 mmol/L), multiple spectra are overlaid together, each taken at a different incident angle.

Multiple measurements were taken at different angles ranging from 0.0904° to 0.1695°. By scanning both the bulk and the interface it is possible to compare the two and knowing the bulk concentration, the surface concentration can be determined through modeling of the system. The surface concentration (in molecule/Å^2) can be compared to the molecular area from the air-water isotherm to obtain a ratio of counterions to surfactant.

2.10. Surface plasmon resonance

Surface plasmon resonance (SPR) is another technique that exploits the phenomena of evanescent waves[124], much like GIXD and X-ray fluorescence. A film is immobilized onto a substrate with a thin outer layer of gold, typically gold. When p-polarized light is directed at the surface at the angle for total internal reflection some of the light energy is transferred to a plasmon field created in the gold. This creates an evanescent wave (Figure. 2-12a)[125], due to the excitation of the electrons in the metal, which penetrate into a solution, typically to a depth of a quarter of the wavelength used[126] (λ=780 nm for the instrument used in this thesis). The energy transferred results in a decrease in intensity of the reflected light. The angle necessary to obtain this resonance effect is dependent on the optical properties of the medium interacting with the evanescence wave, this in turn is dependent on the mass present at the surface. Therefore, if analytes bind to the surface, displacing water in the process and changing the mass and nature of the medium, this will cause a change in intensity of the reflected light, since the angle is no longer the optimal angle for creation of the plasmon field. By monitoring the changes in intensity or in angle required to get optimal resonance (the angle at which the reflected light is the weakest) the changes in surface concentration can be monitored. Experiments are carried out with a constant flow of water or buffer (main solution). Samples are injected into a loop, with a valve allowing the main solution to go straight to the chip chamber or to go through the sample loop, pushing the sample into the chip chamber, over the immobilized surface.

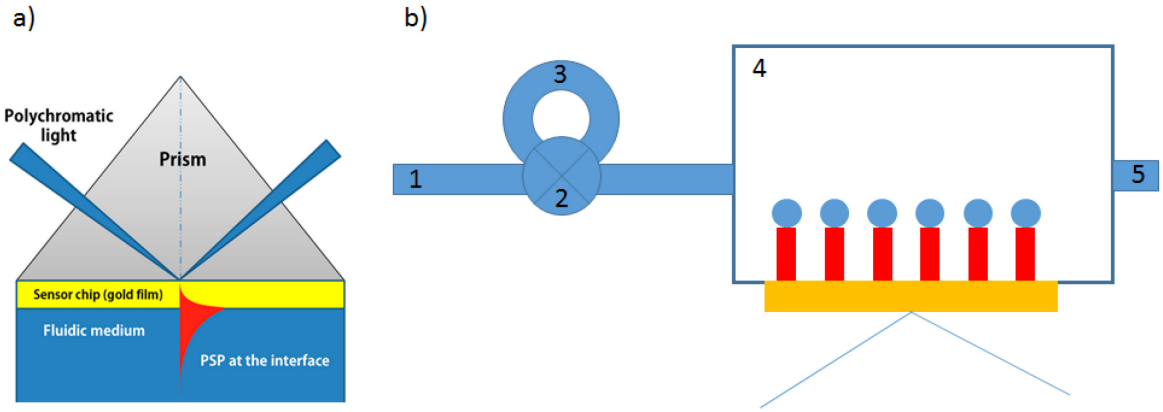

Figure 2-12 a) Representation of SPR evanescence wave effect with intensity represented in red, presented upside-down from the instrument used (solution is at the bottom of the image)[124]. b) SPR instrument configuration, 1) main solution 2) valve, either connecting the main solution directly to chips or through the sample loop 3) Sample loop 4) chamber containing the chips with immobilized thin film 5) waste

Chapter 3. Strong headgroup interactions drive highly directional growth and unusual phase co-existence in self-assembled phenolic films

3.1. Abstract

Self-assembled materials as surface coatings are used to confer functional properties to substrates but such properties are highly dependent on the molecular organization that can be controlled through tailoring the non-covalent interactions. For monomolecular films, it is well-known that strong, dipolar interactions can oppose line tension generating non-circular domain growth. While many surfactant films exhibit liquid crystalline arrangement of the alkyl chains, there are relatively few reports of crystalline headgroups. Here we report the self-assembly of phenolic surfactants where the combination of hydrogen bonding and π-stacking leads to a herringbone arrangement of the headgroups, generating a molecular super-lattice that can be observed using grazing incidence X-ray diffraction; such an arrangement has been previously proposed for related phenolic systems but never experimentally observed. We also investigated using pH to modulate the intermolecular interactions and the response of the system in terms of molecular organization. The first hydroxyl deprotonation of octadecyl gallate does not appear to impact the structure but has significant impact on the domain size and morphology. Higher pH generates both strong directional domain growth and a loss of the molecular lattice structure, attributed to a second deprotonation. In contrast, a shorter chain surfactant, lauryl gallate, forms a liquid expanded phase that can contract upon deprotonation. In the condensed phase, the deprotonation kinetics are unusually slow, taking close to an hour, for which an internal charge re-organization is proposed. The slow kinetics leads to the co-existence of three distinct phases for a single component system over relatively long timescales and provides evidence of a liquid-mediated polymorphic transformation process in two-dimensional, soft-matter films. This work has implications for understanding the long-range ordering in aromatic self-assembled structures and the mechanisms underlying Langmuir monolayer polymorphism.

3.2. Introduction

Polyphenols such as tannins exhibit antioxidant, protein binding and metal chelating properties[127]. The latter is dependent on the orientation and proximity of multiple phenol moieties[128]. Phenolic surface coatings may confer such properties to a substrate and it may be possible to tune the reactivity and specificity by modifying the distance between phenols. While it is possible to control the distance by synthesizing polyphenols with specific arrangements, an alternative method would be to control the intermolecular distance in self-assembled films using phenolic-derived building blocks. For example, long-chain phenolic surfactants and lipids have been shown to self-assemble at liquid[129] and solid surfaces[130]. In this work we seek to control the domain morphology and intermolecular distances in Langmuir monolayers at the air-water interface; such films could subsequently be deposited onto solid substrates as coatings to harness the phenol properties.

The organization of surfactants at the air-water interface is determined by non-covalent interactions. The interplay of hydrogen bonding, ion-dipole and/or dipole-dipole[50,131] interactions and π-stacking[132] are shown to modify the structure and morphology of surfactant films. Phenol headgroups afford the opportunity to modify each of these which in turn can be used to tune the inter-phenolic distance. With more than one hydroxyl on the headgroup, the charge can be varied systematically, inducing either attractive or repulsive interactions. Additionally, the hydrophobic tail can be modified by changing the length and the number of branches while the headgroup interactions can be altered by changing the subphase composition. For example, the addition of ions to the subphase, either as part of the effort to modify the pH of the subphase or by deliberately adding salt, non interacting ions, can also modify the interaction with ions influencing the monolayers behavior[133], like morphology or critical area.

Our group previously reported the monolayer properties of a phenol lipid, dipalmitoylgalloylglycerol, and found evidence of a highly cohesive and rigid film attributed to an extensive hydrogen bond network between the phenol headgroups which comprise multiple hydroxyl groups[37]. Peikert *et al.*[134] studied phenolic surfactant films with variation in hydroxyl position. Using grazing incidence x-ray diffraction (GIXD) and computational methods, they determined possible arrangements of the headgroups where the aromatic ring can interact with 4 adjacent rings, maximizing the π-stacking interactions, hinting that despite the weakness of the π-stacking relative to hydrogen

bonding, this can still significantly influence the organization of the monolayer. Studies of phenol-terminated self-assembled monolayers (SAMs) showed that simply changing the hydroxyl group from the *meta*- to the *para*- position can lower the surface coverage of the deposited SAM by 40% to 60%, attributed to a modification of the organization at the interface[39]. Not only the position of the hydroxyl on the ring, but also the protonation state affects the orientation and exposure of the headgroup and hence the hydrophilicity of the film surface[39]. Azmi *et al.*[40] showed that the relative hydroxyl positions (1,2- or 1,3-) of dihydroxyphenol-terminated SAMs determined the intermolecular hydrogen bonding that impacted the extent of binding of the phenolic SAMs with phosphate. Specifically, the 1,2-diol had significantly higher binding potential to monoprotic phosphate, attributed to the ability of the 1,3-diol to

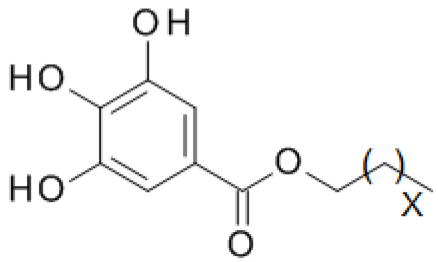

Figure 3-1 Structure of surfactants used, X=10 Lauryl gallate (LDG), X=16 Octadecyl gallate (ODG).

hydrogen bond with multiple neighboring surfactants, reducing the binding potential to the phosphate.

In the present work the self-organization of two phenolic surfactants, lauryl gallate and octadecyl gallate (ODG) (Figure 3-1), which differ only in the length of their chains, are studied as a function of monolayer subphase composition. The difference in chain length enables determination of the impact of suphase pH and ionic strength as a function of the phase of the film (liquid-expanded versus condensed) while maintaining the same headgroup. The two phases afford different routes to controlling the intermolecular spacing that will be required for applications involving protein and metal binding.

The organization of phenol surfaces and interfaces is relevant for understanding systems as diverse as the interaction of aqueous phsophates with phenolic-rich natural-organic matter (humic material)[40] to natural and synthetic cross-linked biopolymer materials including the adhesion of mussels[135] and protein binding [5]. A recent review highlighted the importance of phenolic building blocks for the assembly of functional materials [136]. Amphiphilic phenols provide the opportunity to tailor the self-assembly of

materials via modifications in the arrangement of functional moieties on the headgroup, and electrostatic contributions to hydrogen bonding (H-bonding) affect film organization, properties, and structure.

3.3. Materials and methods

Materials. Lauryl gallate (≥99.0%) was purchased from Sigma-Aldrich and used without further purification. Ocatdecyl gallate (ODG) was synthesized from gallic acid and octadecanol using para-toluene sulphonic acid[137] under reflux conditions and recrystallized from chloroform and hexane. Ultrapure water (resistivity of 18.2 MΩ/cm) was obtained from an EasyPure II LF system (Barnstead, Dubuque IA). The spreading solutions were prepared using chloroform (HPLC grade, trace of ethanol as preservative) from Fisher Scientific Company. Mica (grade V1) used in the AFM deposition was purchased from Ted Pella Inc. and freshly cleaved before each measurement.

Isotherm measurements. Monolayers were spread from a chloroform spreading solution (1 to 1.5 mM) on three different types subphases: i) ultrapure water (pH = 5.5 at 25 °C), ii) ultrapure water that was adjusted to higher pH using NaOH, iii) ultrapure water that was ionic strength adjusted using NaCl. Surface pressure-area isotherms were obtained on Langmuir film balances (Nima Technology Ltd., Coventry, U.K.) at room temperature with a compression speed of 5 cm^2/min (equivalent to between 3 to 7 $Å^2$/(molecule • min) depending on spreading solution concentration). Two different Langmuir film balances were used, one with dimension of 5 cm by 35 cm was used for lauryl gallate isotherms and Brewster Angle Microscopy and the other had dimensions of 7 by 15 cm and was used for octadecyl gallate isotherms. Surface pressure measurements were made using a filter paper Wilhelmy plate (Whatman No. 1 paper). Monolayers were given 10 minutes for film relaxation unless stated otherwise. Monolayers were transferred at a constant pressure onto mica on the upstroke using the Langmuir-Blodgett technique with a dipping speed of 1 mm/min. All transfer ratios were always close to 1. Compressibility modulus measurement was calculated using[138]:

$$C_s = -\frac{1}{A}\left(\frac{\partial A}{\partial \pi}\right)_T$$

Brewster Angle Microscopy (BAM). Brewster Angle Microscopy was carried out with an I-Elli2000 imaging ellipsometer (Nanofilm Technologies GmbH, Göttingen, Germany) equipped with a 50 mW Nd:YAG laser (λ = 532 nm). All experiments were performed using a 20× magnification with a lateral resolution of 1 μm. BAM experiments were performed at an incident angle of 53.15° (Brewster angle of water) and a laser output of 50% (analyzer, compensator and polarizer were all set to 0).

Atomic Force Microscopy (AFM). A Nanoscope IIIa (Digital Instruments, Santa Barbara, CA) was used to capture AFM images in air at room temperature using tapping mode at a scan rate of 1 Hz using etched silicon cantilevers frequency of ~300 kHz, a nominal spring constant of 20-80 N/m and tip radius of <10 nm. An oscillation operating at amplitude of 175 mV and medium damping (~25%) were employed for these measurements.

Grazing Incidence X-Ray Diffraction (GIXD). The GIXD experiments were performed at beamline 15-ID-C ChemMatCARS at the Advanced Photon Source (APS) in Argonne National Laboratory with the following parameters: X-ray beam wavelength of 1.239 Å, incidence angle of 0.09061°, horizontal size of 20 mm, and vertical size of 120 mm, leading to a beam footprint of 20 mm by 7.6 cm. The detector used was the two-dimensional Swiss Light source PILATUS 100K set to single-photon counting mode. Two sets of slits, one placed in front of the detector and the other placed 280.0 mm from the sample, were used to minimize intense low-angle scattering. Experiments were performed at the air/water interface of a 340 cm^2 Langmuir trough, where the monolayer was spread and then compressed at rates of 2 and 5 cm^2/min (equivalent to 0.5 and 1.3 $Å^2$/molecule min respectively) using a mobile barrier. The measured GIXD data is plotted as contour plots of the intensity as a function of both the horizontal (Q_{xy}) and the vertical (Q_z) scattering vector components. The lattice spacing d_{hk} was obtained from the in-plane diffraction data as $d_{hk}=2\pi/q_{xy}^{hk}$, where the Miller indices h and k were used to index the Bragg peaks needed to calculate the unit cell parameters for the in-plane lattice[111,139]. Raw data was extracted and patched using software developed by Wei Bu, beamline scientist at ChemMatCARS. The Bragg rods and peaks were fitted with Gaussian and Lorentzian function, respectively, using Origin lab graphing and analysis software.

3.4. Results and discussion

The isotherm of octadecylgallate (ODG) on ultrapure water (pH 5.5) exhibits a sharp increase in

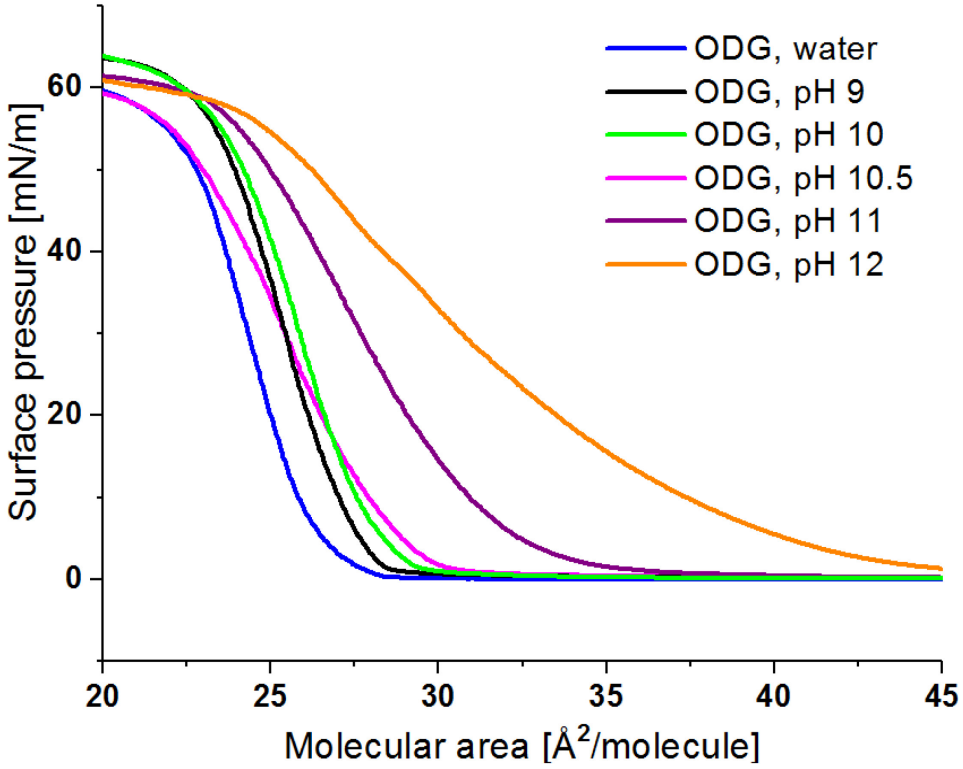

Figure 3-2 Surface pressure-molecular area isotherms of ODG as a function of subphase pH.

surface pressure at areas below 30 Å^2/molecule (critical area for onset of surface pressure), indicative of the formation of a condensed phase (blue isotherm, Figure 3-2). The surface pressure increases without evidence of a phase transition until film collapse at an area of approximately 23 Å^2/molecule and 50 mN/m. The film morphology was visualized using BAM (Figure 3-3). Already at high molecular areas and 0 mN/m surface pressure, large, condensed phase domains are visible, an indication of the strong intermolecular interactions between the headgroups. The domains are untextured (isotropic) and separated

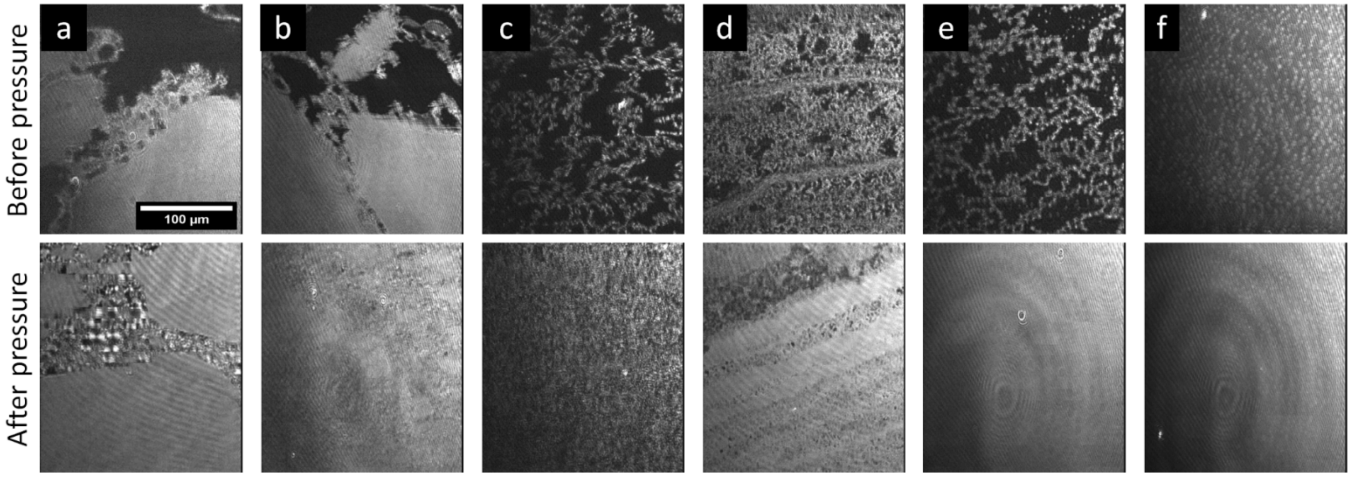

Figure 3-3 Brewster angle microscopy images of ODG, before and after the onset of pressure (0 mN/m) on various subphases with 10 minutes relaxation time: a) water, b) pH 9, c) pH 10, d) pH 10.5, e) pH 11, f) pH 12,

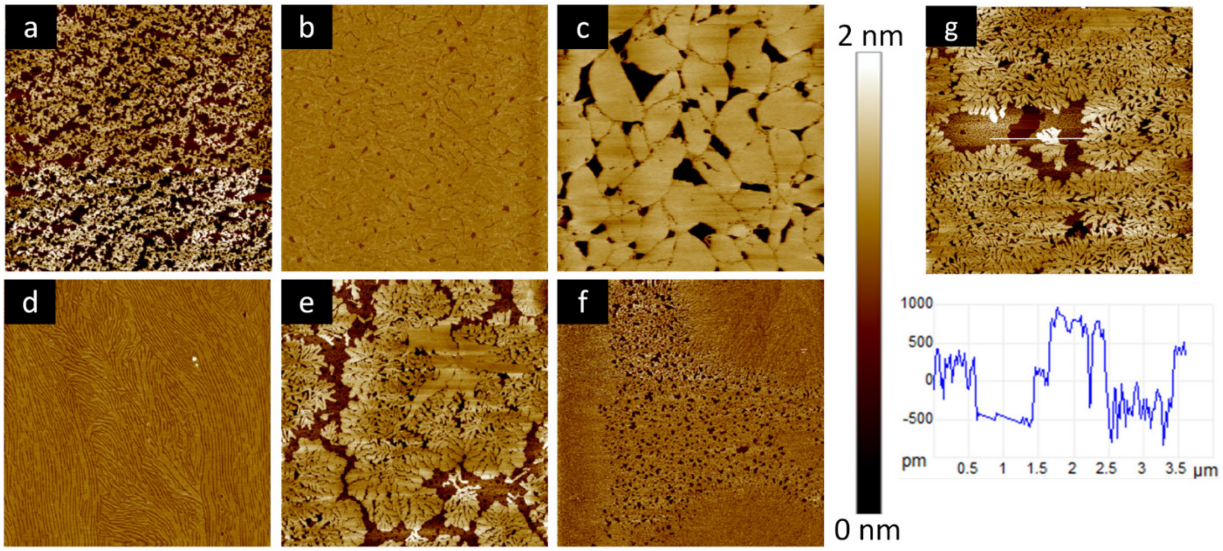

Figure 3-4 Atomic force microscopy images of ODG monolayers deposited by Langmuir-Blodgettry onto mica substrates at pressure of 1 mN/m with 10 minutes relaxation. Subphase and image sizes are: a) Water, 20 µm, b) pH 9, 5 µm, c) pH 10, 15 µm, d) pH 10.5, 15 µm, e) pH 11, 10 µm, f) pH 12, 10 µm, g) pH 11, 10 µm with height scan underneath.

by dark regions that comprise either gaseous phase or bare interface. If the solution is sonicated for 15 minutes before spreading, the domains are smaller, but the isotherm does not change. The pressure increases only after the domains are compressed to the point of contact. Most of the domains coalesce producing large regions of isotropic condensed phase that are larger than the field of view. Periodically, when the interstitial spaces between the domains appear in the field of view, smaller domains of the same

condensed material are visible, likely generated by compression of these interstitial spaces by the highly

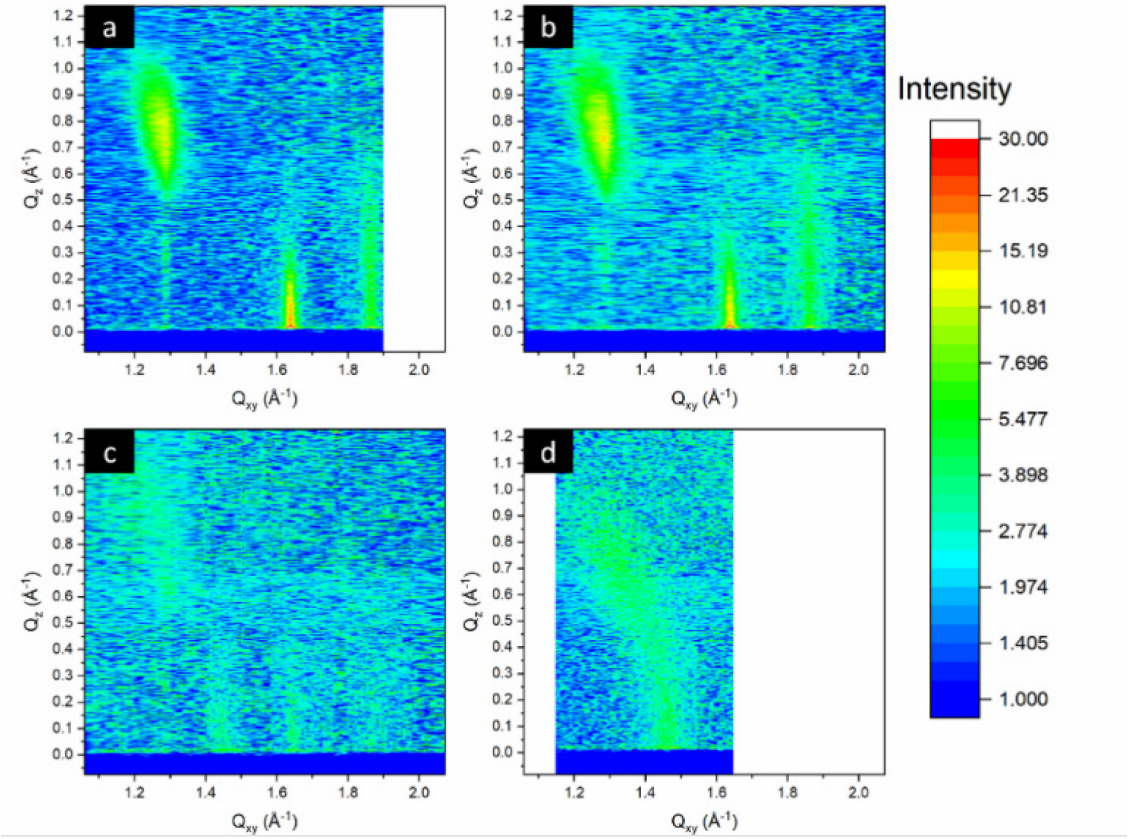

Figure 3-5 GIXD contour plot of X-ray intensity of ODG as a function of the in-plane (Qxy) and out-of-plane (Qz) vector components: a) water, 5 mN/m b) pH 9, 5 mN/m c) pH 11, with 10 minutes relaxation time, 20 mN/m d) pH 11 with 60 minutes relaxation time 5 mN/m.

rigid large domains (see Figure 3-3a). These smaller domains coexist with residual holes. Deposition of the monolayer onto mica by Langmuir-Blodgettry and analysis by AFM reveals clusters of small domains (Figure 3-4 a) that are approximately 1.2 nm above the background. Given the area coverage and the size of the domains observed by BAM and the lack of domains in this size range by AFM, it is presumed that the large, rigid domains break apart upon transfer.

In order to determine the tilt angle and lattice parameters of the condensed phase formed, GIXD measurements were carried out at different pressures (Figure 3-5 a and Table 3-1) and multiple diffraction peaks were observed. Two are located in the region normally associated with the first order peaks of the alkyl chain lattice, at Q_{xy} 1.28 $Å^{-1}$ and 1.63 $Å^{-1}$ (fitted peak positions and widths are provided in the Appendix, Table 1), additional peaks were observed at Q_{xy} 1.86 $Å^{-1}$ and 0.96 $Å^{-1}$ (Figure 3-6), the low

Q_{xy} peak will be discussed later. Using these peaks position to characterise the packing of the alkyl chains yields a centred rectangular unit cell with herringbone backing of the alkyl chains (lattice parameters are shown in Table 3.1). Notably, the unit cell and alkyl chain tilt angle

Table 3-1 Alkyl chain unit cell parameters derived from GIXD for ODG at room temperature on various subphases: a, b, γ are the unit cell dimensions reported using a rectangular unit cell nomenclature, t is the tilt angle relative to normal and the Ψ is the tilt direction relative to the unit cell where NN stands for a tilt towards nearest neighbor.

Water						pH 10 subphase					
Pressure (mN/m)	a (Å)	b (Å)	γ (°)	t (°)	Ψ	Pressure (mN/m)	a (Å)	b (Å)	γ (°)	t (°)	Ψ
5	7.66	6.40	90	39	NN	5	7.66	6.40	90	39	NN
20	7.66	6.37	90	38	NN	20	7.66	6.40	90	39	NN
40	7.59	6.35	90	37	NN	pH 11 subphase, 10 minutes relaxation time					
pH 9 subphase						1	7.64	6.40	90	40	NN
5	7.66	6.40	90	39	NN	20	7.59	6.34	90	35	NN
20	7.66	6.40	90	39	NN	pH 11 subphase, 60 minutes relaxation time					
						5	8.57	5.11	90	33	NN

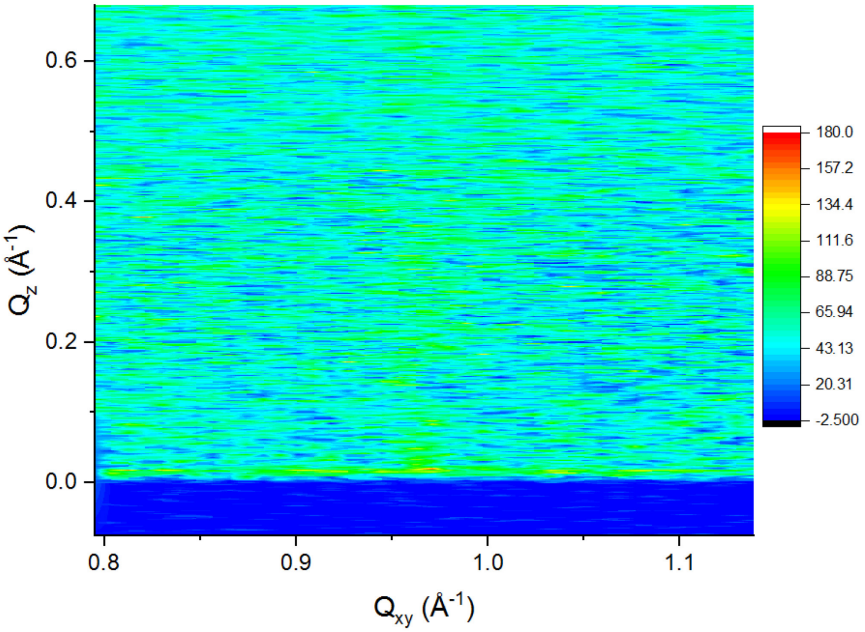

Figure 3-6 GIXD contour plot showing evidence of a low Qxy diffraction peak for ODG on a water subphase at 5 mN/m

change minimally as the film is compressed, suggesting that the molecules adopt a preferred orientation and organization already in the condensed phase domains formed immediately after spreading and compression serves only to remove the residual gaseous phase regions. This is consistent with the isotherms that do not show evidence of phase transitions.

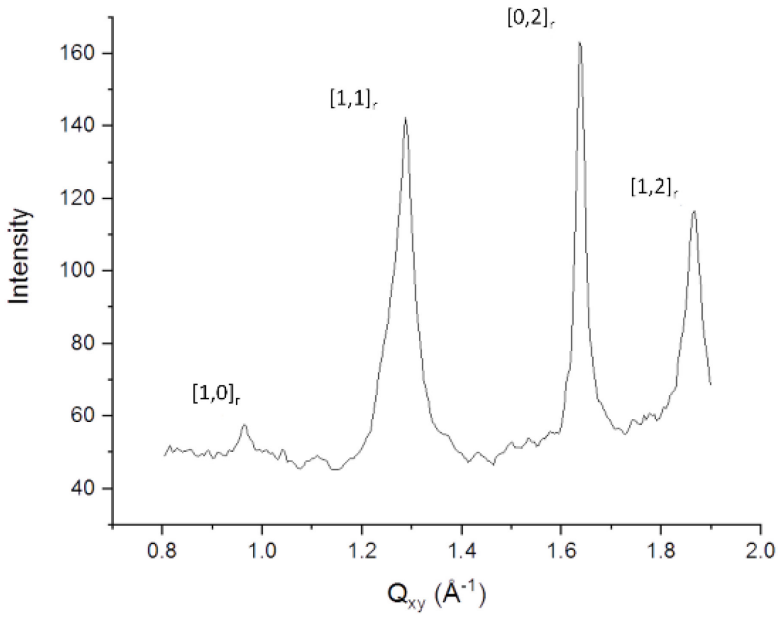

Figure 3-7 Integrated in-plane GIXD intensity for ODG on water at 5 mN/m. Proposed peaks are given relative to a rectangular lattice of headgroups. Note that the [1,1]r and [0,2]r headgroup peaks overlap with the [1,0]h and [0,1]h peaks of the alkyl chain lattice in a hexagonal notation.

Analysis of the distortion as a function of $\sin^2$ t (tilt angle) enables extrapolation of d_0, the distortion at zero tilt angle [50,113,140,141]. This analysis for octadecylgallate shows a non-zero value of d_0 at 0°, indicative of the herringbone arrangement[111,113] of the alkyl chains (Appendix Figure 1) which also correlates well with the high Q_{xy} position for the peak at 1.64 Å^{-1}. The peaks observed at Q_{xy} 0.96 Å^{-1} and 1.86 Å^{-1} correspond to the $[1,0]_r$ and $[1,2]_r$ peaks, respectively, with the peaks at Q_{xy} 1.28 Å^{-1} and Q_{xy} 1.63 Å^{-1} being indexed as $[1,1]_r$ and $[0,2]_r$, where the 'r' subscript denotes the rectangular cell indices (Figure 3-7 for indexed peak). However, the peak at Q_{xy} 1.86 Å^{-1} can only be fit with a full width at half (FWHM) maximum in the Q_z direction of 1.05 Å^{-1} (intensity in the Q_z direction in Figure 3-8), which corresponds to a scattering rod length of 5.4 Å[142] whereas the other peaks exhibit a fwhm of 0.28 Å^{-1} in better agreement with a tilted C18 chain. In the absence of any other phases, and given the large fwhm, this

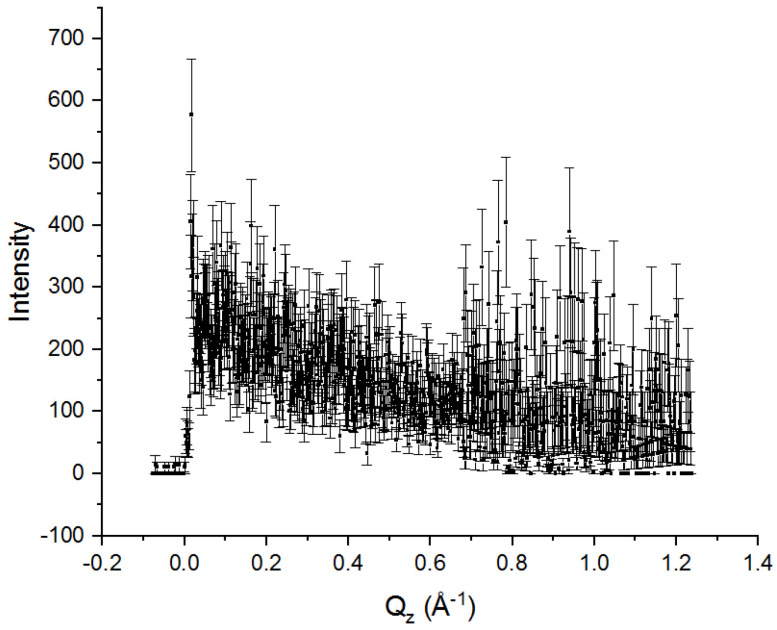

Figure 3-8 Intensity of the peak at Qxy 1.86 Å^{-1} along the Qz direction. Note that the increased noise at high Qz is an artifact of the lower number of points (coarse scan) at high Qz (above 0.65).

reflection is proposed to be the result of an organized headgroup layer. Such an organization was proposed based on simulations for ether-linked, mono- and di-hydroxy phenolic surfactants but not observed by GIXD[134]. Organization of the headgroup leads to the possibility that the centered rectangular herringbone arrangement arises due to a molecular lattice with a non-equivalent headgroup orientation. If the alkyl chains were also to be in herringbone arrangement, a corresponding strong $[1,2]_r$ peak should be observed at the same Q_{xy} = 1.86 Å^{-1}, but such a peak would need to be out-of-plane due to the tilting of the chain. We cannot preclude that this peak is buried under the large width peak at 1.86 Å^{-1} (Figure 3-8) and that the chains are also in a herringbone arrangement as might be expected given the A_0 (chain area normal to the long axis) is 19.2 Å^2, significantly less than the 20-21 Å^2 required for orientational disorder (the free-rotator phase). Notably, most reports of single chain surfactants of similar length that adopt a herringbone arrangement of the alkyl chains are for temperatures significantly below room temperature[139143]. There is a report of a herringbone structure at higher temperature for a longer chain length (C22) for which high surface pressures are required[144]. Therefore, if a herringbone organization of the chains is present, it must be driven by the strong headgroup non-covalent interactions.

Normally, the $[0,1]_r$ and $[1,0]_r$ peaks of a herringbone, centered rectangular unit cell are symmetry forbidden[118]. In this case, a weak $[1,0]_r$ peak is observed at Q_{xy} 0.98 $Å^{-1}$ (Figure 3-6), but the corresponding $[0,1]_r$ peak predicted to be at 0.8 $Å^{-1}$ was not observed (the full Q_{xy} scan range was from 0.8 to 2.4 $Å^{-1}$). Böhm *et al.*[143] observed both the [1,0] and [0,1] in the case of stacked multilayers, however both AFM and BAM exclude this possibility for our system. Thus the observance of the $[1,0]_r$ peak must derive from form factors in this direction that are not identical due to headgroup orientations. The lack of $[0,1]_r$ either implies that in this direction the symmetry is maintained and the form factors are still equivalent or the crystallinity in this direction is significantly weaker. Note that the Q_{xy} position of the $[1,1]_r$ peak of the headgroup or molecular superlattice is commensurate with the alkyl chain peak at Q_{xy} 1.28 $Å^{-1}$ which possesses a strong form factor around Q_z 0 $Å^{-1}$ and therefore cannot be explicitly identified.

Whereas herringbone higher order peaks for alkyl chains have been reported since the early 1990's for single chain fatty acids, molecular superlattices derived from strong headgroup organization leading to non-free rotation of the headgroup are less common. However, the strong intermolecular hydrogen bonding and π-stacking interactions between the gallate headgroups could be sufficient to induce ordering in the headgroup region. Such a hydrogen bond network was previously proposed by Pascher *et al.*[145] in leaflet of bilayer of sphingolipid, where the hydrogen bond network is inferred from crystal diffraction and by Stefaniu *et al.*[146,115] for the sugar headgroup ordering in glycosylphosphatidylinositol monolayers. A contributing factor here is the commensurate size of the headgroup with that of the single alkyl chain, whereas double chain surfactants or lipids may be bulky enough to keep the headgroups far enough apart to prevent long-range orientational order.

In order to probe the impact of head group protonation state on this network, experiments were performed over a range of subphase pH values from 7 to 12. Increasing the subphase pH should lead to deprotonation of the phenol and a charged headgroup which would modify the interaction between the surfactants. At pH 7 and pH 8, no discernible changes in the isotherm or morphology were observed (data not shown). At pH 9 the isotherm shifts to higher molecular areas and shows an increased collapse pressure, close to 60 mN/m (Figure 3-2). There is some disagreement in the literature over the solution pKa of gallic acid, but there is consensus that the first hydroxyl to deprotonate is the *para*- position at a pKa of 8.2[147] or 8.7[148,149]. It is however important to note that pKa is environment dependent and that the headgroup pKa in a monolayer can be substantially different from the solution pKa[150]. Therefore a

modification in isotherm behavior at subphase pH 9 is in reasonable agreement with the deprotonation of the *para*-hydroxyl. This discrepancy in the literature pKa values is more pronounced for the *meta*-positions, with first position being ascribed three possible pKa values: 10.4[149], 10.7[147] and 11.4[148] and the second *meta*-position deprotonation also being ascribed a pKa of 11.4[149] or 13[147,148]. Herein, experiments were not carried out above pH 12, but the isotherms support the idea of a progressive change in *meta*-position protonation state over a pH range of 10.5-12 (Figure 3-2). As might be expected, increasing the extent of deprotonation, and hence the headgroup charge, leads to an expansion of the film due to electrostatic repulsion and consequent shifts to higher molecular areas.

At pH 9, BAM imaging shows a similar morphology as observed on water (Figure 3-3) however the large domains appear more frayed at the edges (Figure 3-9); the increased repulsion brought about by the deprotonation of the headgroup is most likely weakening the integrity of the domains. Similarly, upon compression, the interstitial spaces never fully coalesce which may be due to the highly rigid nature of

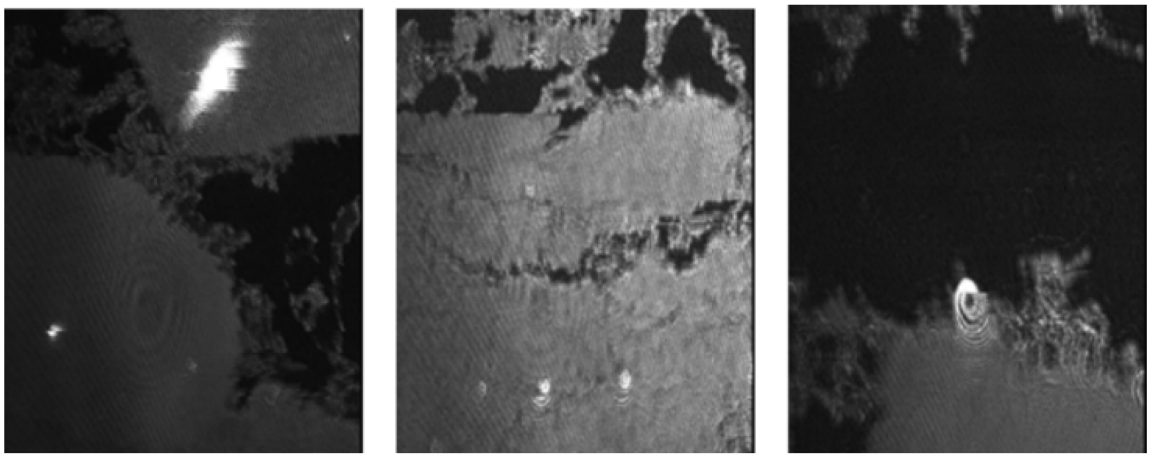

Figure 3-9 BAM images of ODG on a pH 9 subphase taken before onset of pressure

the domains and the increased charge. By BAM, these are visible as regions between isotropic domains that are less homogeneous and still contain small holes. AFM of deposited films (Figure 3-4b) reveals that the large condensed phase regions themselves comprise smaller domains that have not coalesced, evident from the observable grain boundaries and trapped holes comprising either gaseous phase or effectively bare mica. These grain boundaries may induce sufficient flexibility of the film that deposition can occur without the fragmentation that was observed for film transfer from water. Deposition at elevated pressure shows that these domains can fuse with each other's (Figure 3-10). Despite the morphological

changes, GIXD of ODG on a pH 9 subphase shows an organization almost identical to the one found on ultrapure water (Figure 3-6, to be discussed later).

At pH 10 and above, large changes in morphology are observed both at the air-water interface and in deposited films. The large domains seen by BAM at lower pH values are replaced by smaller domains that form a mesh-like structure (Figure 3-3). If compressed, they do not coalesce into a uniform condensed phase, instead forming close-packed small domains of various shapes. AFM of films deposited at low

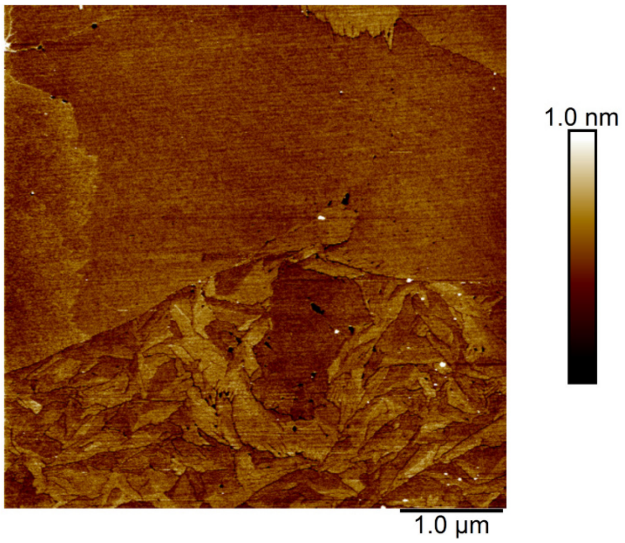

Figure 3-10 AFM image of ODG deposited from a pH 9 subphase at 20 mN/m

pressure (Figure 3-4c) shows small (< 4 microns) distinct domains separated by small regions of gas phase. This, combined with the BAM and AFM image at higher pressure (Figure 3-11), indicate that the domains do not fuse even when compressed.

Despite very different morphologies, the isotherms for ODG on pH 9 and pH 10 subphases are very

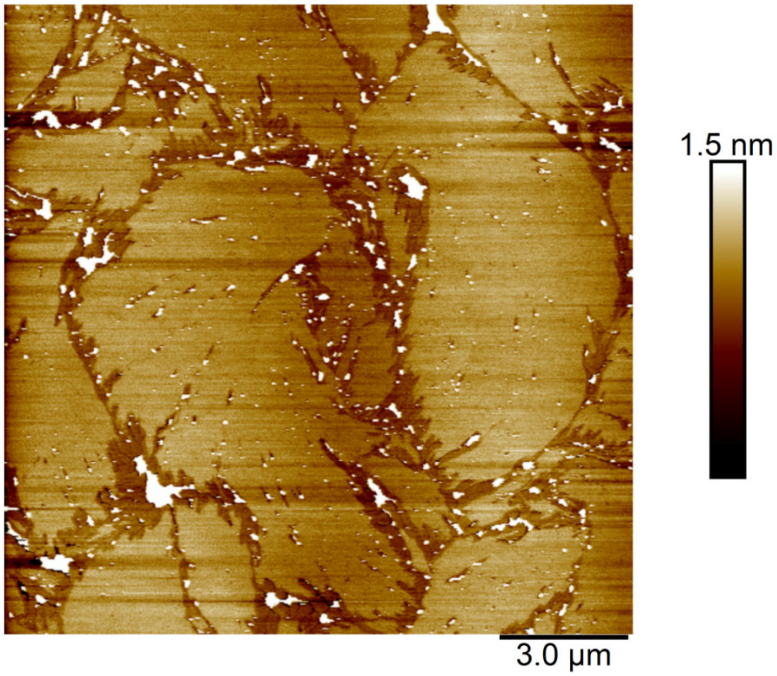

Figure 3-11 AFM image of ODG deposited from a pH 10 subphase at 20 mN/m.

similar. The change in subphase pH is concomitant with a 10-fold change in ionic strength (from 10^{-5} M to 10^{-4} M). To investigate this, NaCl was added to a pH 9 subphase such that the concentration of Na^{+} ions was the same as for the pH subphase (Appendix Figure 2). The isotherm obtained are again similar, but the film morphology resembles that obtained on pH 9 (data not shown), confirming it is the pH changes that alter the morphology not the ionic strength.

The GIXD measurements yield almost identical lattice parameters for water, pH 9 and pH 10 subphases (Table 3.1). Therefore, the morphological changes seen by BAM and AFM do not originate from a modification of the surfactant organization and may result from the increase in charge of the domains themselves. As the headgroup become deprotonated the domains will also experience greater inter-domain charge repulsion producing smaller domains that repel hindering coalescence and favoring small domains[151,152]. Given the similarity of the isotherms and the Q_{xy} values from GIXD, small domains at subphase pH 10 must generate the same area coverage of the surface as the larger domains at pH 9. Assuming the *para*- hydroxyl position is the first hydroxyl to deprotonate, as is the case in solution[149] for gallic acid, this could potentially have less impact on a hydrogen bond network that exists between the

neighboring surfactant *meta*-hydroxyls. This would suggests that the *meta*-positions do not begin to deprotonate until pH> 10.

The BAM morphology comprising chains of small domains persists at pH 11 and becomes more pronounced. The isotherm shifts to significantly higher molecular areas. Unlike at pH 10, increasing the pressure leads to a uniform condensed phase in BAM imaging (Figure 3-3e). However, AFM (Figure 3-4e and 3.4g) reveals a very different internal domain morphology compared to pH 10 (Figure 3-4c). The domains seen by BAM at 0 mN/m are actually composed of small dendritic, snowflake-like features with many branches that continuously split. Grooves are apparent within the dendritic arms (Figure 3-4g) and have a nominal depth of 0.2 nm, although given their width this may be tip-limited and thus inaccurate. Typically, the observation of dendritic features coincides with domain formation and growth at a LE-C phase transition plateau[153] which can relax into circular domain given enough time[154]. Similarly, changing the relative contributions of highly orienting, directional non-covalent interactions (via changing the pH[155] or temperature[156]) versus line tension also impacts dendrimer formation. Careful examination of Figure 3-4g reveals multiple co-existing phases, the region surrounding the dendrites comprises two phases. The height difference between the dendrites and the lowest phase is approximately 1.0 nm while the intermediate phase displays a height difference to the lowest phase of 0.7 nm. Periodic holes within the lowest phase confirm that this is not the mica substrate (Figure 3-12a). It would appear that two different condensed phases are formed and that these co-exist with a liquid-expanded phase. In agreement with BAM imaging, the AFM of a film deposited at 20 mN/m (Figure 3-12b) shows that the coexistence persists over the timescale of an isotherm, although the phases does begin to coalesce.

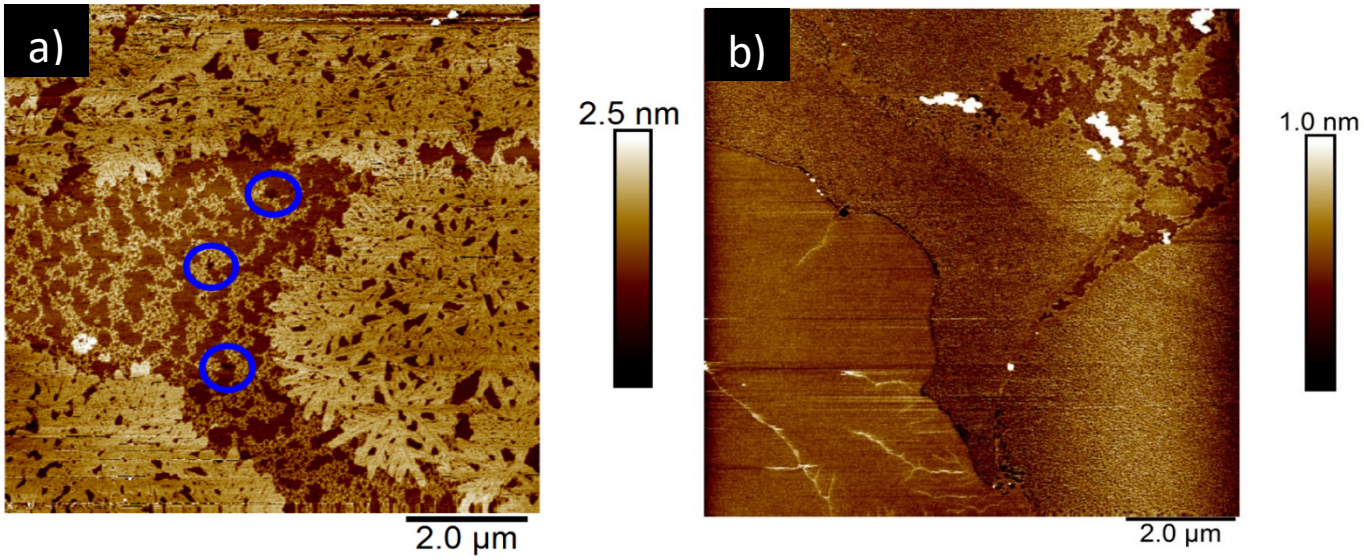

Figure 3-13 a) AFM image of ODG deposited from pH 11 subphase at 1 mN/m, hole in deepest layer circled in blue, approximate depth of 0.9 nm b) AFM image of ODG deposited from pH 11 subphase at 20 mN/m.

The co-existence of multiple phases was studied using GIXD. The diffraction pattern for ODG on a pH 11 subphase shows peaks associated with multiple diffraction patterns. One set of peaks appears at the same approximate positions as observed at the lower pH values (peaks at Q_{xy} 1.28 $Å^{-1}$, 1.64 $Å^{-1}$ and 1.86 $Å^{-1}$), although the peaks are significantly weaker. Additionally, the data shows the appearance of a new set of peaks (Figure 3-5c) corresponding to a phase with a lower tilt angle (peaks at Q_{xy} 1.35 $Å^{-1}$ and 1.46 $Å^{-1}$) that yield the unit cell parameters listed in Table 3.1 for the 60 minutes relaxation time (note

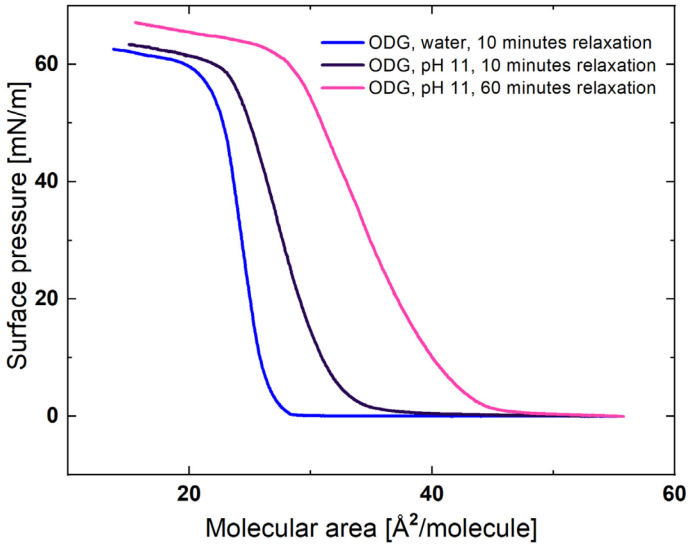

Figure 3-12 Surface pressure-molecular area isotherm of ODG at pH 11 with and without additional relaxation.

that the unit cell is non-herringbone and centred rectangular). The co-existence of two phases was observed both at low (1 mN/m) and high (20 mN/m) pressures. Notably, the height difference between the two condensed phases obtained by AFM was 0.3 nm which corresponds well to the estimated height difference for chains tilted at 40° and 33°.

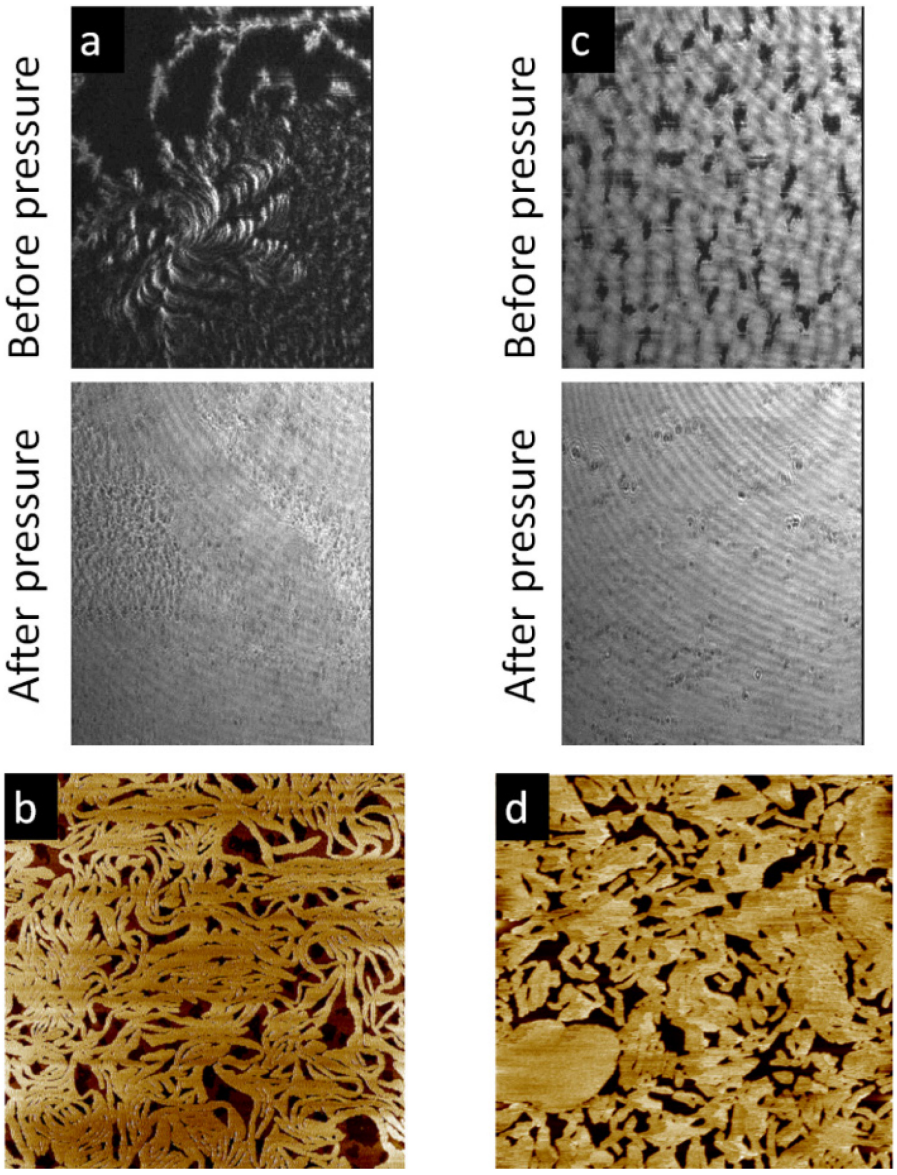

Figure 3-14 BAM and AFM of ODG after 60 minutes relaxation time at subphase pH 10.5 a), b) (size of 10 µm, deposition at 1 mN/m) and pH 11 c), d) (size of 5 µm, deposition at 1 mN/m).

According to the Gibbs phase rule, in a one component system, multiple thermodynamically stable phases can theoretically only coexist at phase transitions but not over broad ranges of surface pressures. In practice, the phase transition can be broader than a single surface pressure as the compression speed renders the film not at thermodynamic equilibrium. However such coexistence over broad ranges of surface pressures could be due to a slow rearrangement of the surfactant due to the increase in pH or separation into two phases, one rich in the deprotonated component and one rich in the protonated component. To test this, the film was allowed to relax for 60 minutes prior to compression. This shows a complete loss of the peaks associated with the higher tilt angle phase (Q_{xy} 1.28 $Å^{-1}$ and 1.64 $Å^{-1}$) and an increased intensity for the lower tilt angle phase (Figure 3-5d). This relaxation of the film also induces a change in the isotherm to higher molecular areas (Figure 3-13). Film relaxation also alters the morphology observed by BAM with rounder, larger domains that never fully coalesce (as indicated by the residual holes at high pressure, Figure 3-14), hence the shift to larger average molecular areas, despite a lower tilt angle. In agreement with GIXD, AFM (Figure 3-14d) confirms that relaxation yields a film comprising only two distinct heights, attributed to a single condensed phase with surrounding low density region (gaseous phase). These results confirm that the multiple phases arise from slow kinetics rather than impurities.

Hossain *et al.* saw similar dendritic features by BAM for a monolayer of di-n-dodecyl hydrogen phosphate which, upon relaxation at constant pressure, relaxed into circular shaped domains[154]. In our case the dendritic phase is the less tilted (higher) phase and appears to grow initially at the expense of the more tilted (lower) phase. This less tilted phase exhibits a fast initial dendritic growth that is not kinetically stable and thus, as the film relaxes, the dendrites re-organize to form more rounded domains, highlighting the competition between directional growth due to strong intermolecular interactions and line tension. Notably, the phase that emerges upon relaxation of the film no longer exhibits the high crystallinity or the herringbone packing observed at lower pH values (Figure 3-5a and d). Keeping in mind that the pKa for the second deprotonation in the meta-position has been reported to be in the range of 10.4 to 11.4 and assuming the *para*-hydroxyls to already be majority deprotonated[149], these changes are likely attributable to a second deprotonation, i.e. deprotonation of one of the *meta*-hydroxy groups. Given the film is spread from chloroform into a highly aggregated state (at high molecular areas) onto a subphase of high pH, one has to assume a component of the kinetics is the rate of deprotonation which would require disrupting

existing strong interactions, keeping in mind that in a condensed film, the gallate cannot be considered in dilute solution. The second component that must be considered is a potential re-organization from the deprotonation in the *para*- and *meta*- positions to deprotonation at both *meta*-positions which would limit the internal charge repulsion and alter the headgroup dipole. The former (*para*-/*meta-deprotonated*) has a strong headgroup dipole which could have a preferred growth direction and could explain the dendritic growth pattern, while the latter (*meta*-/*meta-deprotonated*) has no net headgroup dipole (parallel to the surface) thus could result in the line-tension dominated, circular domains. Transfer from one phase to another must occur via dissolution from the domain edges into an intermediate liquid-expanded phase as observed by AFM, a process similar to the concept of Ostwald ripening or solution mediated polymorphic phase transformation.

In order to probe this pH-induced transition, an intermediate pH value of 10.5 was also studied and also show the time-dependent reorganization. Branching and spiral patterns are visible by BAM and AFM (Figure 3-14a and b) supporting the proposed second deprotonation around this pH. If the film is compressed with minimal wait time, the domains clearly coalesce into long, highly oriented, striated regions (Figure 3-3d). Compression after longer relaxation time (Figure 3-14a) generates a greater coverage in uniform condensed phase although areas resembling the smaller domains observed for pH 10 persist. AFM imaging (Figure 3-4d) also shows a highly striated film, albeit on a completely different length scale. The observed crevasses are of varying length and average 0.4 nm deep, although again, this depth measurement is likely tip-limited due to their small lateral size. Clearly, strong orienting headgroup interactions dominate over line tension in defining the domain shape. The lack of coalescence of these long domains is likely due to increase repulsion between surfactant domains[151]. The lower proportion of di-deprotonated headgroups mixed with the mono-deprotonated would then generate elongated, strand-like domains even after relaxation (Figure 3-14b). This also demonstrates that the changes observed at pH 11 with long relaxation times are not due to the small change in pH from CO_2 absorption, which will lower the pH, since longer relaxation times at pH 11 lead to rounder domains, not long striated ones. The proposed deprotonation states and associated molecular re-organizations, both within the molecule and within the film, leading to this phase behaviour are under investigation using computational methods.

At pH 12, multiple small bright domains are visible by BAM (Figure 3-3f) although there does not appear to be chains of domains forming. Notably the contrast between the domains and the continuous

matrix is significantly reduced. As the pressure increases this background gets brighter until it is the same brightness as the small circles and the morphology become homogenous. AFM reveals that the domains seen by BAM are regions of higher density of condensed phase, these are also dendritic in appearance, especially at the edges, but they are visibly distinct from those seen at pH 11. These are surrounded by regions of small nanodomains co-existing with gas phase, hence the similarity in optical properties seen by BAM to the domains. As the pressure increases the visible holes, which are trapped remnants of gas phase, are eventually excluded as the film fully coalesces, leading to full loss of contrast in BAM. GIXD measurements indicate that only the lower tilt angle phase (seen at pH 11 with long relaxation time) is formed with no evidence of the higher tilt angle phase or headgroup ordering (data not shown). The structure is not included in Table 3.1 because the peaks, although evident, are too weak to be fit accurately. Given the amount of condensed phase found by AFM imaging, the weaker peaks must be attributed to extremely low correlation lengths. The presence of only one phase (low tilt angle) indicates that at higher

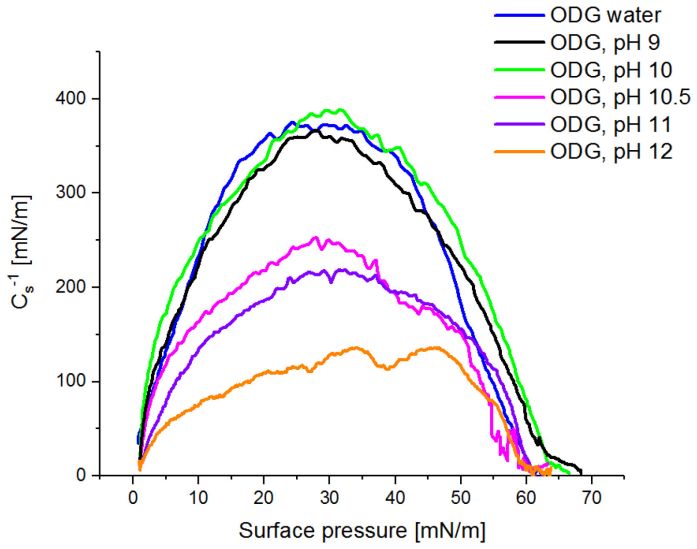

Figure 3-15 Compressibility modulus of ODG as a function of subphase pH.

pH, the rate of deprotonation and kinetic re-arrangements increases. Time dependent studies were performed but show no change to the morphology or structure indicating that this polymorph is stable for relaxation times up to 12 hours.

The impact of pH on the film properties is clearly mapped in the compressibility modulus as a function of pH (Figure 3-15). Three distinct regimes are observed that, according to our proposed model, would correlate with (i) predominantly protonated and mono-deprotonated (water, pH 9, pH 10), (ii) mixed mono- and di-deprotonated (pH 10.5, pH 11) and (iii) predominantly di-deprotonated (pH 12) headgroups. The first two regimes correspond in compressibility moduli to condensed phases[138,157], (C_s> 200 mN/m in all cases), however as the charge repulsion of domains increases and hinders full coalescence, the compressibility modulus decreases.

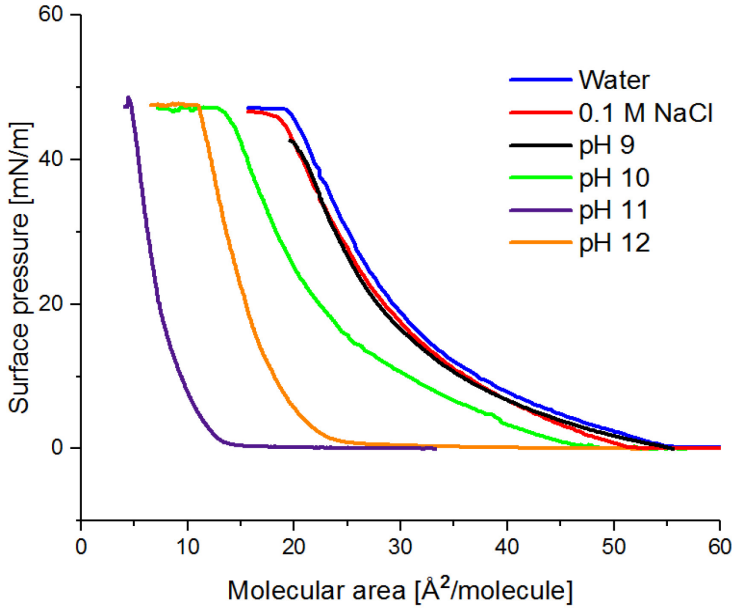

Figure 3-16 Surface pressure-molecular area isotherms of lauryl gallate as a function of subphase.

In order to determine the effect of chain length on the pH induced phase behaviour, a shorter analogue, lauryl gallate, was studied. Lauryl gallate films on ultrapure water exhibit an isotherm typical of a liquid-expanded phase (Figure 3-16) with a critical area for pressure onset at 55 Å^2/molecule. It remains in this phase until film collapse at 20 Å^2/molecule and 47 mN/m. This collapse area is larger than that of ODG, but not significantly, suggesting there may be some solubility of lauryl gallate in the subphase which has been reported for surfactants with a C12 alkyl chain[158]. AFM measurements of films deposited by the Langmuir-Blodgett method on mica, confirm a single phase with a flat, featureless surface (data not shown). As a result, the headgroups should not be in such close proximity as observed with octadecyl gallate. In contrast to ODG for which the headgroup deprotonation at pH 9 induces a shift

of the isotherm, there is no significant change in molecular area for lauryl gallate at pH 9 compared to ultrapure water (Figure 3-16). Similarly, the addition of 0.1 M NaCl has no impact on the widely spaced headgroups whereas with the close-packed ODG, insertion of the counterion into the headgroup region expanded the film (Figure 3-16 and Appendix Figure 2). The first significant change in the isotherm area occurs at pH 10 (for ODG the first noticeable shift was observed at pH 9). This may result from one of two factors, either the greater headgroup spacing enables water and counterion screening of the charge on the *para*-hydroxy and weakens the electrostatic repulsion or there is a difference in the first pKa due to the differences in phase. Notably, the isotherm shifts to smaller molecular areas in contrast to ODG which exhibited a shift to higher molecular areas with increasing pH. In this case, deprotonating the *para*-position generates an ion-dipole interaction which is strong enough to bring the molecules closer together, whereas in ODG the charge repulsion in an already close-packed system generates an increase in molecular area.

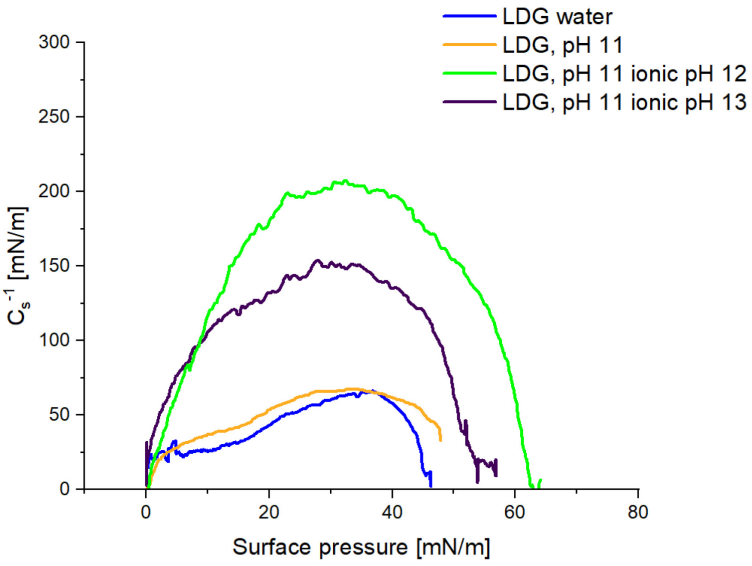

Figure 3-17 Compressibility modulus of lauryl gallate as a function of subphase, NaCl was added to increase the ionic strength of the subphase to be equivalent to subphase of higher pH.

At pH 11, there is a larger shift to smaller molecular areas, this time accompanied by a change in isotherm shape; it would be expected that the isotherm exhibits a change in compressibility modulus[138] corresponding to a condensed phase, however, there is no apparent change when compared to a film on ultrapure water (Figure 3-17). Given the molecular area values are lower than what can be reasonably expected for a single alkyl chain[159] this suggests that the films is not a true insoluble monolayer and that

at this pH, solubility becomes a significant factor, which is reflecting in the compressibility modulus remaining that of a liquid expanded phase despite the low apparent molecular area. To counter the effect of solubility, the subphase salt concentration and ionic strength was increased to reduce the surfactant dissolution[160]. Figure 3-18 shows the isotherms for lauryl gallate at pH 11 with sufficient NaCl to bring the ionic strength equivalent to that of the subphase adjusted to pH 12 (0.01 M) and 13 (0.1 M) with NaOH. These isotherms result in a clear increase in compressibility modulus which is highest for pH 11 with 0.01 M NaCl. This supports the idea that the ion-dipole headgroup interactions are, at this pH, bringing the headgroups closer together, since the addition of counterions into the headgroup region expands the film[161].

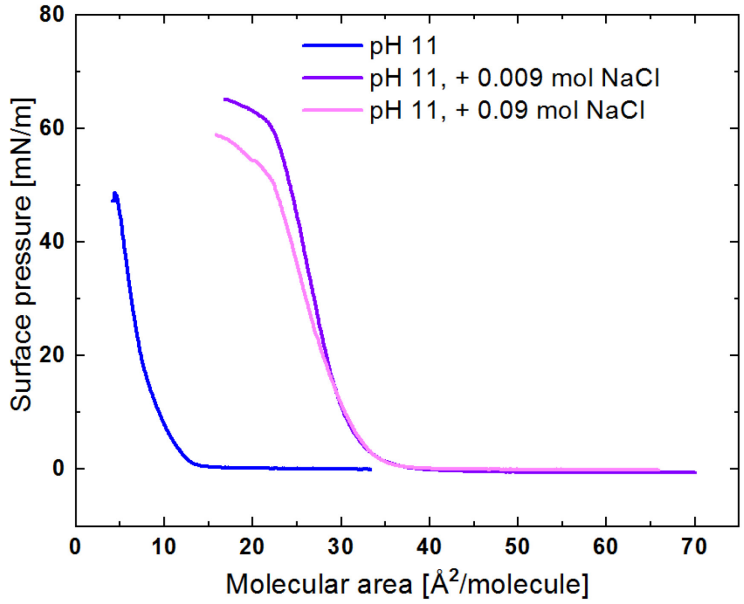

Figure 3-18 Surface pressure-molecular area isotherm of lauryl gallate on pH 11 subphase with ionic strength of higher pH adjusted with NaCl.

Despite the condensing effects noted, no discernible features were observed using BAM (data not shown). To ascertain whether or not a condensed phase is formed, the monolayer was deposited by Langmuir-Blodgettry onto mica at 1 mN/m for characterization using AFM (Figure 3-19). Unlike the deposition at neutral pH, the film is not homogeneous but rather exhibits a large number of small holes with an average depth of 0.5 nm and diameter of only a few nanometers. It is not clear if the holes are present at the air-water interface or if they are induced by the transfer as these features are too small to be

observed by BAM. Transferring the monolayer at higher pressure, 30 mN/m, leads to a smooth surface (data not shown).

Isotherms on a pH 12 subphase show a critical area intermediate between that on water and on a pH 11 subphase (Figure 3-16). As was seen at pH 11 and high salt concentrations, the ionic strength of pH 12 (0.01 M NaOH) will limit the solubility of the surfactant; this reduction in solubility accounts for the difference in isotherms between pH 11 and 12. This is reinforced by AFM imaging of a film deposited from a pH 12 subphase which shows a topology very similar to those seen at pH 11 (Figure 3-19).

3.5. Conclusions

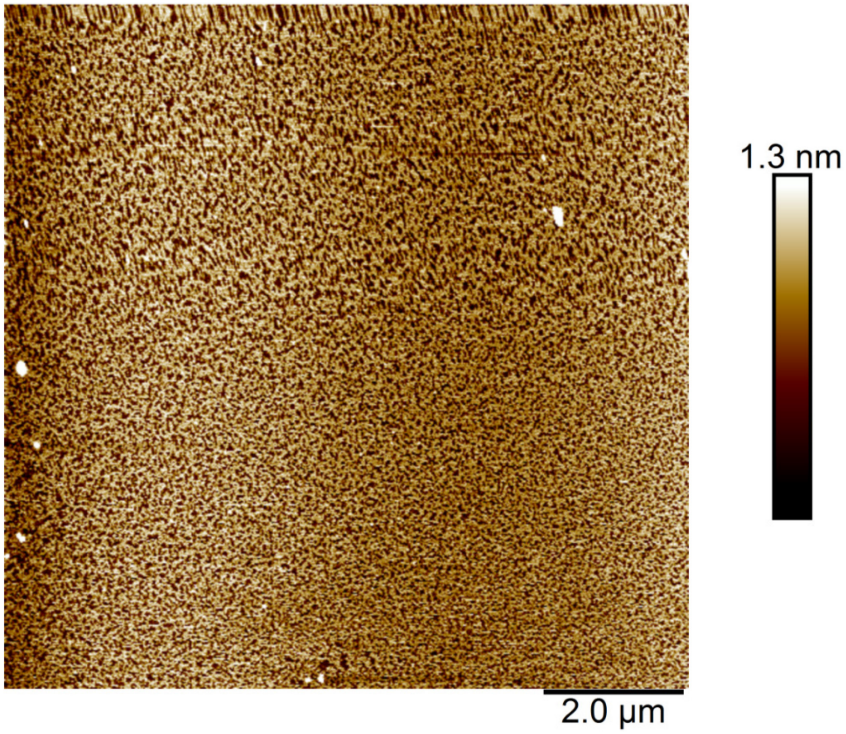

Figure 3-19. AFM image of lauryl gallate deposited from pH 11 subphase at 1 mN/m.

The air-water behavior of monolayer comprising a phenolic surfactant was investigated as a function of subphase pH and chain length. ODG on all subphases up to pH 10 exhibits evidence of strong headgroup ordering both in morphology (high aggregation at high molecular areas) and structure, as revealed by GIXD measurements. For the latter, additional peaks were attributed to a molecular superlattice which exhibits herringbone packing of the headgroups but not necessarily the alkyl chains. Initial deprotonation, presumed to be the *para*-position, has no impact on the intermolecular organization

and structure but does impact morphology as revealed by BAM and AFM. As domain acquire a greater charge, they becomes smaller and resist coalescence due to inter-domain electrostatic repulsion. At high pH, a second deprotonation is presumed to occur since stronger impacts on morphology, structure and relaxation time are observed. Due to the slow kinetics of re-organization, multiple phases are observed to co-exist over a broad range of surface pressures. This has been attributed to the kinetics of deprotonation in a condensed phase and possible internal re-distribution of the internal charges on the headgroup. The generation of a strong headgroup dipole favors highly directional growth in films containing the proposed di-deprotonated headgroup, at the expense of line tension. Moreover, the greater charge promotes the loss of the molecular superlattice organization seen at lower pH in favor of a very different unit cell that does not show signs of herringbone packing. To our knowledge, the impact of strong orientational ordering of headgroups has not previously been shown to affect the kinetics of deprotonation and resulting phase behavior in Langmuir monolayers. Notably, the hindrance of deprotonation due to the crystalline headgroup region, leads to an unusual condensed phase growth mechanism in which the kinetics of the system leads to the formation of a liquid phase as an intermediate in the transition from one condensed phase to another. This is in effect a 2D analogy to the transformation between different polymorphs in the presence of a mother liquor, except that in this case the mother liquor is not a solute and solvent but rather a liquid form of the same material.

In contrast to ODG, initial deprotonation of the *para*-hydroxyl of lauryl gallate, which forms a liquid-expanded phase on water due to the decreased van der Waals interactions, leads to a film contraction due to the increase in headgroup interaction strength, brought about due to the replacement of dipole-dipole interaction with stronger ion dipole. This demonstrates how the same modification, deprotonation, can have very different impacts on a monolayer depending on the monolayer phase. The ability to use subphase pH and chain length to finely tune the intermolecular interactions, headgroup dipole moments and line tension provides the means to easily access a variety of domain morphologies even while keeping the internal structure the same. Understanding interplay of such thermodynamically and kinetically-driven processes will guide the design of new building blocks for functional surface coatings and self-assembled structures.

Chapter 4. ω-Thiolation of phenolic surfactants enables controlled conversion between extended, bolaform and multilayer conformations

4.1. Abstract

The self-assembly of ω-thiolated surfactants onto gold is a well-studied phenomenon, however control over the final organization within the thin films is either limited or requires extensive pre- and post-deposition chemical modifications. Langmuir-Blodgett deposition from the air-water interfaces affords a high degree of control over lateral organization within the film, yet it is generally employed to create physisorbed, soft matter films. Despite this, relatively little is known about the impact of the ω-thiolation on the air-water monolayer organization. Here we show that the introduction of a terminal hydrophilic thiol on a phenolic surfactant does not necessarily disrupt a highly organized film nor does it necessarily induce a bolaform conformation at the interface. We show that the relative proportions of different conformations can be controlled using pH, relaxation time, surface pressure and combinations thereof. Moreover, at high pH, the system undergoes a monolayer-to-multilayer transition wherein well-defined multilayer structures and morphologies are generated. These multilayers appear to comprise a single bolaform conformation atop an extended chain condensed phase. We demonstrate that these structures can be transferred using Langmuir-Blodgett deposition demonstrating that combining these two approaches has the potential to achieve greater control over the functional properties of robust, chemisorbed films.

4.2. Introduction

Phenols are the dominant functional moiety of the class of natural compounds called tannins which can bind histidine-[16] and proline-rich proteins and chelate metals[2]. Combining the phenol functionality into a building block for thin film self-assembly provides a route to conferring this functionality to a solid surface for biosensing[162], antifouling[163], metal binding[23,164], membrane binding[25] and oil repellant[165] applications. However, protein binding requires insertion of the histidine or proline residue[9] between the

phenols moiety, hence the strength and specificity of such binding is dependent on the distance between the phenols, which must therefore be carefully controlled. Thus, while self-assembled monolayers using thiol-functionalized molecules that chemisorb to gold surfaces[59], provides a facile fabrication route and highly reproducible films, generating a homogeneous surface coverage with a high degree of control over lateral spacing is challenging. One approach is to simply change the terminal functional group of a thiolate bearing surfactant to a larger functional group which then defines the lateral spacing[58] and which can later be functionalized. However, this does not necessarily provide the means to generate a homogenously spaced, low-density film required for an analyte such as a proteins to bind. Such a film can be achieved by self-assembling a surfactant with a removable spacer[166,167], wherein this moiety controls the lateral spacing upon chemisorption and can be subsequently cleaved in mild conditions leaving behind a smaller functional group. However, generating the terminal phenol then requires an additional step of chemical modification. In this work, we investigate the possibility of pre-organising thiol-terminated phenol surfactants at the air-water interface and their subsequent deposition by Langmuir-Blodgettry as a means to control the lateral spacing in the film[87].

Surfactants can be spread at the air-water interface at molecular areas that correspond to a monomolecular films[168]. The film is then compressed to alter the organization and lateral spacing between the surfactants. This method introduces multiple variables that can influence the lateral spacing within the film, including surface pressure[169], subphase pH[170], temperature[46] and subphase composition[171]. Our previous work showed that the lateral organization, on both the microscopic (domain morphology) and nanoscopic (surfactant organization within domains), can be modified in films comprising non-ω-thiolated phenolic surfactants by varying the subphase pH, wherein headgroup protonation state alters the intermolecular interactions[172].

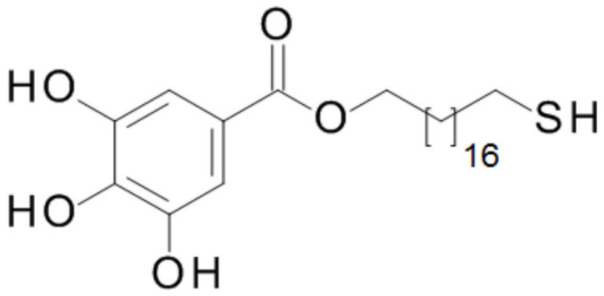

Figure 4-1 18-mercaptooctadecyl 3,4,5-trihydroxy benzoate (ω-thiolated octa-decylgallate or ODG SH).

Despite the wealth of literature on both self-assembly of thiolated surfactants on gold and Langmuir-Blodgett (LB) depositions of non-thiolated surfactants (reviewed, for example by Matharu et al.[173]), there are relatively few studies reporting the Langmuir monolayer behaviour of ω-functionalized surfactants[84,87,89]. Herein, we investigate the impact of adding an ω-thiolation of octadecylgallate to form 18-mercaptooctadecyl 3,4,5-trihydroxy benzoate, (ODG SH, figure 4-1) on its Langmuir monolayer behaviour and its subsequent deposition onto gold substrates.

4.3. Materials and methods

Materials. 18-mercaptooctadecyl 3,4,5-trihydroxy benzoate (ODG SH) was synthesized as reported in the supplemental information. Ultrapure water (resistivity of 18.2 MΩ/cm) was obtained from an EasyPure II LF system (Barnstead, Dubuque IA). The spreading solutions were prepared using chloroform (HPLC grade, trace of ethanol as preservative) from Fisher Scientific Company. Mica (grade V1) used in the AFM deposition was purchased from Ted Pella Inc. and freshly cleaved before each measurement. Gold substrates were purchased from evaporated metal films (Ithaca, New York) product # TA134 with thickness of 100 nm, with a titanium binding layer of 5 nm. These were cut into slices of approximatively 1 cm by 2.5 cm. Prior to deposition these were cleaned using a UVO-cleaner model 342 (Irvine, California) for 15 minutes. The slides used for air-water deposition were then left in ethanol for 1 hour to be chemically reduced[61] and become hydrophobic. Slides were re-used by removing the monolayer using 0.5 M $NaBH_4$ (Fisher chemical) in 1:1 ethanol:water[174] and cleaned by ozone for 1 hour. Templated stripped gold was made by depositing 100 nm of gold onto a silicon wafer and glued to a glass slide using UV activated glue (Norlan optical adhesive). The slides were treated the same as the purchased slides for air-water deposition purposes (15 minutes ozone clean, 1 hour in ethanol) but were not re-used.

Isotherm measurements. Monolayers were spread from a chloroform spreading solution (1 to 1.5 mM) on two different types of subphases: ultrapure water (pH = 5.5 at 25 °C) and ultrapure water that was adjusted to higher pH using NaOH. Surface pressure-area isotherms were obtained on Langmuir film balances (Nima Technology Ltd., Conventry, U.K.) at room temperature with a compression speed of 5 cm^2/min (equivalent to between 3 to 7 $Å^2$/molecule • minutes depending on spreading solution concentration). Two different Langmuir film balances were used, one with dimensions of 5 cm by 35 cm

and one with dimensions of 7 cm by 15 cm for Brewster angle microscopy and ellipsometry measurements. Surface pressure measurements were made using a filter paper Wilhelmy plate (Whatman No. 1 paper). Monolayers were given 10 minutes for film relaxation prior to compression, unless stated otherwise. Monolayers were transferred at a constant surface pressure onto mica (physisorbed) or gold (chemisorbed) on the upstroke using the Langmuir-Blodgett (LB) technique with a dipping speed of 1 mm/min. All transfer ratios were always close to 1 for the mica deposition.

Brewster Angle Microscopy (BAM). Brewster angle microscopy was carried out with an I-Elli2000 imaging ellipsometer (Nanofilm Technologies GmbH, Göttingen, Germany) equipped with a 50 mW Nd:YAG laser (λ = 532 nm). All experiments were performed using a 20× magnification with a lateral resolution of 1 μm. BAM experiments were performed at an incident angle of 53.15° (Brewster angle of water) and a laser output of 50% (analyzer, compensator and polarizer were all set to 0).

Ellipsometry. Ellipsometric measurements at the air−water interface were carried out at an incident angle of 50.00° and a laser output of 100%, with the compensator set to 20.00°. The reported measurements are an average of 10 measurements each taken at a different location on the same film and is consistent for multiple samples. The ellipsometric isotherm is reported in terms of $\delta\Delta$, which is independent of the optical model. $\delta\Delta$ is defined as the difference between the ellipsometric angle Δ of the film on the subphase and the subphase alone ($\delta\Delta=\Delta film-\Delta subphase$). The reference, 0, is pure subphase before the film is spread. The measurements were taken at constant surface pressure. Ellipsometric measurements of films deposited onto gold were carried out at an angle of 65.00° and laser output of 1%, with the compensator set to 45.00°. The optical properties (n and k) of each gold substrate were determined using ellipsometry prior to deposition. The refractive index of the monolayer was set at 1.45[59]. Each set of deposition conditions was performed in triplicate, with 5 measurements per deposition at different locations.

Atomic Force Microscopy (AFM). A Nanoscope IIIa (Digital Instruments, Santa Barbara, CA) was used to capture AFM images in air at room temperature using tapping mode at a scan rate of 1 Hz using etched silicon cantilevers frequency of ~300 kHz, a nominal spring constant of 20-80 N/m and tip radius of < 10 nm. An oscillation operating at amplitude of 175 mV and medium damping (~25%) were

employed for these measurements. All AFM images are for films deposited onto mica unless otherwise indicated.

Grazing Incidence X-Ray Diffraction (GIXD). The GIXD experiments were performed at beamline 15-ID-C ChemMatCARS at the Advanced Photon Source (APS) in Argonne National Laboratory with the following parameters: X-ray beam wavelength of 1.239 Å, incidence angle of 0.09061°, horizontal size of 20 mm, and vertical size of 120 mm, leading to a beam footprint of 20 mm by 7.6 cm. The detector used was the two-dimensional Swiss Light source PILATUS 100K set to single-photon counting mode. Two sets of slits, one placed in front of the detector and the other placed 280.0 mm from the sample, were used to minimize intense low-angle scattering. Experiments were performed at the air/water interface of a 340 cm^2 Langmuir trough, where the monolayer was spread and then compressed at rates of 2 and 5 cm^2/min (equivalent to 0.5 and 1.3 $Å^2$/molecule min respectively) using a mobile barrier. The measured GIXD data was plotted as contour plots of the intensity as a function of both the horizontal (Q_{xy}) and the vertical (Q_z) scattering vector components. The lattice spacing d_{hk} was obtained from the in-plane diffraction data as $d_{hk}=2\pi/q_{xy}^{hk}$, where the Miller indices h and k were used to index the Bragg peaks needed to calculate the unit cell parameters for the in-plane lattice[111,139]. Raw data was extracted and patched using software developed by Wei Bu, beamline scientist at ChemMatCARS. The Bragg rods and peaks were fitted with Gaussian and Lorentzian function, respectively, using Origin lab graphing and analysis software.

4.4. Results and discussion

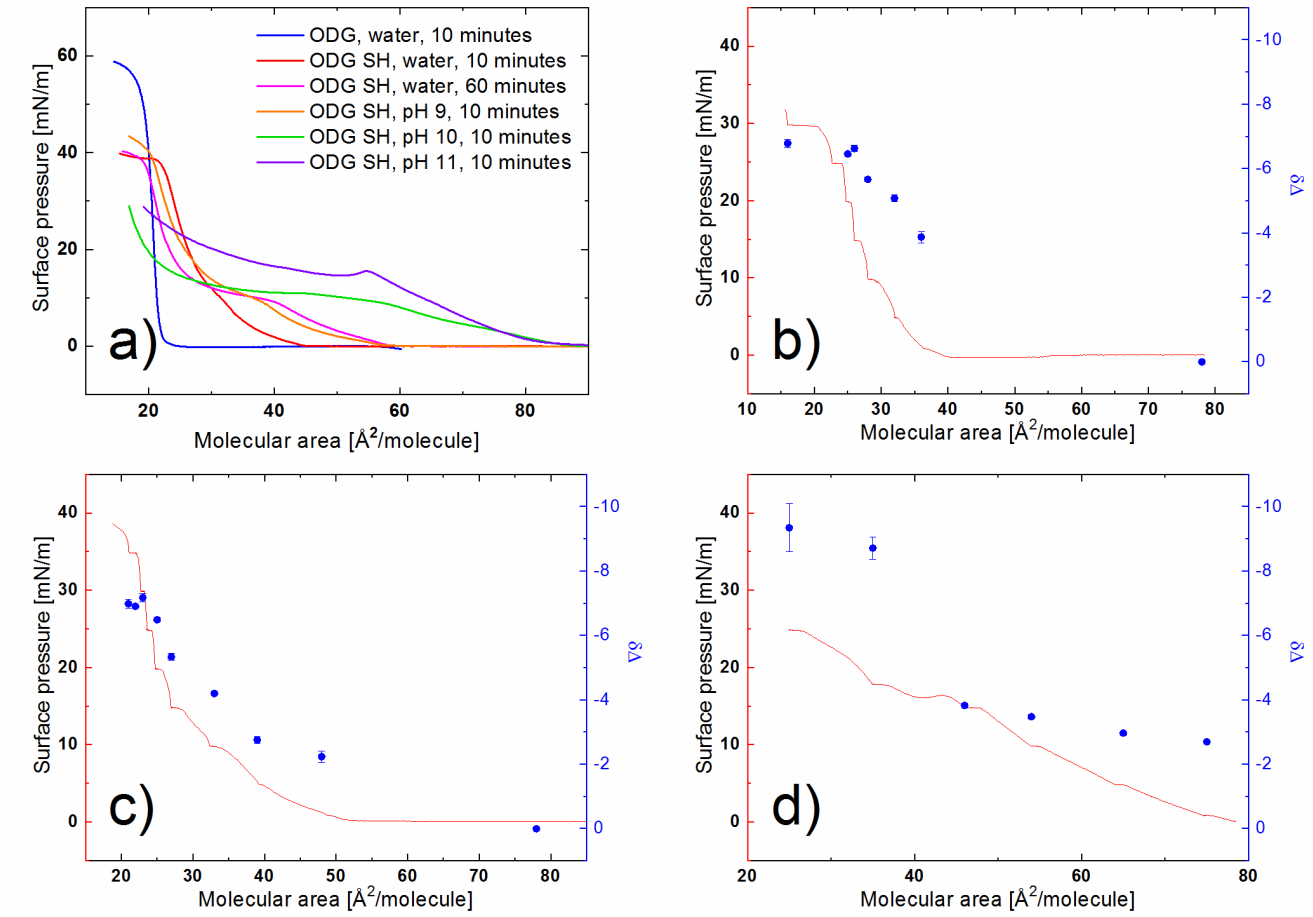

Figure 4-2 a) Isotherm of ODG SH on various subphase conditions with different relaxation times (indicated). Ellipsometric measurements at the air-water interface (blue points) along with isotherms in red, for b) ODG SH on water 10 min relaxation time, c) ODG SH on water, 60 min d) ODG SH on pH 11 subphase with 10 min relaxation time.

Isotherms for ODG SH under various pH conditions are shown in Figure 4-2a. On an ultrapure water subphase (pH 5.5, red line), with a standard relaxation time of 10 minutes prior to compression, ODG SH exhibits a critical area of 45 Å^2/molecule that is significantly larger than the critical area of 26 Å^2/molecule obtained for the non-thiolated (methyl-terminated) octadecylgallate (ODG, blue line). The large increase in molecular area is much greater than what might be expected simply due to the substitution of the methyl with a thiol, which are of similar sizes. A possible explanation for the large increase in critical area is that the molecule adopts a bola conformation[175] wherein the chain bends over

such that the thiol acts as a secondary headgroup (sometimes referred to as U-shaped). However, this conformation would be expected to have an even larger molecular area. For example, Lahann et al.[167] used computational methods to estimate the areas required to generate a bent conformation of mercaptohexadecanoic acid self-assembled monolayers. They found that 0.65 nm^2 generated an optimal balance between the area requirements for bending and maximizing hydrophobic interactions between the chains. Given the critical area lies between the proposed areas for bent chains of similar lengths and the extended chain of ODG, this may indicate the co-existence of both the bola and extended conformations. However, phase co-existence should not be thermodynamically favorable over a broad range of surface pressures for a single component system. The isotherms appear to converge in area at high compression states, prior to collapse of the ω-thiolated surfactant suggesting a compression-induced transformation from a bola to an extended conformation.

To probe the possibility of the coexistence of, and transformation between, kinetically and thermodynamically favoured phases, the monolayer was left to relax for 60 minutes prior to compression (pink line, figure 4-2a). This leads to an even greater critical area of 60 $Å^2$/molecule, almost triple that of the methyl-terminated surfactant. This would suggest that immediately upon spreading, the molecule initially adopts an extended formation, with the thiol oriented towards the air, but that this organization is only metastable, with a conversion to a bent, bola conformation, i.e. with both functional groups contacting the water, occurring over time. Additionally, after the longer relaxation period, the isotherm clearly exhibits a phase transition plateau around surface pressure ~10 mN/m. Such a plateau is usually associated with a first-order phase change in the monolayer[176]. Beyond this plateau, the area approaches the molecular areas obtained upon compression 10 minutes after spreading and the areas of the methyl-terminated surfactant, suggesting that compression of the film forces a return to an extended conformation as these areas are too small for the bola conformation. Upon closer examination of the isotherms with only 10 minutes relaxation time, a small kink in the isotherm can be discerned at 10 mN/m. The ODG SH monolayers all collapse at a lower surface pressures, around 40 mN/m, compared to the collapse pressure of approximately 55 mN/m for the methylated version, regardless of relaxation time. This is most likely due to the increase solubility brought about by the addition of the ω- hydrophilic thiol group[177].

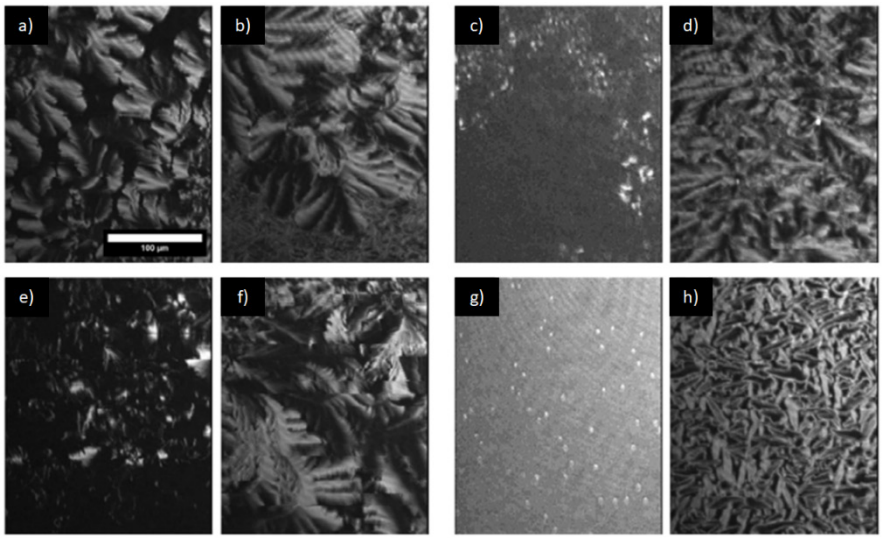

Figure 4-3 BAM images of ODG SH at below (left) and above (right) the plateau: a-b) water, 10 minutes relaxation time, 5 and 20 mN/m c-d) water, 60 minutes relaxation time, 5 and 25 mN/m e-f) pH 9, 10 minutes relaxation time, 1 and 12 mN/m g-h) pH 10, 10 minutes relaxation time, 8 and 11 mN/m. Note that the contrast was enhanced for c) and g).

BAM imaging was used to further elucidate the nature of the plateau. Representative images of ODG SH on a water subphase with either a 10 minutes or 60 minutes relaxation time at surface pressures above and below the plateau pressure are shown in Figure 4-3 a) and b). For the film with a short relaxation time, large domains with a mosaic texture (Figure 4-3a) are observed at both low and high surface pressures, attributed to a condensed phase formed by extended chains. Increasing the relaxation time (Figure 4-3b) lead to a surface bereft of mosaic domains at low surface pressure (5 mN/m). There is evidence of small bright domains which are not sufficiently large to observe the internal anisotropy, if present. Compressing the film into the plateau, leads to the recovery of the mosaic texture. Assuming the mosaic texture to be associated with the extended form, this provides further evidence that an extended-to-bola transformation takes place over time at high molecular areas but the reverse bola-to-extended transformation can be induced with compression via a first order phase transition. Such a bent-to-extended transition has been reported in the literature for the similar length 1,18-octadecanedicarboxylic acid[178] and longer bola amphiphiles[175].

Such a phase transition should be evident from monolayer thickness changes over the course of the isotherm which can be evaluated using ellipsometry. These measurements do not directly measure the

thickness of the monolayer but rather measure the change in ellipsometric angles which can be correlated to relative changes in optical properties including optical thickness[179]. The ellipsometric isotherms are presented in figures 4-2b and c and show that the monolayer with minimal relaxation time exhibits a large initial increase in the ellipsometric angle Δ (which is directly correlated to the thickness, assuming Ψ to be constant) once the critical area is reached, after which further compression yields only a modest increase in δΔ. It is important to note that the laser footprint is much larger than the domains at the air-water interface, thus the δΔ represents an average over the surface. A phase coexistence of condensed phase domains dispersed within a thinner matrix (gas or liquid-expanded phase) will lead to a film thickness that is not representative of the domain thickness, especially at low surface pressures and the modest increase in δΔ may reflect a reduction of the proportion of gas phase present at the surface instead of, or in addition to, a film thickness increase.

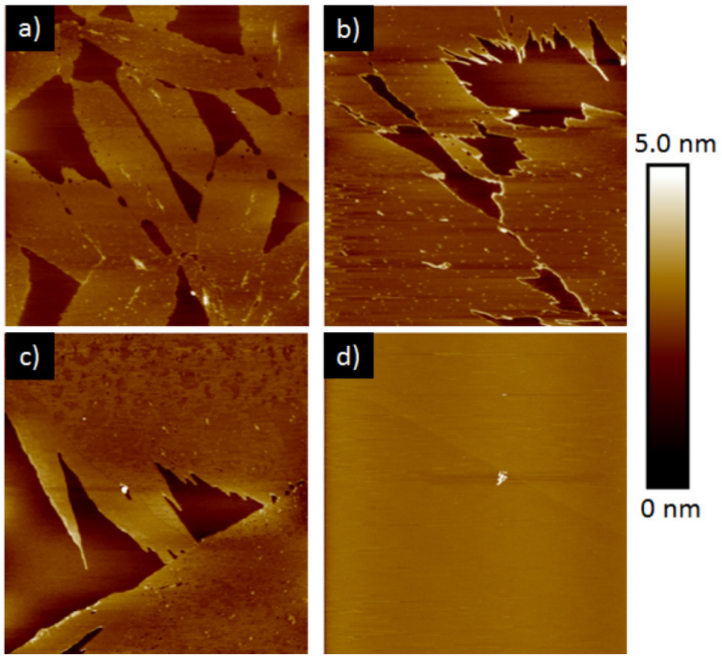

Figure 4-4 AFM images of ODG SH deposited onto mica at 5 mN/m with variations in subphase, relaxation time and image size: a) Water, 10 min, 5 µm, b) Water, 60 min, 5 µm, c) pH 9, 10 min, 5 µm, d) pH 9, 60 min, 20 µm.

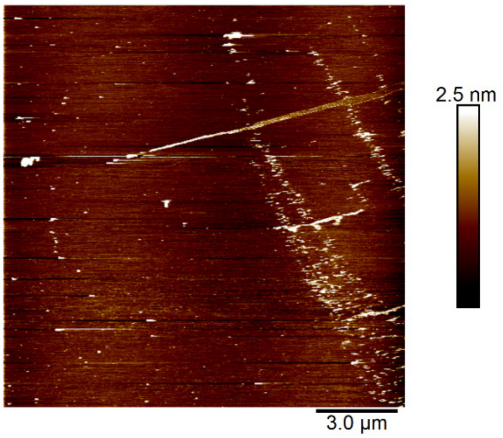

Figure 4-5 AFM image of ODG SH deposited onto mica from an ultrapure water subphase at a surface pressure of 20 mN/m after 10 minutes relaxation time.

AFM imaging of a LB film deposited on mica at 5 mN/m from a water subphase (Figure 4-4a) confirms a co-existence of condensed phase domains within a matrix which is 0.94 ± 0.18 nm lower in height. Deposition of this monolayer at higher surface pressure (20 mN/m, figure 4-5) shows a uniform surface corresponding to a full coalescence of the condensed phase domains and exclusion of any residual gas or liquid phase. Referring to the ellipsometric isotherm, by 20 mN/m the thickness of the film no longer increases significantly, supporting the conclusion that the increase in Δ observed results from exclusion of the thinner phase. In contrast, the ellipsometric measurements for the film with the longer, 60 minutes, relaxation time (Figure 4-2c) shows a more modest initial δΔ and a gradual increase in δΔ with compression. At higher surface pressures similar values of δΔ are reached with both monolayers,

Table 4-1Alkyl chain unit cell parameters derived from GIXD for ODG SH at room temperature on various subphase, where a, b, γ are the unit cell dimensions based on rectangular nomenclature, t is the tilt angle relative to normal, Ψ is the tilt direction relative to the unit cell and approximate thickness is the thickness estimated from the tilt angle and length of full extended surfactant.

Water						
Pressure (mN/m)	a (Å)	b (Å)	γ (°)	t (°)	Ψ	Approximate thickness (nm)
1	7.60	6.35	90	39	NN	2.4
20	7.58	6.37	90	39	NN	2.4
pH 10 subphase						
5	7.58	6.37	90	39	NN	2.4
15	8.31	4.84	90	15	NN	3.0

indicating that the final thickness achieved is the same regardless of relaxation time, consistent with an extended conformation at high surface pressures. AFM deposition for the latter film at low surface pressures (below the plateau) also shows a co-existence of condensed phase domains (Figure 4-4b) but the domain edges are more frayed and less rounded, consistent with the proposal that edge molecules convert to bola form (the surrounding matrix).

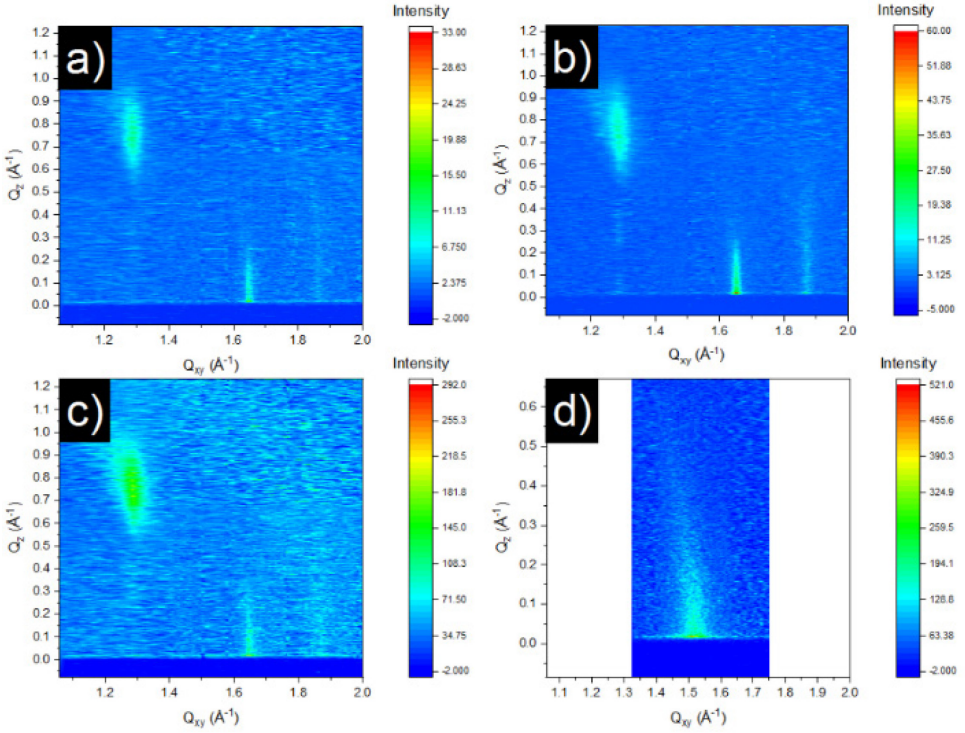

Figure 4-6 GIXD contour plots of the diffracted X-ray intensity as a function of the in-plane (Qxy) and out-of-plane (Qz) vector components for ODG SH: a) water, 1 mN/m, b) water, 20 mN/m, c) pH 10, 5 mN/m, d) pH 10, 15 mN/m.

GIXD provides information about the lateral structure of the condensed phase formed. A GIXD contour plot of the diffracted intensity as a function of the in-plane (Q_{xy}) and out-of-plane (Q_z) components of the scattering vector for ODG SH on water is show in Figure 4-6a with the corresponding unit cell parameters in Table 4.1. The peak positions (Appendix Table 2) and hence unit cell are identical within experimental error to those reported previously for the methyl-terminated ODG surfactant[172]. We note in particular the presence of a peak at Q_{xy} of 1.86 Å^{-1} that we previously attributed to a supermolecular

lattice unit cell due to headgroup ordering. This not only confirms that the condensed phase observed by BAM and AFM corresponds to the extended conformation, additionally the presence of the ω-thiol has no impact on the organisation of the surfactants when they are extended. This highlights the strength of the non-covalent interactions between the headgroups which dominates the organization leading to a supermolecular lattice in addition to an alkyl chain lattice wherein even the addition of the ω-thiol does not disrupt this organization.

Deposition of the thiol was achieved both using self-assembly and LB deposition from the air-water interface. The self-assembled monolayers (SAMs) of ODG SH exhibit a post-wash thickness of 3.81 ± 0.16 nm as determined by ellipsometry. This is thicker than the length of the fully extended surfactant (3.1 nm), indicating partial multilayer formation. Visualization of the surface using imaging ellipsometry did not reveal any features (data not shown), therefore any form of multilayer must be homogeneously distributed across the sample, at least on the micron scale.

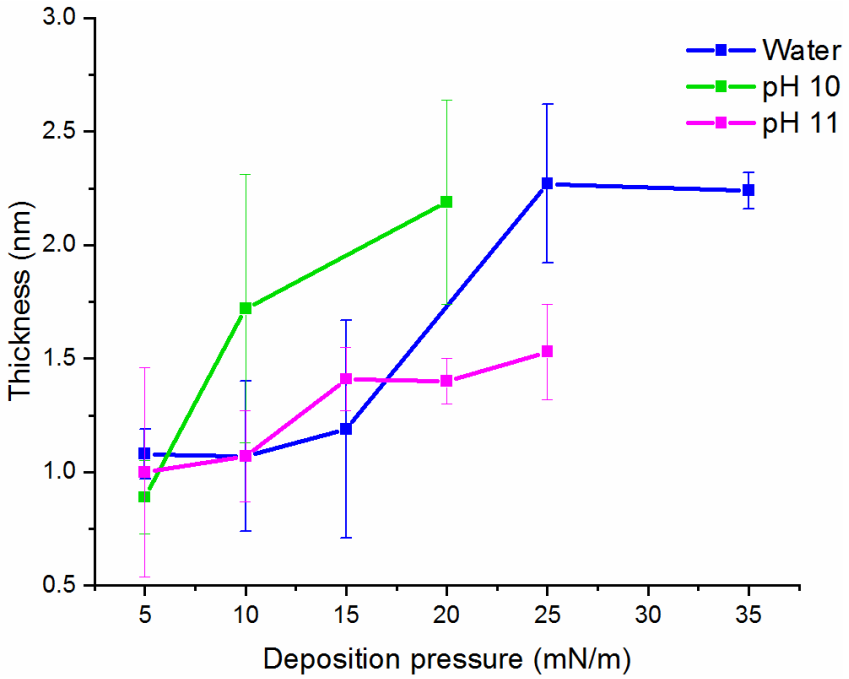

Figure 4-7 Deposition thicknesses obtained by ellipsometric measurement of ODG SH transferred onto gold substrate using LB deposition from the air-water interface as a function of deposition pressure for different pH subphases

The LB deposition onto gold from the air-water interface was carried out on the upstroke, with the gold surface being in an hydrophobic state[61]. The lack of observable meniscus and generation of a robust film that does not wash away, as is the case with methyl-terminated surfactant, support a chemisorption of the thiol to the gold even in an upstroke deposition. The average film thicknesses obtained for films deposited from the air-water interface are presented as a function of surface pressure in Figure 4-7 and Appendix Table 3. These films yield thicknesses that are significantly lower than those of the SAMs and are affected by both surface pressure and subphase pH (to be discussed later). Visualization of the LB deposited films by ellipsometry showed that they were free of large domains or other features that would indicate phase separation on the micron scale (data not shown). AFM imaging of deposited films on template stripped gold show no evidence of phase separation or poor coverage for either the SAMs or the LB films (see Figure 4-8). This may be due to the roughness of the bare sample masking any variation due to the monolayer (the roughness of the substrate is on the same order of magnitude as the monolayer).

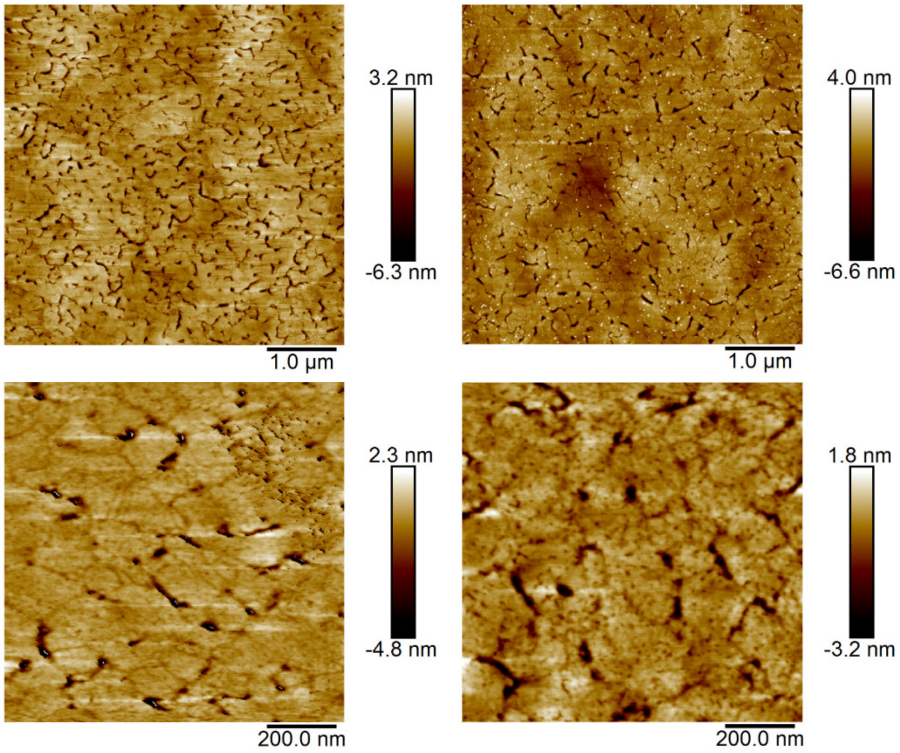

Figure 4-8 AFM images of a) bare template-stripped gold (TSG), b) SAM of ODG SH assembled on TSG, c) LB transfer of ODG SH from an ultrapure water supbase onto TSG at pressure of 25 mN/m before an ethanol wash, d) LB transfer of ODG SH on a water supbase onto TSG at pressure of 25 mN/m after an ethanol wash.

The surface of the LB film post-wash shows the appearance of multiple small holes with depths of around

1 nm (this depth measurement is likely tip-limited due to their small lateral size). These holes most likely derive from areas where the thiol failed to chemisorb to the surface and were subsequently removed during the wash process, which correlates with the decrease in thickness due to washing (see Appendix Table 3 for pre- and post-wash thicknesses). Transfer ratios were not recorded since the two sides of the substrate have different properties (hydrophobic gold and hydrophilic glass). In comparison, deposition of the physisorbing methyl-terminated ODG, yields a film with non-zero thickness that is completely removed through washing, confirming that the thiolated ODG SH is more strongly attached, likely chemisorbed, to the surface.

Deposition from a water subphase as a function of surface pressure shows two deposition regimes, either side of the isotherm kink, the surface pressure at which the bola form surfactants are forced upward due to surface pressure. Thus at 15 mN/m, the larger standard deviation is a consequence of depositing within the plateau region where the films appear to feature a mix of both bola and extended forms. The increase in thickness at surface pressures of 15 mN/m and above would then derive from variation in the proportion of these two forms since it was shown by GIXD that the organisation of the condensed phase, and therefore its thickness, is constant during the compression. Thus, the increase can be attributed to the exclusion of any remaining bola form still present at the air-water interface. Once all of the bola form is fully converted to extended form, the thickness stabilizes.

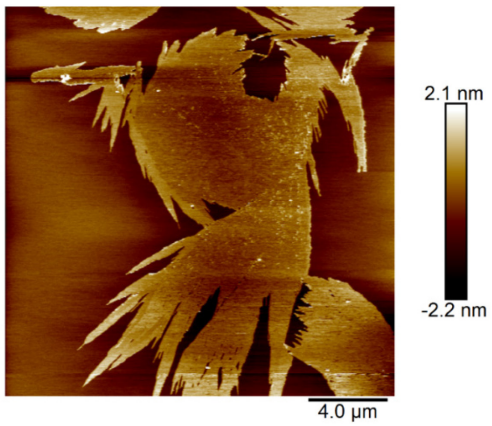

Figure 4-9 AFM image of ODG SH deposited onto mica from a pH 9 subphase at a surface pressure of 5 mN/m after 10 minutes relaxation time.

In our previous work, ODG rigid organisation imposed by strong headgroup interactions could be disrupted by increasing the subphase pH, attributed to deprotonation of two of the headgroup hydroxyls[172].

Similarly, modifying the subphase pH may alter either or both the molecular conformations or the kinetics of conformational changes. The isotherm of ODG SH on a pH 9 subphase (10^{-5} M NaOH) is shown in Figure 4-2a. At this pH and with 10 minutes relaxation time, the isotherm shows similar behaviour to that observed on water with the longer relaxation time, namely the shift to higher molecular areas and the appearance of a plateau in the isotherm at approximately 10 mN/m. BAM images (Figure 4-3c) confirm the similarity in the morphological features of these two films with small domains below the plateau (as well as some anisotropic regions) and complete coverage of the mosaic texture (anisotropic) film above the plateau. Similarly, AFM shows frayed domains (Figure 4-4c, and Figure 4-9) as seen for longer relaxation time on a water subphase. We have previously shown that increasing the pH of the subphase with ODG leads to smaller domains, most likely due to inter-domain electrostatic repulsion[172], even when the organisation at the molecular level within the domains is unperturbed. For ODG SH, the increase in pH increases the rate of conversion from an extended to a bola conformation, as seen by the increased critical area of the film, see Figure 4-10. Assuming that this transition is initiated at domain boundaries (likely leading to the frayed domain edges) where the surfactants have sufficient space and conformational freedom to bend over, then the increased rate of conversion correlates with a higher proportion of perimeter molecules that occurs with smaller domains. Combining an increase in pH and a longer relaxation time yields a greater increase in molecular area (Figure 4-10), demonstrating that the system is not yet at equilibrium. Under these conditions, BAM (Figure 4-11) and AFM (Figure 4-4 and 4-12) images

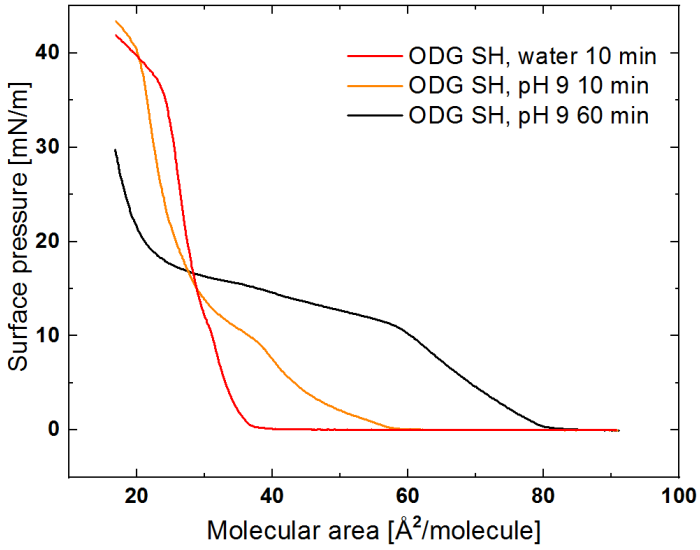

Figure 4-10 Surface pressure-molecular area isotherms of ODG SH as a function of subphase pH and relaxation time.

reveal a different morphology: below the plateau no features are seen, most likely indicating that the

system is fully in the bola conformation, which cannot coalesce into discreet domains. With the onset of the plateau, small condensed phase domains, attributed to the extended conformation, appear. This indicates that although the pH impacts the rate of conversion, the fundamental organisation of the system is unchanged and the bent-to-extended transition can still be induced with compression of the film.

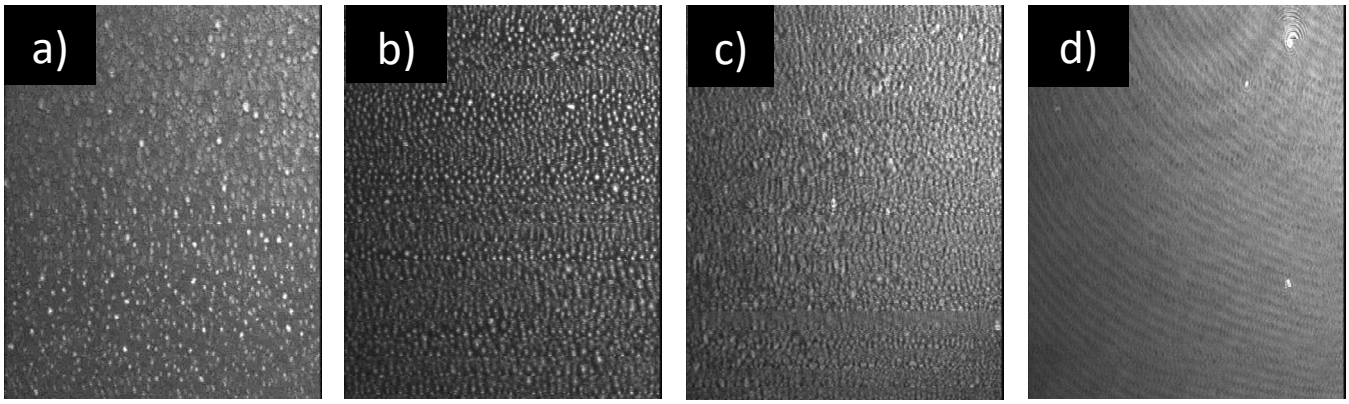

Figure 4-12 BAM images of ODG SH on a pH 9 subphase with 60 minutes relaxation at surface pressures of a) 10 mN/m, b) 12 mN/m, c) 15 mN/m, d) 22 mN/m.

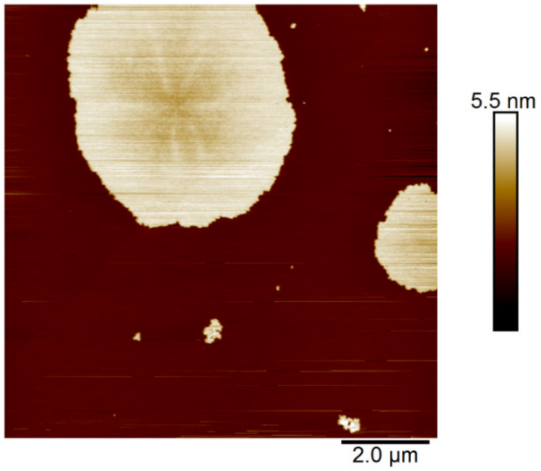

Figure 4-11 AFM image of ODG SH deposited onto mica from a pH 9 subphase at a surface pressure of 12 mN/m after 60 minutes relaxation time.

These effects are accentuated with increasing pH. At pH 10, shifts to higher molecular areas are observed (Figure 4-2a green), confirming a greater proportion of molecules with the bent, bola conformation or, in other words, a greater rate of conversion between the initial phase of extended conformation and the bent conformation phase formed upon relaxation at the surface. BAM (Figure 4-3d) and AFM (Figure 4-13a) imaging show the presence of some well-dispersed, small, condensed phase domains (1.5 to 1.7 nm above the background) below the plateau. This height difference between the two phases is larger than was obtained at lower pH (for which the height difference was approximately 0.95 nm). It is not known whether the greater height difference is because the condensed phase domains are thicker or the bola form matrix thinner, however, as will be shown below, the GIXD indicates that the tilt angle of the condensed domains present up to the plateau remains the same, indicating that the bola phase must be thinner which may be due to charge repulsion between deprotonated headgroups. It is thought, based on our previous work, that the gallate begins to undergo a second deprotonation at this pH.

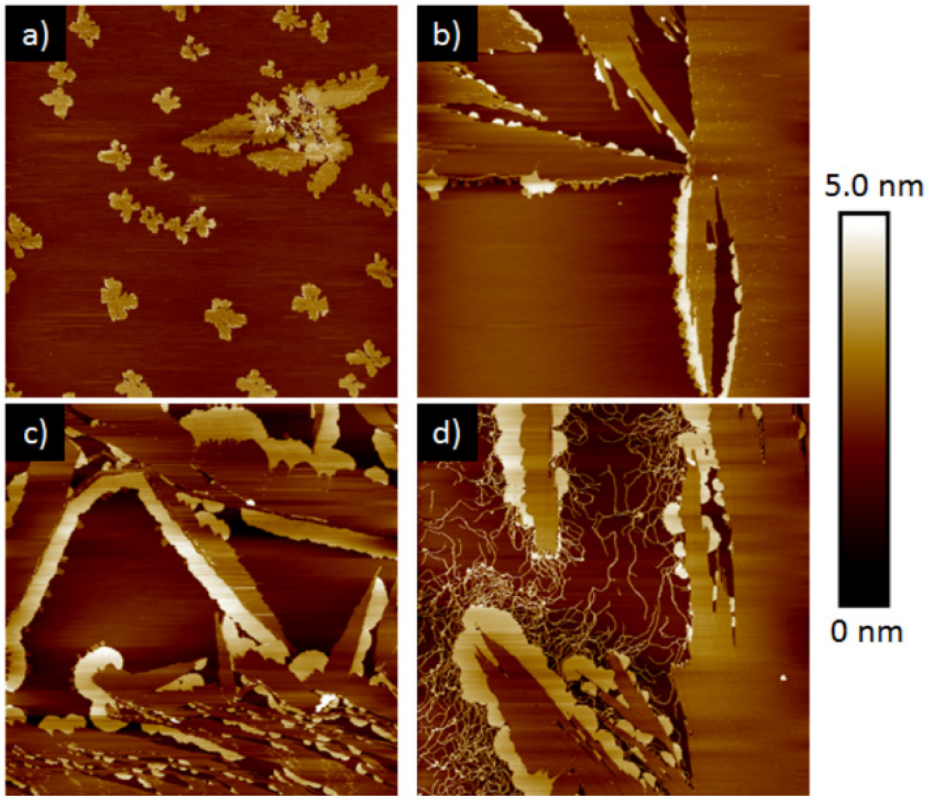

Figure 4-13 AFM measurement of ODG SH deposited onto mica from a pH 10 subphase at surface pressures of a) 5 mN/m, 25 µm, b) 10 mN/m, 25 µm, c) 14 mN/m, 15 µm, d) 16 mN/m, 15 µm.

However, the thiol must additionally be taken into account for which a pKa of approximately 10.5 has been reported[180].

BAM shows the growth of irregularly shaped domains at the beginning of the plateau (Figure 4-3d and 4.14). As the domains grow, the internal anisotropy becomes apparent with the brightness of the domain being a function of its orientation relative to the incoming polarized light. Many of the domains feature a dark interior with a brighter perimeter; notably these domains are oriented in the same direction (i.e. the long axis of the domain is horizontal with respect to the image, see highlighted domains in figure 4-14) while the brighter features are oriented vertically with respect to the image. AFM imaging was used

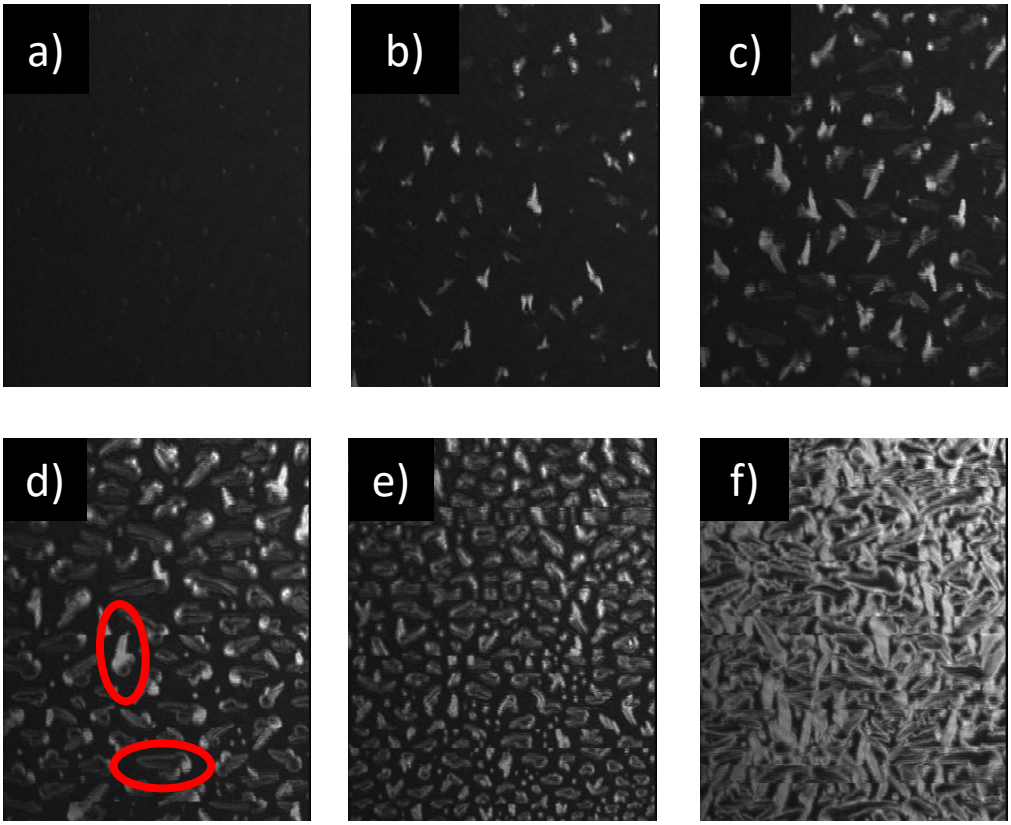

Figure 4-14 BAM images of ODG SH on a pH 10 subphase at surface pressures of a) 7mN/m, b) 8 mN/m, c) 9 mN/m, d) 10 mN/m , e) 11 mN/m, f) 12 mN/m. The ellipses in d) highlight two domains that differ in brightness due to their orientation.

to determine if the bright perimeter material is different from the dark interior or if this is simply a manifestation of the anisotropy. These images reveal a very unusual morphology (Figure 4-13 b-d and Appendix figure 3) with three phases with distinct heights. At the start of the plateau (Figure 4-13b), we

again observe the large, frayed-edge domains that are approximately 1.75 ± 0.14 nm higher than the surrounding matrix in height. Additionally, small bright regions are observed at the domain boundaries, which are 3.12 ± 0.14 nm above the background matrix. Initially, these appear as rounded nodules decorating the domain boundary (Figure 4-13b). As the surface pressure increases, these nodules coalesce to generate a more continuous band of material outlining the condensed domain. The lateral thickness of the band is reasonably consistent between domains and does not appear to grow beyond 1-2 μm from the domain edge. As the film emerges from the plateau, filaments appear to form extending from the continuous band of higher material. There is a higher density of these filaments near the edges of the band of higher material but they can extend throughout the background matrix (figure 4-13d) and the filaments are the same height as the continuous band, namely 3.12 nm above the matrix. Notably, in figure 4-13d (Appendix Figure 3 for a magnified view) the small round domains of the same material appear to nucleate at the junctions of filaments which may grow to form the larger domains of this materials observed in figure 4-13d and Appendix Figure 3. Notably, this morphology appears to be extremely sensitive to deposition conditions, i.e. the intermediate stages are not always observed and films comprising only the round domains surrounded by a high density of filaments (to be discussed later), in the absence of the intermediate height condensed domains, can also be observed.

GIXD measurements were performed below and above the plateau region (1, 5 and 15 mN/m, Figure 4-6 and Appendix Table 2). At the lowest surface pressure, no discernible diffraction pattern was observed, this was attributed to a low density of any residual extended form, condensed phase material. By 5 mN/m, the organization is identical to that observed for both the thiol- and methyl-terminated surfactants on a water subphase, for which the tilt angle was invariant with compression. At the plateau, a transition takes place with a step change to less tilted structure (tilt angle of 15° from the normal, versus 39° from the normal at lower surface pressure and on water at all surface pressures). Additionally, the high Q_{xy} peak attributed to headgroup ordering is no longer present. If both the frayed domains and the band of higher material surrounding them are assumed to be liquid crystalline, either two diffraction patterns should be observed or one, if they have identical organizations. However, if the band of higher material were to be fully organized, one would expect to see bending of the peaks along the Debye-Scherrer line to reflect the three-dimensional nature of the structures[181,182]. Given that neither of these are

the case, two assumptions can be made: the plateau corresponds to the transition between the two tilted structures, and concurrently the taller material is formed and is amorphous.

Using this information, we can attempt to identify the various features seen by AFM. The background matrix is most likely the surfactant in bola form, which is not in a condensed phase and therefore does not generate a diffraction pattern. Just below the plateau, domains appear which correspond to the more tilted phase (figures 4-13a and 4-6c). At the phase transition, the frayed edge domains are generated which must correspond to the lower tilt angle phase seen by GIXD in agreement with the increased height difference observed with AFM. The film thickness has been estimated from the molecular length (3.1 nm full extended) and the tilt angle in Table 4.1. For the phase with a 15° tilt angle, the maximum thickness would be 3.0 nm. Given these domains are only 1.8 nm above the background, it can be assumed that the background matrix comprises the bent bola conformation and precludes that this is simply uncovered mica. The bola phase must therefore have a thickness of approximately 1.2 nm. This is in reasonable agreement with a bent chain conformation, assuming a tight turn, which can be achieved

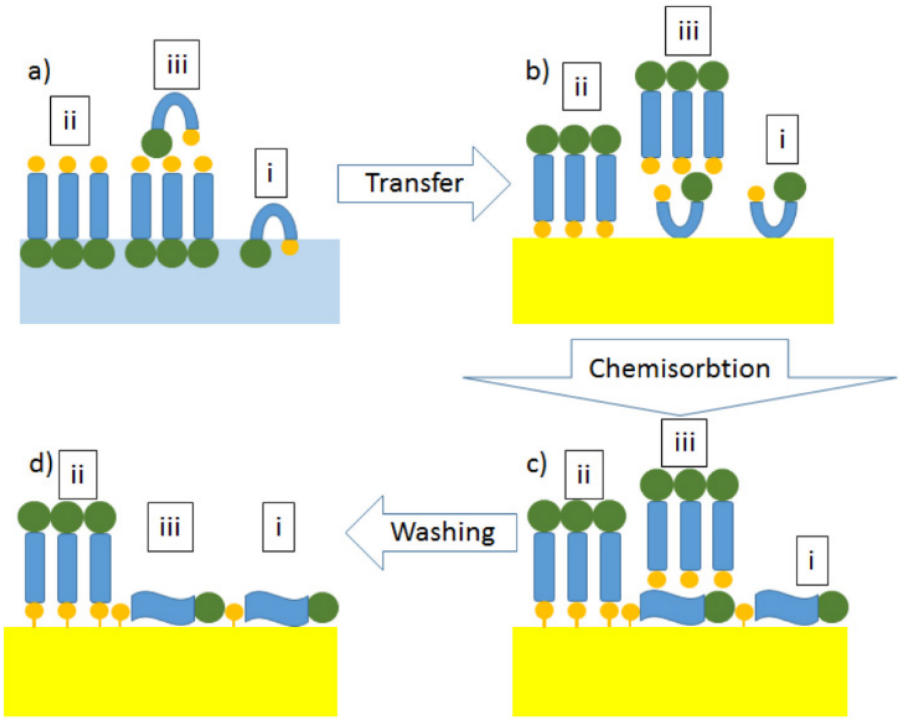

Figure 4-15 Schematic representation of the various phases formed by ODG SH on a pH 10 subphase at high surface pressure: a) at the air-water interface, b) after LB transfer onto gold, c) after chemisorption, d) after washing.

even with only 6 carbons involved in the turn[183]. The highest phase (3.1 nm above the bola phase) is too

high to be a single monolayer. The height difference between the higher material and the domains in which they are in contact is 1.4 nm (tallest phase to intermediate phase), which is in reasonable agreement with another bola layer. It is therefore propose that the material in this highest phase is not a traditional multilayer but rather a combination of an underlying condensed phase with the molecules in extended form upon which sits an additional layer in bola form (Figure 4-15a, iii). This would allow the surfactant to maximize the interactions between polar moieties, the thiol at the end of the condensed phase and both the thiol and phenol of the bola phase, leaving the bola chain exposed. Compressing bola surfactant monolayers often results in multilayer formation[184–186], but to our knowledge there are no reports of a multilayer combining the layers of extended molecules with layers of bent conformation molecules. This difference may derive from the molecular structure: prior studies used symmetrical bola amphiphiles whereas here we report on an asymmetric ω-thiolated phenolic bola surfactant.

We previously showed with the methyl-terminated octadecylgallate that high pH can modify the film organization[172]. However, although the methyl and thiol-terminated surfactant condensed phases show identical organizations and tilt angles on water, the impact of headgroup deprotonation leads to very different tilt angles at high pH as well as a difference in the pH required for deprotonation. Assuming the phenolic headgroup retains a similar pKa, which is not unreasonable given the similarity in phase behaviour, this would indicate that once the headgroup organization is disrupted (loss of the high Q_{xy} peak), the ω-thiol has a much more significant impact on the phase behaviour. The change in the packing and tilt angle is likely driven by maximizing thiol-thiol non-covalent interactions.

Since the filaments observed using AFM for films deposited from a pH 10 subphase (figure 4-13d) are the same height as the nodules formed (the highest phase) we assume that they correspond to the same phase. This is supported by the observance of only a single diffraction pattern by GIXD. Given the nodules appear at lower surface pressures (the beginning of the plateau) while the filaments appear only at the end of the plateau, this might suggest that the formation of the multilayer can occur via different routes. They initially form only at the edges of the condensed phase domains indicating that the phase boundary catalyzes and nucleates the formation of the multilayer phase. Once the frayed domain perimeter is mostly covered, a new nucleation mechanism results in the long filaments. Linear nanostriped multilayers formed by bolaamphiles were reported by Chen et al.[185], although in this case the multilayered bola amphiphile was proposed to be in an upturned bent conformation, i.e. the orientation was driven by

hydrophobic interactions. They based their conclusion on a prior report in which traditional, single-headgroup surfactants could form linear multilayers along defect lines[187]. In both of these reports, these defects at which multilayer formation occurred attributed to the mismatch of the area requirements of the polar groups and the hydrophobic chains. In our case, this mismatch may be amplified by the strong headgroup interactions and non-equivalent headgroups that may be driving molecular alignment.

The methyl-terminated surfactant has a tendency to form a condensed phase with highly directional growth at high pH[172] which has been attributed to strongly oriented headgroup interactions. Such interactions can also dominate with the bolaform surfactant, for example a symmetric phenolic bola surfactant by Liu et al.[188] showed strong tendency to form filamentous domains but only when the alkyl chain number was odd, otherwise 3D nanostructures were formed. This was attributed to the presence of strong directional interactions between both the phenol headgroups and the amide connections to the chains which then limited the conformation freedom of the alkyl chain. The difference in chain lengths (odd versus even) led to changes in the dipolar interactions between the amides resulting in the different either parallel or anti-parallel arrangements (filaments or 3D structures).

Deposition of the films onto gold substrates from pH 10 subphase shows an earlier, i.e. at lower surface pressure, increase in deposition thickness compared to water (figure 4-7). This large increase coincides with the appearance of the thicker (frayed edge) domains observed on mica (figure 4-13d), which GIXD confirmed were thicker than the condensed phase formed on water (table 4.1). However, further compression does not yield as large an increase in the thickness of the deposited film (compare 20 mN/m to 10 mN/m). At these higher surface pressures, the film comprises three phases, postulated to be i) fluid phase comprising bola form, ii) condensed phase comprising straight form and iii) a multilayer comprising a bola-form atop the condensed phase (see figure 4-15a). Depending on the surface pressure and phases present, not all of the thiols will contact the hydrophobic gold during the LB deposition process in which the outward facing groups (air-side) make initial contact with the gold. For the simple bola phase (phase i, figure 4-15), although the chain makes initial contact with the gold, the flexibility afforded in this phase enables subsequent rearrangement such that many of the thiols can chemisorb. For the extended-form condensed phase domains (phase ii, figure 4-15), the thiol is exposed air-side and therefore easily chemisorbs. For the multilayered phase (phase iii, figure 4-15), again the bola can re-organize to

contact the gold, however much of the extended phase upon which the bola resided is either not transferred or blocked from chemisorbing to the gold surface, allowing it to be washed away (figure 4-15c and d)).

Spreading the monolayer on a pH 11 subphase does not cause further increase in the critical area (Figure 4-2a) but induces a slight increase in the plateau pressure. As was observed on the pH 10 subphase, no features are visible by BAM before the plateau (with the exception of a 2D foam structure directly after spreading, supplemental Figure 4-16). Again visible domain formation begins with the plateau, with a different morphology. Initially, small, bright domains are observed within a non-homogeneous background. By 20 mN/m these domains appear to coalesce with only a few residual holes visible (figure 4-16). AFM images taken of films deposited below the plateau are mostly flat with the occasional small domain that would be at the limit of the resolution of BAM. The domains have a height between 1.5 and 2.5 nm (supplemental Figure 4-17a) above the continuous phase and display significant roughness. It may be that these domains are remnants of the extended form of the surfactant which has not converted into bolaform prior to compression. GIXD of the film at 5 mN/m shows no discernible diffraction peaks indicating that the continuous phase is likely the bolaform surfactant and that there are not sufficient condensed phase domains present within the beam footprint to generate a diffraction signal. Above the plateau, AFM shows the co-existence of filaments and small round domains that are 2.7 ± 0.2 nm above the continuous bolaform phase, i.e. at no stage are only circular domains or filaments observed (supplemental Figure 4-17b). The circular domains are at the limit of the resolution of BAM. At this pH

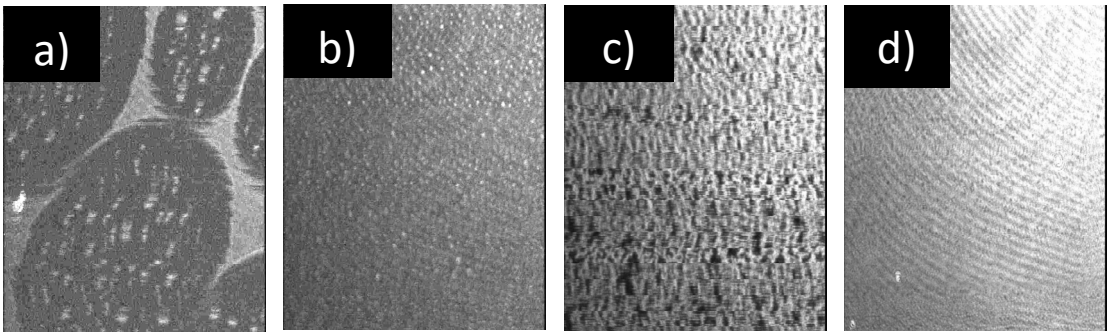

Figure 4-16 BAM images of ODG SH on a pH 11 subphase at surface pressures of a) 0 mN/m, immediately after spreading, b) 15 mN/m, c) 14 mN/m (past the local maxima), d) 20 mN/m.

and surface pressures above the plateau, there is no evidence of the intermediate height phase that was observed at pH 10. Despite this GIXD confirms the presence of the low tilt angle phase (Figure 4-18),

similar to what is seen at pH 10. However the signal is weak, such that the exact position of the out-of-plane peak cannot be fit with confidence. Evidence that the phase is still tilted (i.e. that there is a second peak which resides at Q_z>0 Å^{-1}) derives from the peak widths. The in-plane peak is at a very similar position (Q_{xy} 1.48 Å^{-1} at pH 11 compared to 1.51 Å^{-1} for pH 10), but fitted as a single peak this would yield a FWHM in Q_z that is far too high for a C18 alkyl chain (see Appendix Table 2 for GIXD peak fits). The weak GIXD peaks are most likely due to a smaller area surface coverage by this phase. Given the lack of evidence of an intermediate height (condensed) phase in the AFM images at these surface pressures, it can only be concluded that this low tilt condensed phase must reside underneath the small domains and filaments. Ellipsometric measurements at the air-water interface show a significant step change in δΔ at the plateau region which also reaches greater (more negative) δΔ values (Figure 4-2d).This is consistent with a transition from a predominantly bola phase with very few condensed phase domains to a multilayered phase. Notably, the surface homogeneity in this phase separated system was low, resulting in large errors on the measurements at high surface pressures. Our previous work[172] showed that the second pKa of the headgroup is approximately 11 in the condensed phase. At subphase pH of 11 or higher, a similar low tilt condensed phase was formed depending on the time allowed for film relaxation. In the case of ODG SH, it appears that increasing the charge on the phenolic headgroup limits the ability

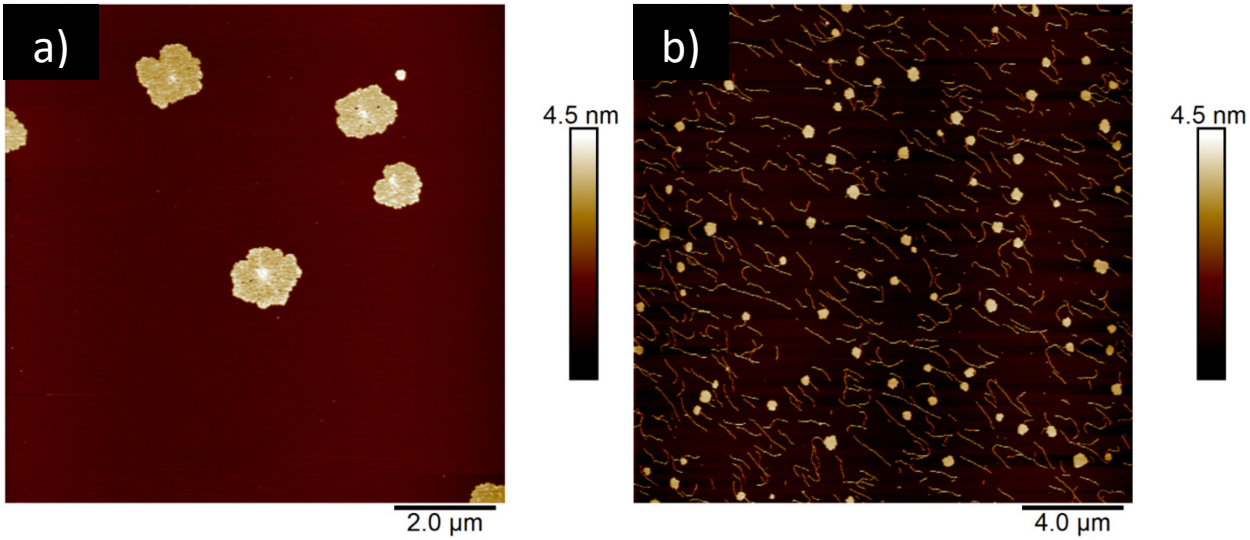

Figure 4-17 AFM image of ODG SH deposited onto mica from a pH 11 subphase at surface pressures of 5 and 15 mN/m after 10 minutes relaxation time.

to form the condensed phase unless a multilayer can be formed concurrently. This may be due to the

additional stabilizing non-covalent interactions between the thiol and the phenol when a multilayer is formed.

In contrast to the ellipsometry at the air-water interface, deposition of the film from a pH 11 subphase onto gold indicates a lower film thickness than observed at lower pH and the lack of a significant step change in thickness at the plateau. At low surface pressures, the film showed no GIXD peaks and is therefore assumed to have only one dominant phase, a fluid bola form phase, present, which explains the similarity in thickness between all of the films deposited at 5 mN/m. Upon compression, only the multilayered phase and the bola phase are observed (phases i and iii in figure 4-15). As described earlier, phase iii does not deposit well and in the absence of an extended from condensed phase, only the bola-phase deposits to any great extent (i.e., the overlying phase is easily washed away). This results in a small, continuous change in thickness for the deposited films at pH 11, attributed simply to compression of the bent bola form chains. Even upon higher compression, the thickness never reaches that expected for a condensed phase.

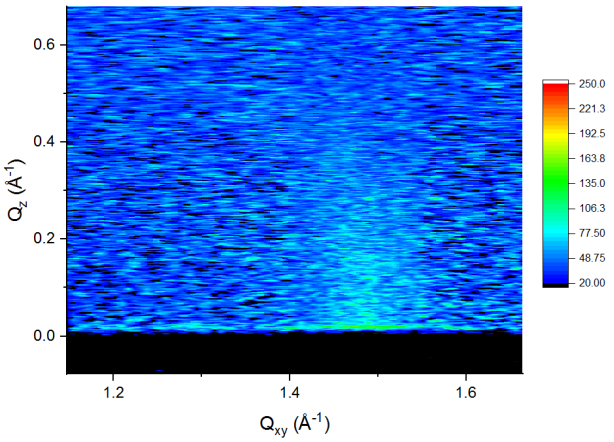

Figure 4-18 Contour plot of X-ray intensity as a function of the in-plane (Qxy) and out-of-plane (Qz) vector components of ODG SH on a pH 11 subphase at a surface pressure of 15 mN/m.

4.5. Conclusions

The formation of highly organized chemisorbed monolayers of long chain thiols from solution self-assembly is now well established yet there are relatively few examples of deposition of long-chain thiols from an air-water interface as means to control lateral spacing and film organization[87]. Ihalainen and Peltonen[89] demonstrated that ω-methyldisulfide-terminated phospholipids, in which one of the two

alkyl chains terminates with a disulfide moiety, can be deposited with the disulphide exposed for subsequent metal deposition, however this was for a disulfide rather than thiol. In this work we demonstrate that for single chain, condensed phase forming surfactants, the addition of an ω-thiol does not impact the structure of the condensed phase on water. It does however, impact the overall phase behaviour, wherein the ω-thiol acts as a second headgroup. Initially, a condensed phase forms which comprises an identical organization to the methyl-terminated surfactant, i.e. the extended conformation of the surfactant. This is however kinetically unstable: relaxation over an extended period of time prior to compression allows a significant proportion to convert to a bola conformation, wherein both the phenol and thiol are tethered to the water. This is reversible with film compression, where the reduction in available surface area will force the surfactants back to an extended conformation, yielding a first order phase transition (plateau). The kinetics of the transition from extended to bola can be increased by increasing the subphase pH to 9. This is most likely due to the increased electrostatic repulsion between the deprotonated phenols for which the bolaform organisation, where the phenols are further apart, is more favorable. Understanding the behavior of such molecules is essential to be able to use the LB deposition as a means to afford control over film organization at the air-solid interface.

Most reports of bola amphiphiles at the air-water interface involve symmetrical molecules. Herein we report on an asymmetrical molecule such that one headgroup provides the means to tether to the solid surface and will confer functionality to the deposited film. At high pH (pH 10 and above), this results in the co-existence of multiple phases including a multilayer phase. Importantly, unlike systems in which the ‘collapse’ of the film generates amorphous material and/or irregular multilayers, this asymmetrical bola amphiphile forms a regular, well-defined structure which is proposed to be a second bola conformation atop the extended form condensed phase. The evolution of this multilayer, in the forms of nodules decorating the edges of the condensed phase, circular domains and filaments within a bola matrix, was followed using AFM and GIXD.

Finally, we demonstrated that the monolayer films could be deposited by Langmuir-Blodgettry from the air-water interface, generating robust, chemisorbed films. The deposited film thickness, and hence organization, is dependent on the deposition conditions, i.e. both the surface pressure and subphase pH, and as such these could be employed to tailor the lateral spacing between the surfactants. This opens

the avenues for a new deposition approach by pre-assembling ω-thiolated surfactants at the air-water interface.

Chapter 5. Phenolic monolayers exhibit strong binding with copper and proline causing chain-independent re-organization of the headgroups

5.1. Abstract

Phenolic compounds such as tannins are known to bind strongly to proline-rich proteins and to chelate metals. Surfactants containing phenolic headgroups have the potential to mimic these properties in a self-assembled film. Yet, with headgroups that themselves exhibit strong intermolecular interactions, leading to highly organized structures, the impact of film phase, morphology and organization on the binding is important. We studied the binding of poly-L-proline as well as zinc and copper ions to a Langmuir monolayer formed from ω-thiolated, gallate surfactants with either shorter (C12) or longer (C18) chains. Both copper ions and poly-L-proline interact strongly with the monolayer, even at submicromolar (10^{-7} M) subphase concentration, while zinc ions were absent from the interface. Notably, the films formed are dominated by the headgroup-analyte interactions, regardless of the chain length, i.e. in the presence of the corresponding binding partner, the films properties of ODG SH and LDG SH appear to be converging in terms of isotherm, morphology and structure. Pre-organization of the film for subsequent deposition onto solid substrate will permit tailoring of the film for binding and therefore sensing applications.

5.2. Introduction

Tannins have a propensity to interact with metals and proteins[127], particularly proline rich protein[4]. These interactions are centered on the phenol moiety[9,189] which exhibits binding selectivity. For example, many poly-phenols selectivity bind copper over zinc ions[20,23] and proteins that have proline-rich regions have a stronger binding affinity with poly-phenols[9]. This binding selectivity could be exploited for biosensing, but this would require a convenient method to attach the phenol to the solid surface with control over the lateral organization; one approach would be to use well-established gold-thiol chemistry. Furthermore, if multiple proline residues were to bind simultaneously to multiple phenol moieties, unhindered by steric restrictions, this would create a far stronger affinity between polyphenol surface and the desired protein or peptide analyte. On the other hand, steric restrictions are a major consideration. It

is known that proline interacts via stacking interactions with the phenol moieties[9]. This emphasizes the necessity to pre-organise the phenols in order to fine tune the selectivity. One strategy would be to pre-organise the phenols in the presence of the analytes of interest at the air-water interface, such that the phenols adopt the optimal organisation, prior to deposition and subsequently removing the bound analytes. This is analogous to the approach used in molecular imprinting of polymers[72].

To this end, we have previously studied the air-water interface behavior of surfactants possessing a phenol moiety[172]. At this interface, phenols should possess enough conformational freedom to reorganise when presented with analytes with significant binding potential such that they adopt conformations to maximize binding to the selected analytes, either metal ions or proline-rich proteins. These films could be subsequently deposited onto gold-coated solid supports. For this deposition method, the impact of the ω-thiol on the organisation of phenolic surfactants and the ability to deposit such films, is important[190]. It was previously shown that monolayers of phenolic surfactants self-assembled onto gold have different interaction strengths with phosphate depending on the position of the hydroxyl groups on the aromatic ring[40]. If the lateral phenol-phenol intermolecular interactions reduced their ability to interact with other analytes of interest, namely phosphates, demonstrating the importance of controlling the lateral spacing of phenol moiety to modulate the interaction with analytes and neighboring phenols.

In this work, the interaction of phenolic surfactants with both metal ions and poly-L-proline

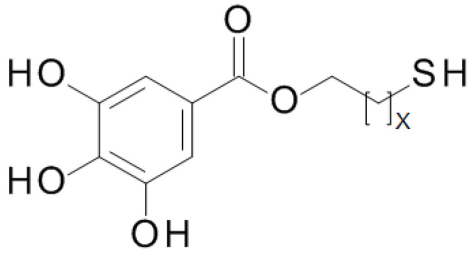

Figure 5-1 Structure of surfactants used, X=11: 12-sulfanyldodecyl 3,4,5-trihydroxybenzoate (ω-thiolated lauryl gallate, LDG SH), X=17: 18-sulfanyloctadecyl 3,4,5-trihydroxybenzoate (ω-thiolated octadecyl gallate, ODG SH).

peptides were investigated. Langmuir monolayers at the air-water interface were spread first on subphases containing dissolved chloride salts of either zinc or copper. The surfactant to metal ion molar ratios were kept constant at either 1:1 or 1:10 (surfactant:metal), assuming all metal would bind to the monolayer. Copper and zinc salts were selected because they are both divalent ions and known to have different binding affinities for phenols in solution, with copper ions showing stronger binding than zinc[23]. Poly-L-

proline is used as an analogue of proline-rich proteins and peptides which are often found in saliva[7] and are of interest as biomarkers[191].

In addition, to investigate the impact of the monolayer phase (either liquid expanded or condensed), two different ω-thiolated surfactants were studied with chain lengths of 12 and 18 carbons, namely 12-sulfanyldodecyl 3,4,5-trihydroxybenzoate (ω-thiolated lauryl gallate, LDG SH), and 18-sulfanyloctadecyl 3,4,5-trihydroxybenzoate (ω-thiolated octadecyl gallate, ODG SH) respectively (Figure 5-1). Where appropriate, the interactions with the corresponding octadecylgallate (ODG) are presented for comparison. Herein it is demonstrated that when the analyte is already present in the subphase when the monolayer is spread, the interaction with a strongly-bound analyte dominates the organization of the films rather than the phase naturally formed by the surfactant.

5.3. Experimental

Materials. 12-sulfanyldodecyl 3,4,5-trihydroxybenzoate (LDG SH) was synthesized as previously reported[192]. 18-mercaptooctadecyl 3,4,5-trihydroxy benzoate (ODG SH) was synthesized as previously reported[190]. Ultrapure water (resistivity of 18.2 MΩ/cm) was obtained from an EasyPure II LF system (Barnstead, Dubuque IA). The spreading solutions were prepared using chloroform (HPLC grade, trace of ethanol as preservative) from Fisher Scientific Company. Mica (grade V1) used in the AFM deposition was purchased from Ted Pella Inc. and freshly cleaved before each measurement. Poly-L-proline was purchased from Sigma Aldrich, it is composed of a mixture of polyproline peptides with molecular weights ranging from 1000 to 10 000. The dominant species was determined using mass spectrometry to be 25 prolines long (Pro_{25}) which was used to calculate the lipid:peptide ratio.

Isotherm measurements. Monolayers were spread from a chloroform spreading solution (1 to 1.5 mM) on two different types of subphases: ultrapure water (pH = 5.5 at 25 °C) and ultrapure water that was adjusted to higher pH using NaOH. Surface pressure-area isotherms were obtained on Langmuir film balances (Nima Technology Ltd., Conventry, U.K.) at room temperature with a compression speed of 5 cm^2/min (equivalent to between 3 to 7 $Å^2$/(molecule • minute) depending on spreading solution concentration). Two different Langmuir film balances were used, one with dimension of 5 cm by 35 cm and one with dimensions of 7 cm by 15 cm for Brewster Angle Microscopy. Surface pressure measurements were made using a filter paper Wilhelmy plate (Whatman No. 1 paper). Monolayers were

given 10 minutes for film relaxation unless stated otherwise. Monolayers were transferred at a constant pressure onto mica (for AFM) on the upstroke using the Langmuir-Blodgett technique with a dipping speed of 1 mm/min. All transfer ratios were always close to 1.

Brewster Angle Microscopy (BAM). Brewster Angle Microscopy was carried out with an I-Elli2000 imaging ellipsometer (Nanofilm Technologies GmbH, Göttingen, Germany) equipped with a 50 mW Nd:YAG laser (λ = 532 nm). All experiments were performed using a 20× magnification with a lateral resolution of 1 μm. BAM experiments were performed at an incident angle of 53.15° (Brewster angle of water) and a laser output of 50% (analyzer, compensator and polarizer were all set to 0).

Atomic Force Microscopy (AFM). A Nanoscope IIIa (Digital Instruments, Santa Barbara, CA) was used to capture AFM images in air at room temperature using tapping mode at a scan rate of 1 Hz using etched silicon cantilevers frequency of ~300 kHz, a nominal spring constant of 20-80 N/m and tip radius of <10nm. An oscillation operating at amplitude of 175 mV and medium damping (~25%) were employed for these measurements.

Grazing Incidence X-Ray Diffraction (GIXD). The GIXD experiments were performed at beamline 15-ID-C ChemMatCARS at the Advanced Photon Source (APS) in Argonne National Laboratory with the following parameters: X-ray beam wavelength of 1.239 Å, incidence angle of 0.09061°, horizontal size of 20 mm, and vertical size of 120mm, leading to a beam footprint of 20 mm by 7.6 cm. The detector used was the two-dimensional Swiss Light source PILATUS 100K set to single-photon counting mode. Two sets of slits, one placed in front of the detector and the other placed 280.0 mm from the sample, were used to minimize intense low-angle scattering. Experiments were performed at the air/water interface of a 340 cm^2 Langmuir trough, where the monolayer was spread and then compressed at rates of 2 and 5 cm^2/min (equivalent to 0.5 and 1.3 $Å^2$/molecule min • respectively) using a mobile barrier. The measured GIXD data is plotted as contour plots of the intensity as a function of both the horizontal (Qxy) and the vertical (Qz) scattering vector components. The lattice spacing d_{hk} was obtained from the in-plane diffraction data as $d_{hk}=2\pi/q_{xy}^{hk}$, where the Miller indices h and k were used to index the Bragg peaks needed to calculate the unit cell parameters for the in-plane lattice[111,139]. Raw data was extracted and patched using software developed by Wei Bu, beamline scientist at ChemMatCARS.

The Bragg rods and peaks were fitted with Gaussian and Lorentzian function, respectively, using Origin lab graphing and analysis software.

X-ray fluorescence near total reflection (XFNTR). The XFNTR experiments were performed at beamline 15-ID-C ChemMatCARS at the Advanced Photon Source (APS) in Argonne National Laboratory using the same trough and chamber for GIXD experiment. The beam energy was of 10 keV (1.239 Å), the incidence angle range used was of 0.0904° to 0.1695° with slits size of 0.04 mm and a Vertex-60EX detector set 10 mm above the surface. The data fitting was performed using software developed by Wei Bu, beamline scientist at ChemMatCARS using procedure described elsewhere[193].

5.4. Results and discussion

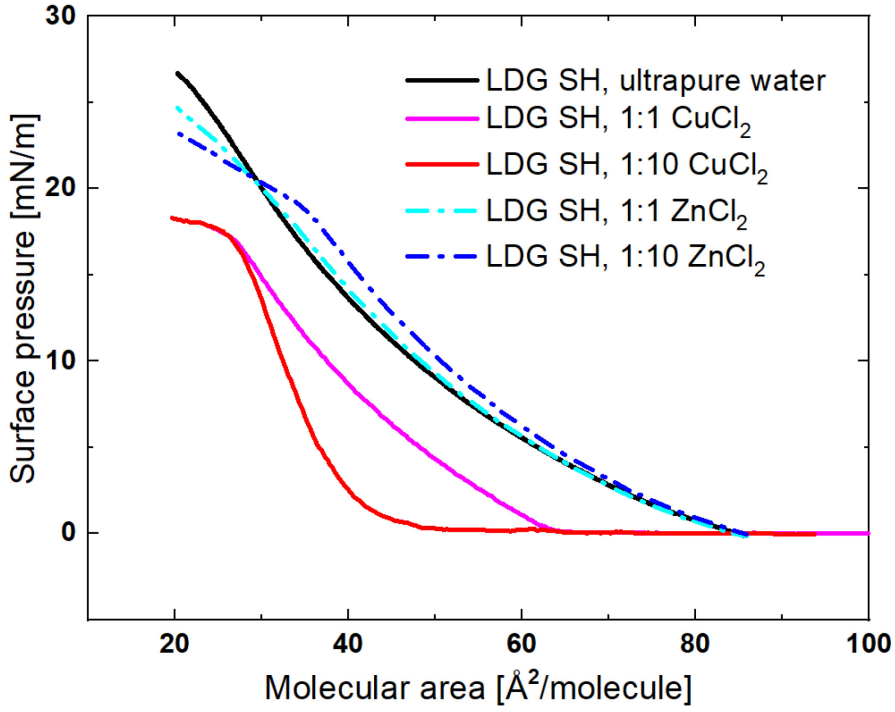

Figure 5-2 Surface pressure-molecular area isotherms of LDG SH as a function of lipid to metal ratio.

The surface pressure-area isotherms for ω-thiolated lauryl gallate on different subphases are shown in Figure 5-2. On a water subphase, LDG SH exhibits liquid expanded behavior at all surface pressures. Metal ions were introduced into the subphase such that either a 1:1 or 1:10 surfactant:metal ratio would result if all metal ions accumulated at the interface. The presence of zinc ions in the subphase

causes no significant changes in the isotherms (Figure 5-2), although the film is slightly more expanded at high surface pressures. In contrast, copper ions have drastic effects, with a large reduction in critical area, from 85 Å^2/molecule to 64 Å^2/molecule for the 1:1 ratio and 50 Å^2/molecule for the 1:10 ratio. This is also accompanied by a large decrease in collapse pressure, the cause of which will be discussed later. The copper ions appears to condense the monolayer which likely results from the metal ions bridging the phenols; this condensation is also reflected in the compressibility modulus which is significantly increased at a ratio of 1:10 LDG SH:copper ions (Figure 5-3). This in itself is not unusual as

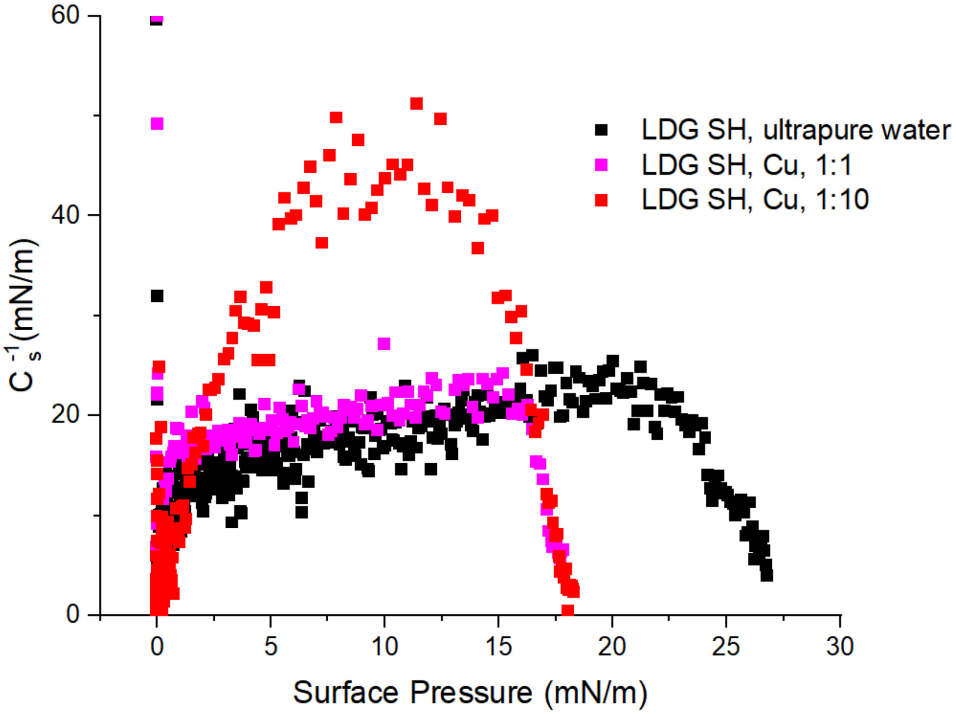

Figure 5-3 Compressibility modulus of LDG SH as a function of subphase lipid to metal ratio.

ions frequently have an ordering effect on films[194], but the difference between zinc and copper, both divalent ions, suggests a specific effect, especially given the low overall ion concentration (10^{-7} M).

While it is clear that there is a strong effect due to copper ions, it is possible that zinc ions are also bound but either has a limited effect on the isotherm or binds to a lesser extent. X-ray fluorescence at the air water interface was used to ascertain and quantify the presence of metal ions in the surface layer. Measurements were carried out at both ratio of 1:10 for copper ions and zinc ions but also for a subphase combining both copper and zinc ions, in a 1:10:10 ratio (lipid:copper:zinc), to confirm the preferential binding of the phenol to copper ions over zinc ions, see Table 5.1 (Appendix Figure 4 for raw data). The measurements were taken at 2 mN/m to avoid the presence of collapse material at the surface. As can be seen, copper ions have a very strong adsorption to the monolayer whereas zinc ions shows no measurable signal. This also hold true for the mixed system, which shows that the monolayer affinity for copper over

Table 5-1 Surface ion density as measured by XFNTR at a surface pressure of 2 mN/m, no signal was detectable for zinc ions in both conditions.

System, ratio and subphase concentration	Surface density (atom/Å^2)
LDG SH: Copper (1:10), 2.48e-06 mol/l	0.02295
LDG SH: Zinc (1:10), 1.66e-06 mol/l	No signal
Lauryl SH: Cu and Zn (1:10), Copper 2.48e-06 mol/l Zinc 2.42e-06 mol/L	0.02688 (Cu), no signal (Zn)

zinc ions is the reason for the vastly different isotherms rather than the two different ions binding differently to the phenol. The surface density of copper ions was determined to be 0.02295 atom/Å^{2,} equivalent to approximately 1 atom per 43 Å^2 or 1 atom of copper ions per surfactant present at the interface, when compared to the value of molecular area from the isotherm at 2 mN/m (40 Å^2/molecule). The depth of penetration of the evanescent wave is approximately 50 Å from the surface. Thus, the

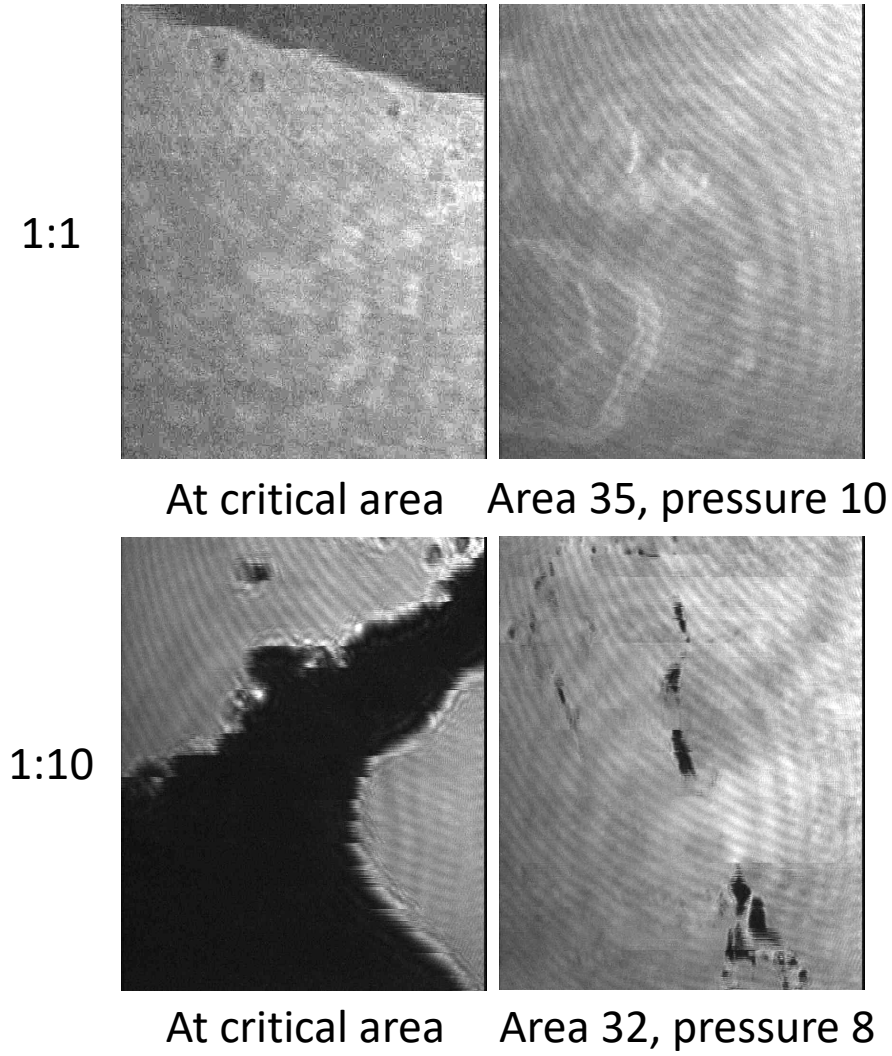

Figure 5-4 Brewster angle microscopy images of LDG SH on subphase containing copper ions at two different lipid:metal ratio. Image at critical area of 1:1 ratio contrast was enhanced.

technique cannot distinguish chelated copper ions from an underlying copper ions rich water layer, which could mean the number of ions directly associated with the phenol might be lower.

The shift of the isotherm towards lower molecular areas in the presence of copper ions, suggests the formation of a condensed phase. Brewster angle microscopy of LDG SH on either an ultrapure water

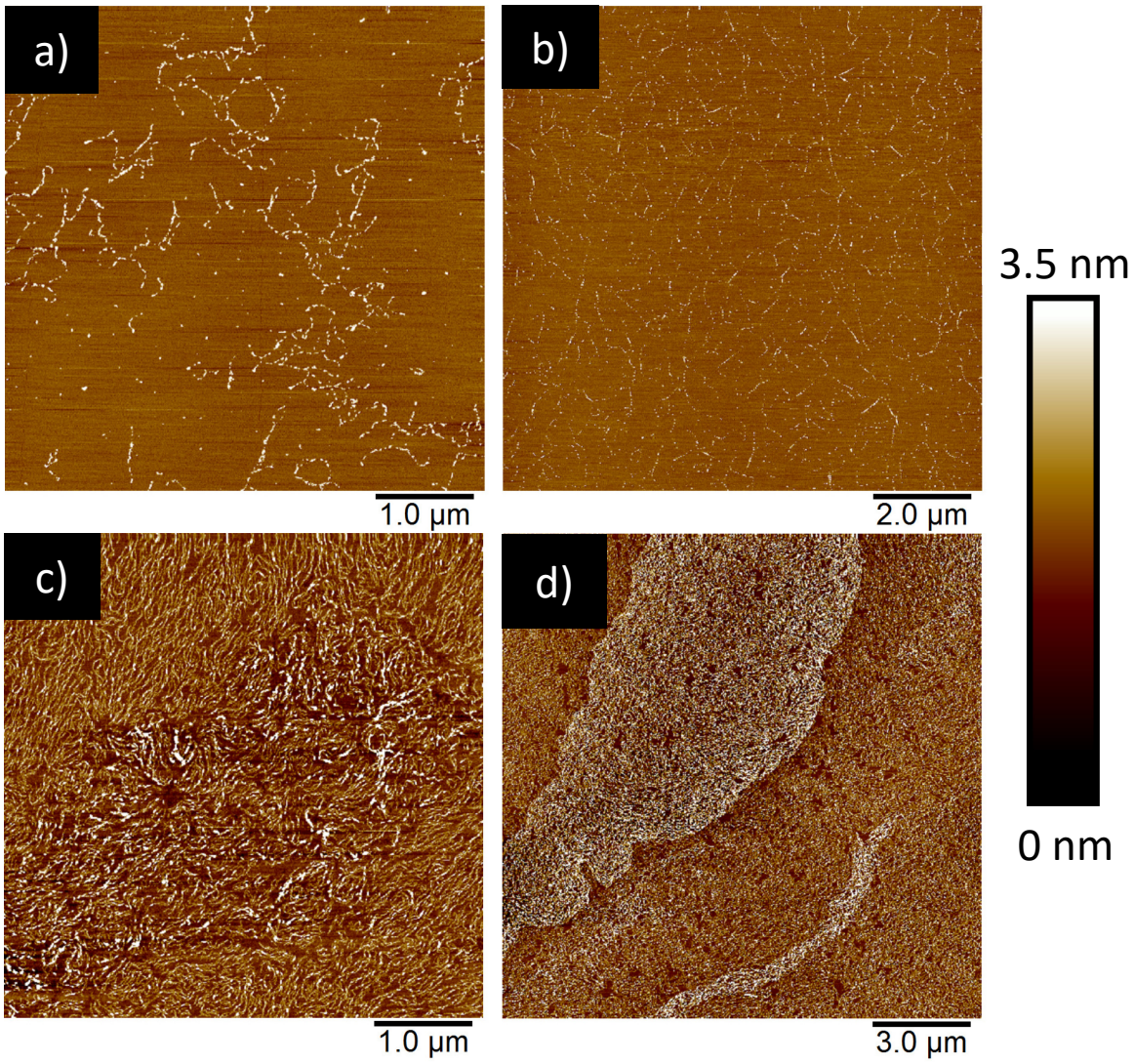

Figure 5-5 Atomic force microscopy images of LDG SH monolayers deposited by Langmuir-Blodgettry onto mica substrates at pressure of 5 mN/m. Lipid:metal ratio of 1:1 (a, b) and 1:10 (c, d)

or a zinc ions-containing subphases does not show any evidence of domain formation (data not shown), however domains are visible for LDG SH at both copper ions ratios (Figure 5-4). At the higher 1:10 ratio,

a greater proportion of the surface is covered by condensed phase domains and a stronger contrast of the domains with the background is observed. The domains are large plate-like domains, with no specific shape motif. These appear as soon as the surfactant is spread and compression only serves to force the domains into closer proximity (Appendix Figure 5a for image before compression). The increase in surface pressure coincides with the point at which most of the gaseous phase has been excluded and the domains begin to contact and coalesce. Residual gaseous phase can be observed even at high surface pressures, indicative of a rigid condensed phase.

AFM imaging of films deposited by Langmuir-Blodgettry reveal a more complex morphology when spread in presence of copper ions (zinc ions shown no changes compared to water, see Appendix Figure 5). Filaments are present at the interface in both 1:1 and 1:10 cases (Figure 5-5). In the 1:1 case, the filaments are around 1.66 ± 0.19 nm above the background. This can be correlated to the BAM images darker and lighter regions, likely corresponding to areas with low and high densities of these filaments, respectively. The situation is similar in the case of the 1:10 ratio, however with an overall much higher density of filaments and region where the filaments are much higher (brighter region) reaching upward of 5 nm. At this ratio, there are regions where the higher segments are ubiquitous, which may explain the presence of anisotropy in the domains seen by BAM, i.e. areas with high concentrations of higher filaments appear brighter. We have previously shown[190] for the longer-chain ODG SH, that the addition of the ω-thiol can allow the surfactant to behave as a bola surfactant, with both the phenol headgroup and the thiol being in contact with the water, but that upon compression the surfactant can undergo a conformational change such that if it behaves as a traditional surfactant. Here we propose a similar bola conformation is initially adopted upon spreading, which corresponds to the background matrix seen in the AFM images. Catechol and gallic acid are known to chelate metals such as copper ions in a bidentate manner and even in binary complexes[22,195,196], although in solid state, the latter generates an orientation that is not conducive to monolayer formation. If copper ions were to bridge multiple phenol headgroups, it must necessarily bring the surfactants closer together, and force the thiol from the water surface. The formation of a copper-bridged, extended-chain condensed phase (filaments) surrounded by a bola amphiphile liquid phase (dark areas) would correlate well with the height differences between the phases measured using AFM, which are less than a molecular length at full chain extension (2.3 nm).

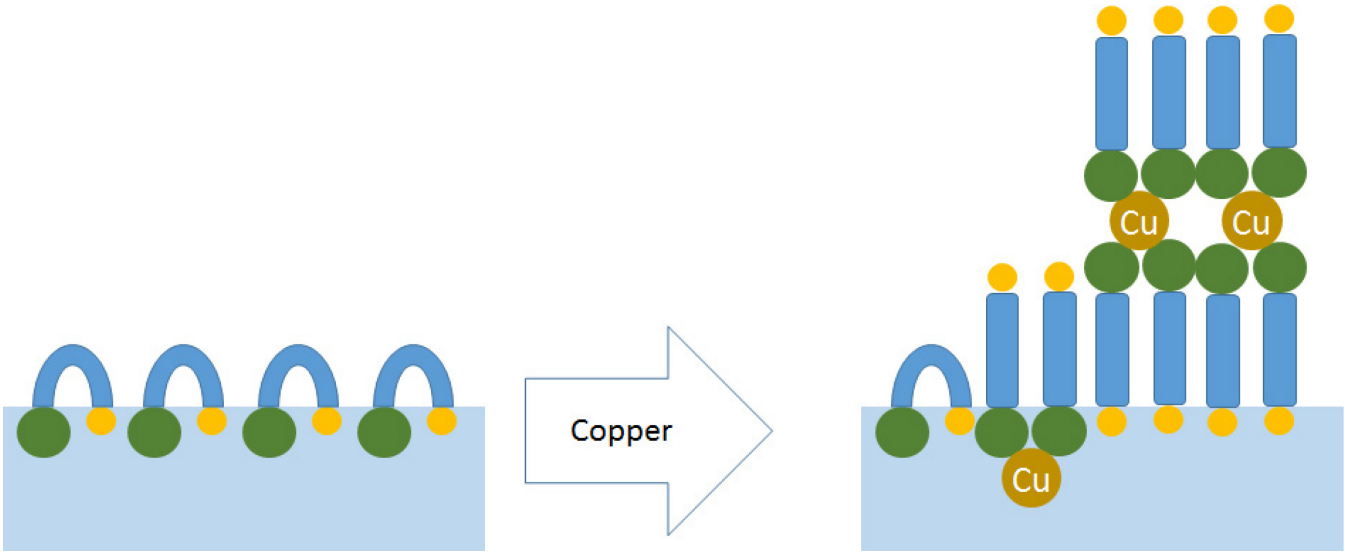

Figure 5-6 Schematic representation of LDG SH monolayer on ultrapure water (left) and a possible re-organization of the film on a subphase containing copper at a 1:10 lipid:metal ions ratio (right).

Given the height differences, the higher filament segments appear to be a form of bilayer or even multilayer, likely with the copper ion bridging the two layers and the thiol of the bottom layer connected to the water (see Figure 5-6). A similar organization was proposed for the collapse of arachidic acid in the presence of Ca^{2+} ions using MD simulations and confirmed by X-ray reflectivity[197]. Similarly a surfactant derived from urea[198] was shown to reorganize at the air-water interface such that the hydrophobic chain contacts the water and the hydrophilic headgroups are in the middle (vertically) of the monolayer film rather than submerged in the subphase. This is attributed to a strong, multipronged hydrogen-bonding network.

GIXD was used to probe the nature of the filamentous condensed phase. For a monolayer spread on a copper ions-containing subphase (1:10) no diffraction peaks were observed (data not shown, full scan range in Q_{xy}, was from 0.5 to 2.0 $Å^{-1}$). In addition, neither LDG SH on ultrapure water and, or, on a 1:10 zinc ions-containing subphase produced any discernible diffraction peaks. Two potential explanations for the apparently contradictory results for LDG SH associated with copper ions arise. In the first, the nature and size of the filaments leads to a very low correlation length such that only a broad, diffuse scattering would be expected. Such a reduction in condensed phase correlation length has been observed for the intercalation of iron within a dipalmitoylphosphatidylcholine (DPPC)[199] monolayer. In the second, the headgroups bind to the copper ions which forces the headgroups into a rigid network that

is not, or only, weakly ordered. Previous research[172] has shown that long chain phenolic surfactant, C18, are heavily titled (39° from the normal), this organization was heavily influenced by the phenol headgroup space requirement. If the addition of copper ions causes the system to adopt an similar organization, with the same tilt requirement, then the C12 chain might be too short to generate sufficient van der Waals interactions for chain condensation. A similar idea, namely the organization of the headgroups into a network wherein the chain spacing and length are insufficient for the formation of a condensed phase has been proposed by Giner-Casares *et al.*[200], although in their case the headgroup network was induced by the asymmetric nature of the surfactant and the large size of the headgroup.

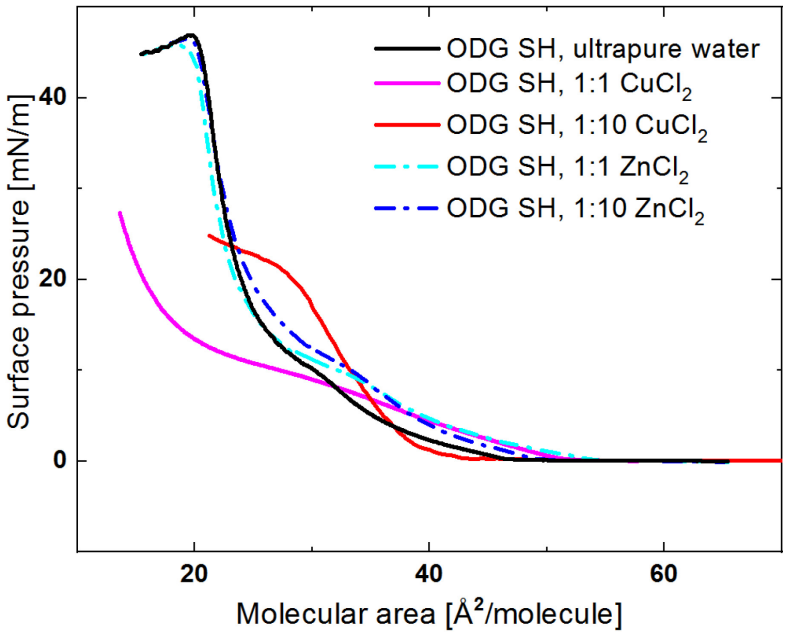

Figure 5-7 Surface pressure-molecular area isotherms of ODG-SH as a function of lipid to metal ratio.

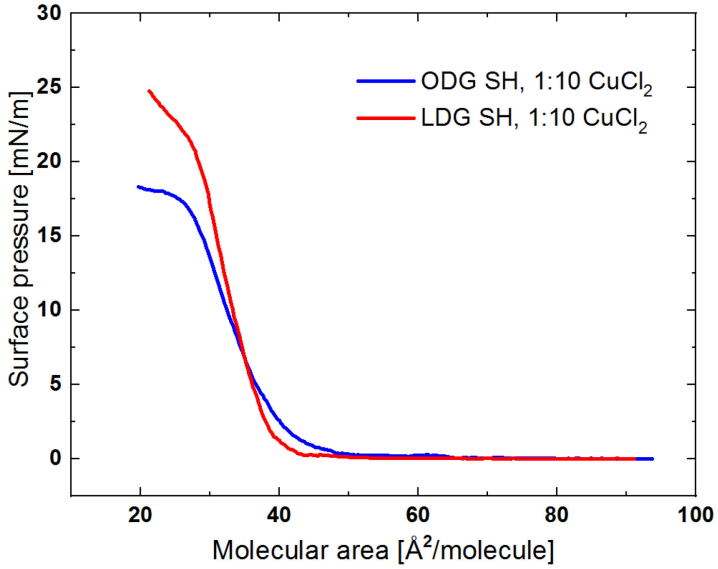

Figure 5-8 Surface pressure molecular area isotherms of ODG SH and LDG SH at 1:10 lipid:$CuCl^2$ ratio

While LDG SH shows almost no interaction with zinc ions, the situation is different when the phenolic lipid adopts a condensed phase due to a longer alkyl chain, as is the case with ODG SH (Figure 5-1). In this case, zinc ions does show modest effects on the isotherm, Figure 5-7, with a somewhat higher critical area and a more pronounced phase transition. Those effects are however very minor compared to the impact of copper ions. In that case, the molecular area increases rather than decreases, as was the case with LDG SH. The film behaviour on a copper ions subphase at the lower ratio (1:1) is similar to the film behavior on the zinc ions subphase, with a plateau around 10 mN/m and a small shift to higher molecular areas. Beyond the plateau, as the pressure continues to increase, the isotherms cross, and the molecular area shifts to much smaller areas than can be reached with ODG SH on ultrapure water. This is probably due to the formation of structures extended into the z-direction, as was observed for LDG-SH with the formation of bilayer filaments. In the case of the higher metal ratio (1:10), the critical area for the onset of pressure shifts to lower molecular areas, there is a loss of the phase transition plateau and the film collapses at much lower surface pressures. Notably the isotherm of ODG SH 1:10 copper ions and LDG SH 1:10 copper ions are very similar (Figure 5-2 and 6, see Figure 5-8 for an overlay of the two isotherms), having almost identical critical areas and similar collapse pressures, despite the two surfactants adopting different phases when spread on ultrapure water. This indicates that at sufficiently high concentrations, the intercalation of the copper ions with the phenol

headgroups dictates the molecular spacing, regardless of the chain length.

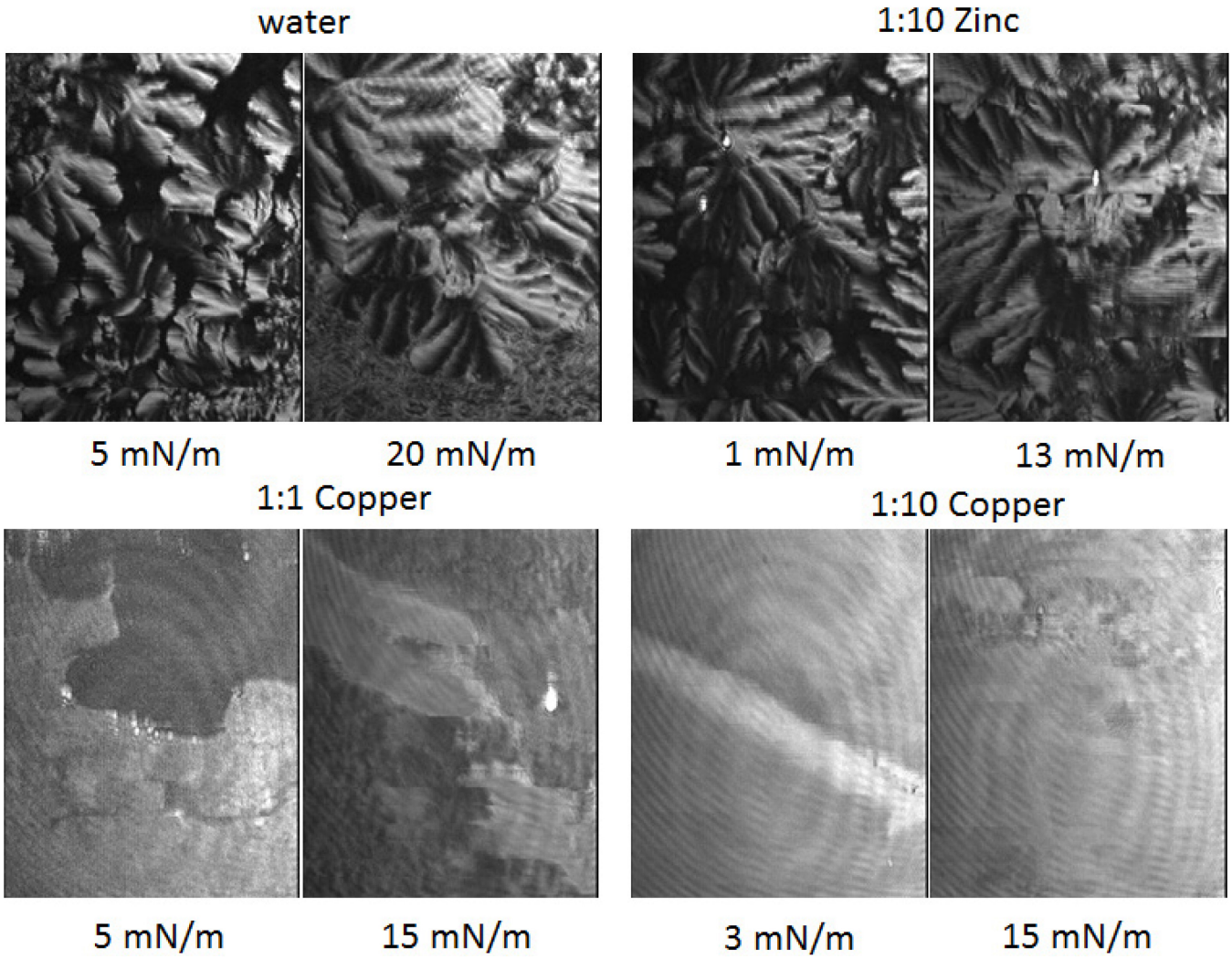

Figure 5-9 Brewster angle microscopy images of ODG SH on subphase of ultrapure water or containing metal with lipid:metal ratio given.

Brewster angle microscopy of the ODG SH on an ultrapure water subphase was previously published and showed a mosaic texture (Figure 5-9), wherein the texture is due to internal anisotropy of an otherwise relatively flat surface[190]. The addition of zinc ions at either the 1:1 or 1:10 ratio produced little difference compared to water (1:10 shown in Figure 5-9). The copper ions containing subphase, however, generates significant differences, both above and below the plateau, with significant inhomogeneity. AFM imaging again reveals highly inhomogeneous surfaces for both 1:1 and 1:10 copper

ions (Figure 5-10). At 1:1 these show remarkable similarity with LDG SH AFM, exhibiting filaments that have formed above the continuous phase which have highly regular width (50 ± 6.0 nm) and height (1.3 ± 0.16 nm taller than the background), attributed to bilayer structures. As with LDG SH, the filaments contain sections that are higher (>2 nm above the background). The filaments are not regularly distributed at the interface, and areas absent of filament are also seen (Appendix Figure 7). The difference in brightness observed by BAM must derive from regions of higher filament density, since the filaments are below the resolution limit of BAM. At a 1:10 ratio the AFM images reveals a far more irregular, rough

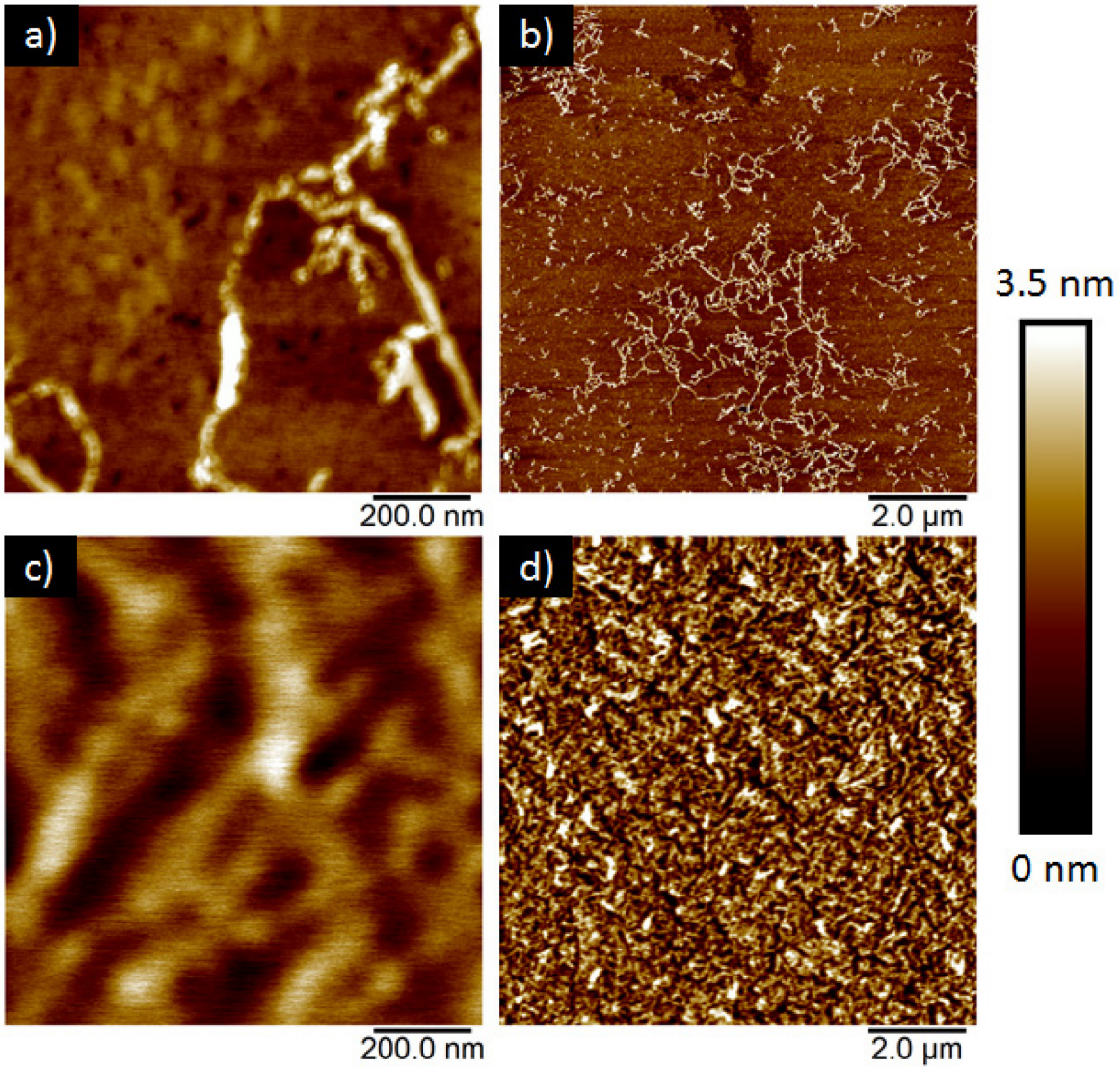

Figure 5-10 Atomic force microscopy images of ODG SH monolayers deposited by Langmuir-Blodgettry onto mica substrates at pressure of 5 mN/m. Lipid:metal ratio of 1:1 (a, b) and 1:10 (c, d)

surface with height difference between 1 to 2.5 nm. The density of bilayer and multilayer structures has now increased to cover the majority of the surface, i.e. there is no longer a continuous background nor regions of higher and lower filament density.

The ability of subphase metal ions to induce aggregated structures from Langmuir monolayers has been reported, even in the absence of a chelating group. Low concentrations of Fe^{3+} (μM) have been shown to accumulate at the DPPC interface, with as many as 3 iron ions per choline. The strong binding led to intercalation of the iron and partial disruption of the condensed phase[199]. At much higher subphase concentrations (0.1 M), Li *et al.*[201] showed that Fe^{3+} interacted with DPPC monolayers and generated lipid-iron nanoparticles that are squeezed out of the monolayer plane. In the case of chelating surfactants, the concentration at which 3D structures are formed appear to be even lower. To probe the impact of the adsorbed ions on the gallate surfactant structure, GIXD measurements were performed with ODG, the methyl terminated version, on zinc and copper ions-containing subphases (Appendix Figure 8). At a 1:10 ratio of ODG:zinc the diffraction pattern is identical to that obtained for ODG on water[172] and ODG SH on water[190], including the molecular lattice/headgroup peaks. With the same ratio of copper ions in the subphase, there is evidence of weak diffraction peaks in the same positions, however these are too weak to be fit and reflect an almost complete loss of condensed phase and/or crystallinity, see Figure 5-11.

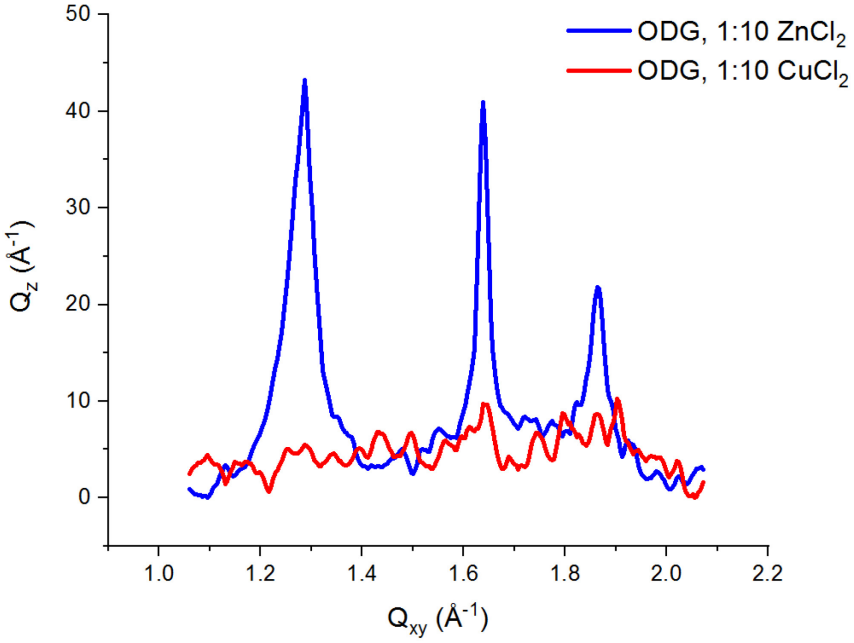

Figure 5-11 Integrated intensity of GIXD data for ODG on metal containing subphase at specific lipid:metal ratio

All data confirm that the propensity of phenol to interact with copper over zinc ions is conserved at the air-water interface, with very strong binding between the monolayer and the copper ions being observed. Despite the difference in monolayer phase between the C12 and C18 variants, there is remarkable convergence between their behaviors on copper: similar isotherm, appearance of a condensed phase (BAM), observance of multilayer filaments (AFM) and the lack of alkyl chain ordering (GIXD). This suggests that the interaction between the phenol and the metal is so strong and dominant that the impact of lengthening the chain by 6 carbons becomes inconsequential. Notably, the formation of a bi-/multi-layer would normally be expected to shift the isotherm to smaller molecular areas as some of the surfactants are removed from the water interface to form the multilayer. This is observed for LDG SH but not for ODG SH which instead exhibits a slight increase in molecular area, despite multilayer formation. Considering the loss of chain organization observed using GIXD, it is likely that the initial interaction with the copper ions with the headgroups expands the film; the increased intermolecular distance prevents efficient chain-chain van der Waals interactions thus leading to the loss of the condensed phase. It is known that gallic acid can dimerize in presence of copper ions[202], which would certainly result in a reorganization. We therefore propose that the two effects are happening concurrently when copper ions is introduced into the subphase of an ODG SH monolayer, namely multilayer formation and film expansion. The relative propensity of each of these effects can be partially controlled by the copper ions concentration. The surfactant-copper ions interaction (for either chain length) leads to a molecular area that is intermediate between that of LDG SH and ODG SH and ultimately results in the convergence of the LDG SH and ODG SH isotherms with higher copper ions concentrations. Moreover, the collapse pressure decreases for both surfactants in the presence of copper ions, indicating a low compressibility film, most likely due to a preferred area of the phenol-copper ions complex. Although the compressibility modulus reported in Figure 5-3 is lower than that expected for a condensed phase, the presence of the multilayer means that the molecular area is not accurate and the true compressibility modulus would be higher. Assuming that this new organization is the optimal conformation for copper ions binding, and that copper ions concentration can be controlled to minimize the prevalence of multilayering, this would

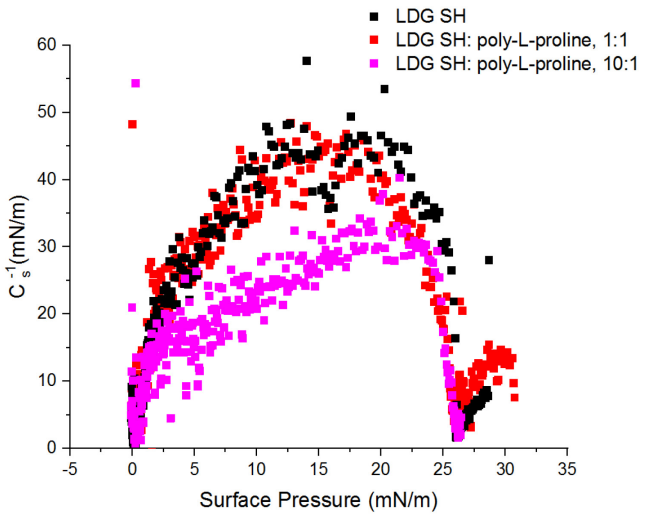

Figure 5-12 Compressibility modulus of LDG SH as a function of subphase lipid to poly-L-rpoline ratio.

allows pre-organization of the films for transfer to solid substrate in order to generate surface coatings with high binding affinity to copper ions.

In addition to metal chelation, phenols are known to bind proline-rich proteins and peptides[9]. Poly-L-proline was used to probe the binding of the gallate surfactants with proline-rich peptides. The effects of poly-L-proline dissolved in subphase on the LDG SH isotherm are shown in Figure 5-12a (poly-L-proline spread by itself at the air-water interface does not show an increase in surface pressure). At lower

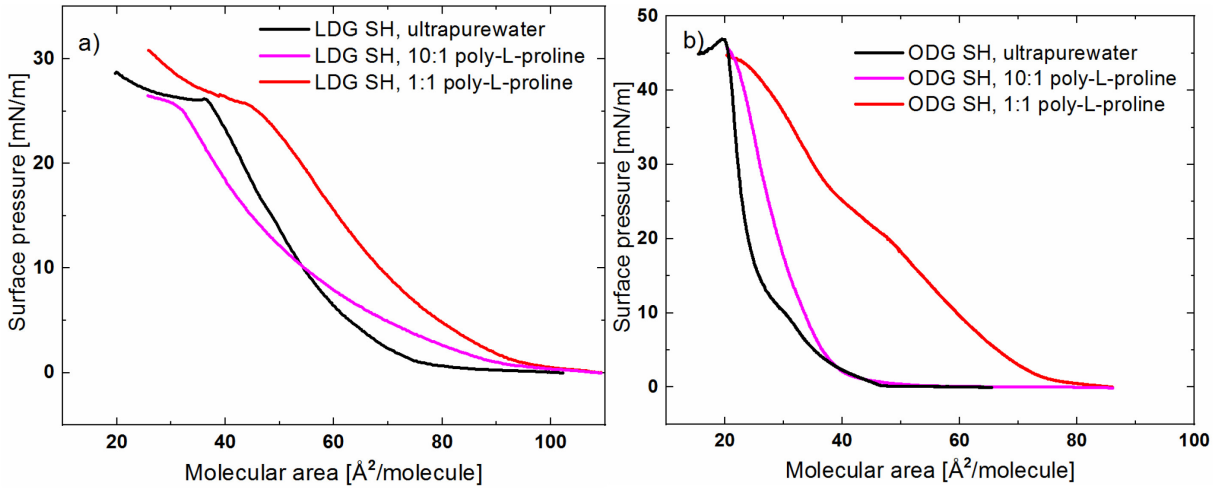

Figure 5-13 Surface pressure-molecular area isotherms of a) LDG SH and b) ODG SH as a function of lipid to poly-L-proline ratio.

peptide concentrations (higher lipid:peptide ratio), the poly-L-proline causes an increase in the critical area but a reduction in the rate at which the surface pressure increases with a reduction in the corresponding compressibility modulus (Figure 5-13). Increasing the peptide concentration yields the same isotherm slope as obtained on ultrapure water but with an increase in critical area. These changes in slope and shift to molecular areas results in no net change in compressibility compared to the films on ultrapure water. BAM imaging showed no features (data not shown), suggesting that the monolayer remains in a liquid phase. AFM imaging of deposited films with a 1:1 lipid:peptide ratio, likewise, show a homogeneous surface (Appendix Figure 9) similar to films deposited from a water subphase.

GIXD measurements of the LDG SH film in the presence of poly-L-proline (1:1) does not produce any diffraction pattern located in the region normally associated with alkyl chains, which is also the case

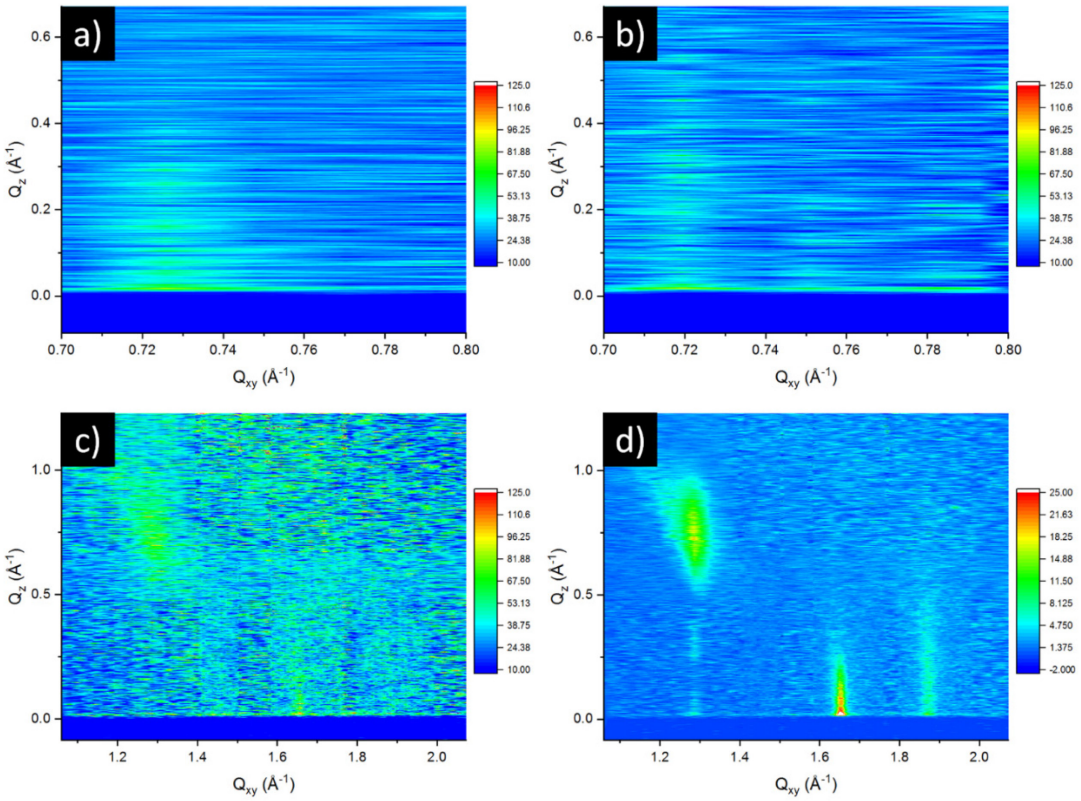

Figure 5-14 GIXD contour plots of the diffracted X-ray intensity as a function of the in-plane (Q_{xy}) and out-of-plane (Q_z) vector components over various subphase lipid:poly-L-proline ratio: a) LDG SH, 1:1 poly-L-proline, 20 mN/m, b) ODG SH, 1:1 poly-L-proline, 15 mN/m, c) ODG SH, 1:1 poly-L-proline, 25 mN/m d) ODG SH, ultrapure water, 20 mN/m

when LDG SH is spread on ultrapure water. However, a weak in-plane diffraction peak is seen at low Q_{xy} values (figure 5-14a, integrated intensity Appendix Figure 10), namely at 0.725 $Å^{-1}$ and 0.75 $Å^{-1}$, which correspond to d-spacings of 8.67 Å and 8.32 Å. These are too large for chain-chain distances, moreover, the short alkyl chains are unlikely to form a liquid-crystalline lattice. Therefore this must come from either the headgroups or the poly-L-proline. Poly-L-proline in water is known to favor the poly-prolines II helix[203] (PPII), this structure is reported to have a diameter of 7.36 Å[204] and a proline repeat distance of 9.60 Å. While these are similar to the d-spacings observed, they are not sufficiently close to attribute the diffraction peaks to those deriving from a PPII helix at the interface. Co-crystals of phenol with proline do tend to create linear alignments of proline alternating with linear assemblies of flavonoid (phenol)[205], and a similar structure could form at the air-water interface, wherein the proline organizes at the phenolic surface, either below or interdigitated. The presence of two peaks with Q_z close to 0 $Å^{-1}$ could arise from the polyproline polydispersity in which folded and unfolded peptides may interact differently with the phenolic monolayer. Alternatively, it may represent the phenol-proline unit cell with non-equivalent d-spacings. Future experiments to resolve these questions include GIXD measurements of LDG SH in the presence of monomeric proline and x-ray reflectivity to determine the thickness of the absorbed layer. Computational studies are underway to assess the level of insertion of the proline into the phenolic headgroups and the resultant organization.

Although it is not possible to assign these diffraction peaks, they represent clear evidence that the poly-L-proline has a strong affinity for the monolayer and can induce ordering of an otherwise disordered

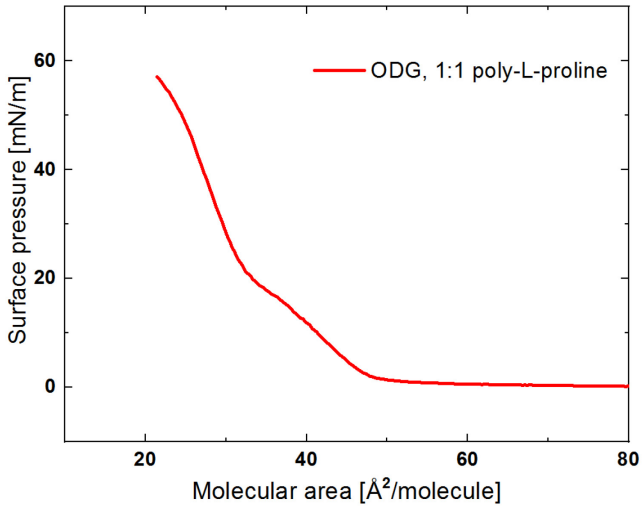

Figure 5-15 Surface pressure-molecular area isotherms of ODG on 1:1 ODG:poly-L-proline ratio.

film. MD calculations[206] for surfactants with a related headgroup (alkylbenzene sulfonate) in lyotropic liquid crystals showed that water penetration disordered the alkyl chain region without disrupting headgroup organization, supporting the notion that the small aromatic headgroups can form an ordered lattice without consequently requiring chain ordering.

The effect of poly-L-proline on ODG SH isotherms is similar in that it induces an increase in critical area (Figure 5-12b). The changes at a 10:1 surfactant:poly-L-proline ratio are relatively minor, with similar critical areas but a loss of the isotherm kink at 10 mN/m, previously reported to be associated with a bola-to-extended conformational change[190]. However at a 1:1 surfactant:poly-L-proline ratio, a much larger increase in molecular area is apparent, most likely indicating significant insertion into the monolayer. There is also the appearance of a new transition at around 20 mN/m, which is either the same

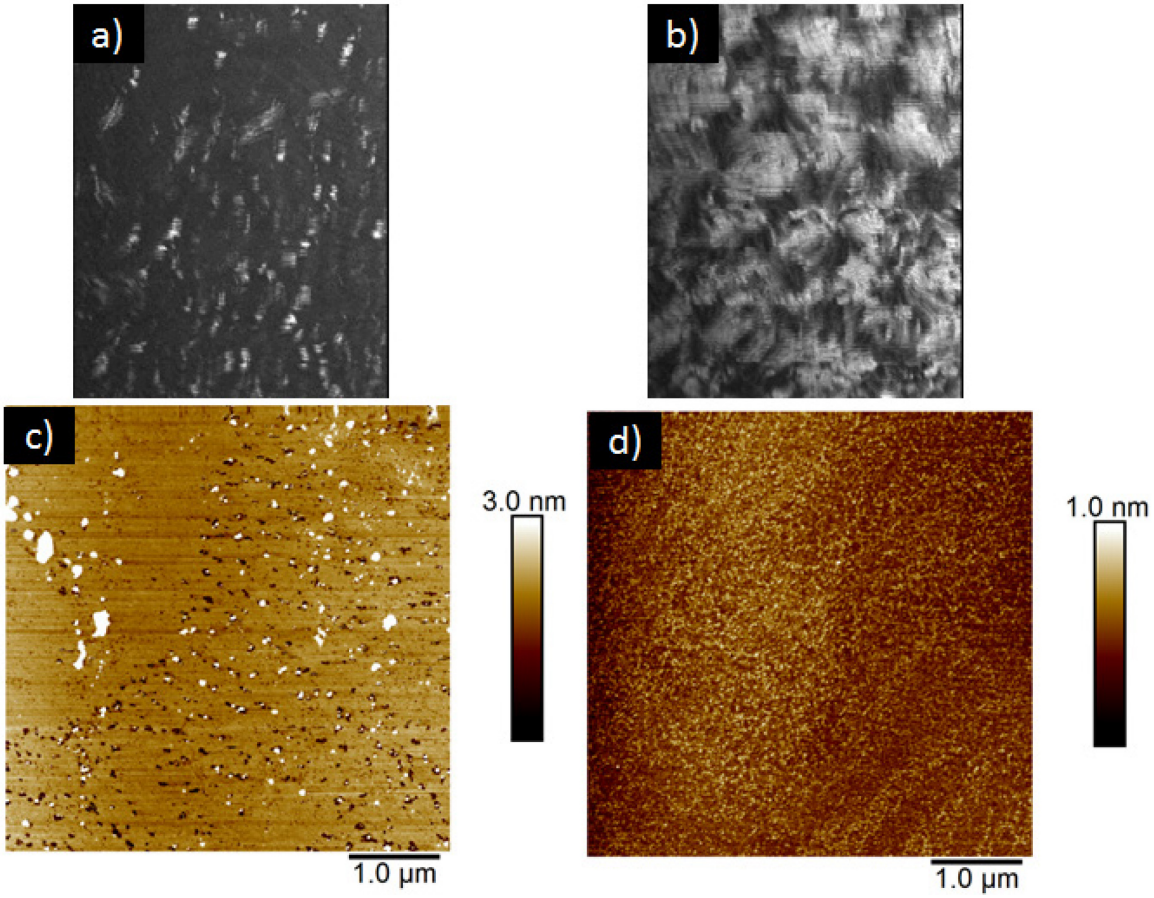

Figure 5-16 Brewster angle microscopy images of ODG SH on subphase with lipid to poly-L-proline ratio of 1:1, a) 1 mN/m, b) 30 mN/m. Atomic force microscopy images of ODG SH monolayers deposited by Langmuir-Blodgettry onto mica substrates at pressure of c) 5 mN/m, d) 20 mN/m.

surfactant conformational change shifted to higher surface pressures or a squeezing-out of the polyproline form the interface[207,208]. The appearance of a kink in the isotherm at 20 mN/m is also observed for poly-L-proline interactions with ODG, the methyl-terminated analogue (see Figure 5-15), supporting a squeezing-out rather than bola-to-extended conformational change.

Brewster angle microscopy of the 1:1 system (Figure 5-16a) shows small, bright features visible at all surface pressures below the transition (20 mN/m), in contrast to the anisotropic features observed throughout the isotherm for ODH SH on ultrapure water (Figure 5-9). Above 20 mN/m, ODG SH on poly-L-proline exhibits distinct bright and dark regions, reminiscent of the anisotropic features on a water subphase[190]. As the poly-L-proline is excluded from the interface at the transition, the surfactants should be able self-assemble into a condensed phase. AFM of a LB film at 5 mN/m (Figure 5-16c) shows a relatively flat surface dotted with both small aggregates, height of 5 to 15 nm, and small holes, with a depth of around 1.36±0.20 nm. Both features appear to be co-located which, in combination with the previously reported high rigidity, suggest that the bright features may be the result of the deposition process. Deposition at higher surface pressures, above the transition, yields rough surface absent of any large domains, although notably with a relatively low roughness of 0.11 nm. There are no signs of the large, bright aggregates seen at lower surface pressure, supporting the hypothesis that these are due to the deposition process.

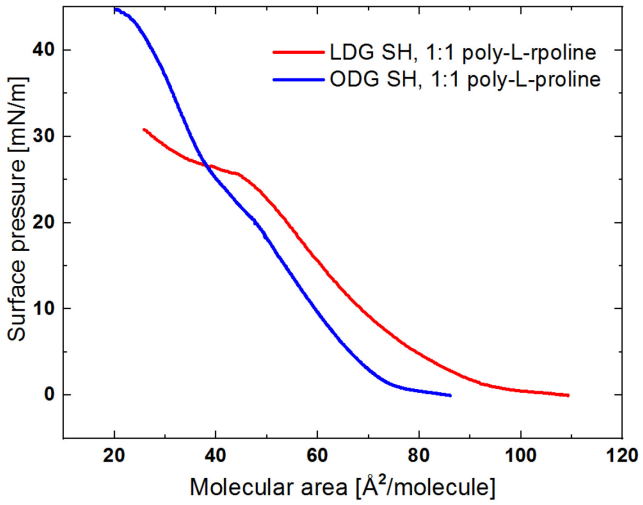

Figure 5-17 Surface pressure molecular area isotherms of ODG SH and LDG SH at 1:1 lipid:poly-L-proline ratio.

GIXD was used to determine the phases formed by the surfactant (Figure 5-14b, c). At low pressure the pattern obtained for ODG SH on poly-L-proline is very similar to that of LDG SH on the same subphase, namely a lack of alkyl peaks indicating disorder chains and similar low Q_{xy} peaks, however these are not at the exact same positions (Appendix Figure 10). By comparison, ODG and ODG SH on ultrapure water show strong alkyl chain peaks[172,190]. The similarity of the diffraction patterns for LDG SH and ODG SH at low surface pressures in the presence of poly-L-proline indicates that the poly-L-proline interacts with the phenol headgroup in the same manner and with the same result, regardless of the length of the tail and the phase of the system. The lack of alkyl chain peaks indicates that the poly-L-proline forces the surfactants far enough apart to induce a liquid expanded state for the chains. This is also reflected in the isotherms which converges toward similar molecular area with increasing amount of peptide (Figure 5-17).

Compressing the film above the transition leads to the disappearance of the peaks at low Q_{xy} and the re-appearance of the peaks normally observed in the absence of the peptide, although notably weaker (compare Figures 5-14c and d). The weaker peaks correlate well with the AFM images at the higher surface pressures in that the domains are much smaller, and irregular shaped, in the presence of the peptide. This is clear confirmation that the peptide is squeezed out at the transition, allowing the ODG to regain its close-packed organization. This behavior is in contrast to LDG SH, where the low Q_{xy} peaks never disappear as a results of compression, most likely because the surfactant adopts a liquid expanded phase with larger molecular areas even in the absence of the peptide.

5.5. Conclusions

Phenols are known to bind strongly to proline-rich proteins and to chelate metals, yet in both cases, there are specific space requirements for the interaction. This becomes important in the design and preparation of phenol-functionalized surfaces for the purposes of conferring these strong binding characteristics. In a Langmuir monolayer, achieving this space means overcoming the natural self-association properties of phenols, driven by strong π-stacking and hydrogen bonding[172]. In this work, we have demonstrated the utility of a Langmuir film, prepared in the presence of a binding partner, to modify the strong heagroup interactions, when the binding is sufficiently strong. Both copper ions and poly-L-proline interact strongly with the monolayer, even at submicromolar (10^{-7} M) subphase concentration.

Moreover, in the case of the metal ions, the specificity of the binding was demonstrated by confirming the presence of copper, but not zinc, ions at the interface. In the presence of copper ions and poly-L-proline, the phenolic surfactant headgroup organization was significantly modified. For LDG SH which nominally forms a fluid phase, the binding of copper ions condenses the film without headgroup crystallinity while with poly-L-proline, it expands the film, likely due to interdigitation, and generates an ordered headgroup region. For ODG SH, both copper ions and poly-proline expand the normally close-packed, condensed film leading to a disorganization of the chains, but while poly-L-proline interdigitating induces a new crystalline organization of the headgroup region, intercalation of copper ions appears to crosslink the headgroups into a type of condensed phase in which neither the chains nor the headgroups show long-range ordering. Notably, the films formed are dominated by the headgroup interactions, regardless of the chain length, i.e. in the presence of the corresponding binding partner, the films properties of ODG SH and LDH SH appear to be converging in terms of isotherm, morphology and structure. This opens avenues for a molecular imprinting-type of film assembly in which the desired analyte is used to pre-organize the film into the optimal organization for binding prior to assembly onto a solid substrate.

Chapter 6. Conclusion and future work

To evaluate the potential for transferring highly organised monolayers from the air-water interface onto solid substrate for the purposes of creating a functional coating, it is necessary to understand their air-water behavior and which conditions enable control over the film organisation. The gallate moiety was employed both because of its potential applications and because of the opportunity to systematically modify the headgroup interaction through hydroxyl deprotonation and subphase modification.

In most typical surfactant monolayers, the headgroup freely rotates in the water and the organisation is predominantly dictated by the chain packing, which can be modified through compression. The gallate group, however, has a very strong intermolecular (phenol-phenol) interactions in a monolayer. With the C18 alkyl chain, it creates a rigid monolayer which possesses a preferred arrangement, dictated by the headgroup area requirement, which is unmodified by compression. Even the addition of an ω-thiol group, thus replacing a terminal hydrophobic group by a hydrophilic one, does not initially cause any significant change to the film organisation, the hydrogen bond and π-stacking network being strong enough to retain the same organisation. However this is not the most stable conformation for the thiolated surfactant and with time a new organisation evolves, with the surfactant adopting a bola form. This organisation has a much larger surface area, however compression forces the monolayer back into the extended form, yielding an organization identical to that observed with the methyl-terminated surfactant.

With three hydroxyl moieties in the headgroup, in principle these strong inter-headgroup interactions, and hence the film organization, can be modified by changing their protonation state. Deprotonation of the headgroups does not initially modify the organisation of the methyl terminated alkyl gallate surfactants, however it does generate sufficient inter-domain repulsion to oppose coalescence and cause the domain to become smaller. This reduced domain size due to repulsion in turn causes the thiol terminated surfactant to convert from the extended to bola form at a faster rate, most likely because the conversion occurs at the boundary of the domains. This conformational change can still be reversed through compression.

The electrostatic repulsion of a single deprotonation by itself is not enough to disrupt the organisation, however multiple deprotonations weaken the hydrogen bond network sufficiently for a new organisation to be adopted. This could be due to the greater electrostatic repulsion between neighboring

surfactants or it could be due to the ion-dipole interactions having different area requirements than the hydrogen bond they replace, one that may in turn push the aromatic rings further apart thus weakening the π-stacking interactions that contribute to holding the system in a rigid conformation. The likelihood of this second possibility is reinforced by the behavior of the phenol surfactant when in the liquid expanded phase, achieved with a shorter chain. In contrast to ODG, which exhibits a film expansion with increasing pH, the shorter chain LDG exhibits a shift to smaller molecular areas, indicative of stronger intermolecular interactions; this was supported by AFM measurements, which reveal the presence of domains.

The new film organisation observed at high pH manifests itself differently for the C18 methyl and thiol surfactants. For the methyl-terminated surfactant, the headgroup organisation is weakened at high pH, as evidenced by the disappearance of the GIXD peaks associated with headgroup lattice. This allows the chains to adopt a more compact organisation with a much lower tilt angle. In the case of the thiol, the weakened headgroup network causes a faster transformation to a bola form, with the complete disappearance of any GIXD peaks. Compression can be used to force the system back into an extended conformation but, due to the presence of the ω-thiol, a slightly different organisation is generated and the formation of defined multilayers is favored. This has profound implications for the deposition of the system onto a gold support, since only part of the multilayer can chemisorb with the gold and any material in the multilayer not directly in contact with the gold is therefore not deposited. The extent of this multilayering can be controlled via the deposition pressure, which allows the selectivity of the dominant form present at the air-water interface. Similar control is afforded at lower pH, where surface pressure can dictate whether the major species is bola or extended. In this way different deposited films have been created with different thicknesses and, presumably, lateral surfactant distances.

More work will be needed to elucidate the protonation state of the gallate headgroup, this can take two different approaches. New surfactants with different hydroxyl substitution patterns can be synthesised (e.g. mono- and di-hydroxyl substituted) and studied as a function of pH, to contrast with the tri-hydroxyl (gallate) headgroup. In particular, selectively removing a meta- or para-hydroxyl may shed light on the individual pKa's for each position and their relative importance in determining the headgroup organization. Alternatively, it has been reported that the UV absorption of methyl gallate shift with deprotonation of the gallate in dilute [209]. Thus employing a surface-specific spectroscopic technique for

measurements directly at the air-water interface[210] can be used to monitor the changes brought about due to deprotonation.

The headgroup rigid organisation can also be disrupted by introducing subphase components that have a natural affinity for the phenol groups, which limit the neighboring phenol-phenol interactions. When metals are used, their drastic differences in affinity for the monolayer are evident: zinc ions are undetected at the interface and the hydrogen bond network is intact, potentially because the interaction of the zinc ions with phenol is much weaker than the phenol-phenol interactions. Copper ions on the other hand showed a very high enrichment at the interface compared to the subphase concentration. The monolayer organisation is completely disrupted, both chain and headgroup, in the case of ODG. The copper ions are forcing the monolayer into a new organisation with a different inter-phenol distance. The exact nature of the interaction between the gallate and the copper at the air-water interface will need to be investigated. A significant re-orientation of the gallate may be required for chelation with the copper ions. The coordination environment for copper (II) complexes can include tetragonal (most common), tetrahedral, square planar and trigonal bipyramidal[211], not all of which may be achievable given the constraints of the 2D film. Additionally, the interaction of gallate with copper ions in solution is not fully understood, whether or not an oxidation reaction occurs has been called into question[202]. A surface-specific spectroscopy such as sum frequency generation would be needed to yield information about the orientational changes in the gallate ring upon binding to copper.

A similar situation arises when poly-L-proline is introduced into the subphase. The usual organisation is disrupted by the strong phenol-proline interactions. However, the new lattice extracted from GIXD measurements cannot yet be assigned to either poly-L-proline, phenol or a combination thereof. With both poly-L-proline and copper ions, the headgroup-analyte interactions are much stronger and this causes both long and short chain surfactant to behave very similarly, since the increase in interaction potential energy arising from the additional six-carbons in the chain is significantly less than the interaction potential generated by the headgroup-analyte interactions. It is hoped that transferring films with this pre-defined organization will translate into stronger binding affinity for the desired analyte with the deposited film.

Some very preliminary work has been carried out using surface plasmon resonance (SPR) using poly-L-proline binding to films deposited under different conditions. When a poly-L-proline solution is flowed over a deposited monolayer film of LDG SH onto gold, binding is registered but once the running solution is returned to ultrapurewater the response returns to baseline, indicating that the poly-L-proline easily desorbs. When the deposited film is a monolayer comprising 50:50 LDG:LDG SH that is subsequently washed to remove the unreacted, methyl-terminated surfactant, thereby giving more conformational freedom to the remaining chemisorbed thiol, the response does not return to baseline, indicating that some of the poly-L-proline remains bound to the surface, demonstrating a stronger binding (example of preliminary data included Appendix Figure 11).

Further SPR work will need to be carried over a wider range of deposition conditions (surfactant, composition, pressure, subphase pH and presence of analyte in subphases) to confirm differences in binding due to film organization. Additionally, SPR may not be sensitive enough to detect metal binding to the surface, so to measure the interaction of the deposited film with metals it may be necessary to use quartz crystal microbalance (QCMD). Moreover, given the known strong binding affinity of phenols such as catechol with iron[2], this may be a good candidate for study. However, iron (III) chloride is known to form iron clusters at neutral pH[212] and therefore a larger study of this in the context of different pHs would be required.

The deposited films themselves will need to be further scrutinized as no direct evidence of chemisorption of the thiol to the gold surface has yet been obtained. X-ray photoelectron spectroscopy (XPS) which would reveal the oxidation state of the sulfur, could be used to confirm the chemisoprtion. Furthermore, grazing incidence small-angle X-ray scattering (GISAXS) at the air-solid interface can be used to compare the deposited film organisation to the organisation seen by GIXD at the air-water interface, to determine how much the deposition process alters the organisation. The nature of the hydrophobic gold and the exact steps in which the depositions occur will also need to be scrutinized, the filmed obtain by Langmuir-Blodgett transfer onto hydrophobic gold will need to be compared to film obtained trough different deposition technique and gold nature.

The deposition strategy can also be diversified. Expanding on the idea of deposition from mixtures of thiol- and methyl-terminated surfactants, it should be possible to back fill the space left behind in the

monolayer from the removal of the methyl terminated surfactant using short chain alkyl thiol. By controlling the length of the alkyl chain the rigidity and conformational freedom of the phenol group can most likely be fine-tuned.

The interaction of phenolic air-water monolayers with peptides also needs to be further studied to determine the species involved in the lattice structure seen by GIXD. Some potential experiments that can be envisaged include spreading the monolayer on a subphase containing free proline, or other amino acids which should make it possible to see whether the organisation observed is also disrupted in a similar fashion as with the poly-L-proline. Also comparing poly-L-proline to other peptides, one that may, or may not, be rich in proline, could shed light on the necessity and/or presence of the secondary structure. Computational studies are ongoing to shed further light on these interactions.

In this thesis, the focus has been on single-chain, trihydroxy surfactants. Additional parameters which will influence the headgroup organization include both modification of the number and placement of the hydroxyl groups on the headgroup which will alter the balance between π-stacking and hydrogen bonding as well as introducing a second chain which will yield greater space and hence more conformational freedom for the headgroup. GIXD data has been collected for such systems at the air-water interface and computational studies are ongoing.

The focus of this thesis was to investigate the potential to control the surfactant intermolecular spacing at the air-water interface for transfer onto solid support using gold thiol chemistry, creating robust functional surface films. In particular, the aim was to generate a tannin-mimetic surface coating using a gallate-based surfactant. On a fundamental level, the strong gallate intermolecular interactions, and the ability to generate charged forms of this heagroup, provided insight into the balance of π-stacking, hydrogen bonding and ionic interactions in defining film structure and organization at different length scales. We also demonstrated that the introduction of an ω-thiol, necessary for chemisorption to gold, does not necessarily disrupt this organization, but careful control of spreading conditions is required. These concepts are more broadly applicable than just the gallate-derived surfactant studied here. A preliminary study of molecular imprinting the required spacing for analyte binding was undertaken but further study is required.

References

(1) Haslam, E. Natural Polyphenols (Vegetable Tannins) as Drugs: Possible Modes of Action. *J. Nat. Prod.* **1996**, *59* (2), 205–215.

(2) Quideau, S.; Deffieux, D.; Douat-Casassus, C.; Pouységu, L. Plant Polyphenols: Chemical Properties, Biological Activities, and Synthesis. *Angew. Chemie Int. Ed.* **2011**, *50* (3), 586–621.

(3) Poncet-Legrand, C.; Edelmann, A.; Putaux, J.-L.; Cartalade, D.; Sarni-Manchado, P.; Vernhet, A. Poly(l-Proline) Interactions with Flavan-3-Ols Units: Influence of the Molecular Structure and the Polyphenol/Protein Ratio. *Food Hydrocoll.* **2006**, *20* (5), 687–697.

(4) Soares, S.; Mateus, N.; de Freitas, V. Interaction of Different Classes of Salivary Proteins with Food Tannins. *Food Res. Int.* **2012**, *49* (2), 807–813.

(5) Shimada, T. Salivary Proteins as a Defense Against Dietary Tannins. *J. Chem. Ecol.* **2006**, *32* (6), 1149–1163.

(6) Sathyapriya, S.; Bharani, G.; Nangalingam, M.; Jayanthi, M.; Kanagavalli, U. Potential of Salivary Protein as a Biomarker in Prognosis of Diabetes Mellitus. *J. Pharm. Res.* **2011**, *4* (7), 2228–2229.

(7) Levine, M. Susceptibility to Dental Caries and the Salivary Proline-Rich Proteins. *Int. J. Dent.* **2011**, *2011*, 1–13.

(8) Carregaro, F.; Stefanini, A. C. B.; Henrique, T.; Tajara, E. H. Study of Small Proline-Rich Proteins (SPRRs) in Health and Disease: A Review of the Literature. *Arch. Dermatol. Res.* **2013**, *305* (10), 857–866.

(9) Baxter, N. J.; Lilley, T. H.; Haslam, E.; Williamson, M. P. Multiple Interactions between Polyphenols and a Salivary Proline-Rich Protein Repeat Result in Complexation and Precipitation. *Biochemistry* **1997**, *36* (18), 5566–5577.

(10) Soares, S.; García-Estévez, I.; Ferrer-Galego, R.; Brás, N. F.; Brandão, E.; Silva, M.; Teixeira, N.; Fonseca, F.; Sousa, S. F.; Ferreira-da-Silva, F.; et al. Study of Human Salivary Proline-Rich

Proteins Interaction with Food Tannins. *Food Chem.* **2018**, *243*, 175–185.

(11) Bourvellec, C. Le; Renard, C. M. G. C. Interactions between Polyphenols and Macromolecules: Quantification Methods and Mechanisms. *Crit. Rev. Food Sci. Nutr.* **2012**, *52* (3), 213–248.

(12) Murray, N. J.; Williamson, M. P.; Lilley, T. H.; Haslam, E. Study of the Interaction between Salivary Proline-Rich Proteins and a Polyphenol by 1H-NMR Spectroscopy. *Eur. J. Biochem.* **1994**, *219* (3), 923–935.

(13) Williamson, M. P. The Structure and Function of Proline-Rich Regions in Proteins. *Biochem. J.* **1994**, *297 (Pt 2* (Pt 2), 249–260.

(14) Vergé, S.; Richard, T.; Moreau, S.; Nurich, A.; Merillon, J.-M.; Vercauteren, J.; Monti, J.-P. First Observation of Solution Structures of Bradykinin–penta-O-Galloyl-d-Glucopyranose Complexes as Determined by NMR and Simulated Annealing. *Biochim. Biophys. Acta - Gen. Subj.* **2002**, *1571* (2), 89–101.

(15) Hanton, L. R.; Hunter, C. A.; Purvis, D. H. Structural Consequences of a Molecular Assembly That Is Deficient in Hydrogen-Bond Acceptors. *J. Chem. Soc. Chem. Commun.* **1992**, No. 16, 1134–1136.

(16) Yan, Q.; Bennick, A. Identification of Histatins as Tannin-Binding Proteins in Human Saliva. *Biochem. J.* **1995**, *311* (1), 341–347.

(17) South, P. K.; Miller, D. D. Iron Binding by Tannic Acid: Effects of Selected Ligands. *Food Chem.* **1998**, *63* (2), 167–172.

(18) Fu, F.; Wang, Q. Removal of Heavy Metal Ions from Wastewaters: A Review. *J. Environ. Manage.* **2011**, *92* (3), 407–418.

(19) Kasprzak, M. M.; Erxleben, A.; Ochocki, J. Properties and Applications of Flavonoid Metal Complexes. *RSC Adv.* **2015**, *5* (57), 45853–45877.

(20) Guy, R. D.; Chakrabarti, C. L. Studies of Metal–organic Interactions in Model Systems Pertaining

to Natural Waters. *Can. J. Chem.* **1976**, *54* (16), 2600–2611.

(21) Hider, R. C.; Liu, Z. D.; Khodr, H. H. Metal Chelation of Polyphenols. In *Flavonoids and Other Polyphenols*; Methods in Enzymology; Academic Press, 2001; Vol. 335, pp 190–203.

(22) Fazary, A. E.; Taha, M.; Ju, Y.-H. Iron Complexation Studies of Gallic Acid. *J. Chem. Eng. Data* **2009**, *54* (1), 35–42.

(23) McDonald, M.; Mila, I.; Scalbert, A. Precipitation of Metal Ions by Plant Polyphenols: Optimal Conditions and Origin of Precipitation. *J. Agric. Food Chem.* **1996**, *44* (2), 599–606.

(24) Janasek, D.; Franzke, J.; Manz, A. Scaling and the Design of Miniaturized Chemical-Analysis Systems. *Nature* **2006**, *442* (7101), 374–380.

(25) Takai, E.; Hirano, A.; Shiraki, K. Effects of Alkyl Chain Length of Gallate on Self-Association and Membrane Binding. *J. Biochem.* **2011**, *150* (2), 165–171.

(26) Maldonado, O. S.; Lucas, R.; Comelles, F.; González, M. J.; Parra, J. L.; Medina, I.; Morales, J. C. Synthesis and Characterization of Phenolic Antioxidants with Surfactant Properties: Glucosyl- and Glucuronosyl Alkyl Gallates. *Tetrahedron* **2011**, *67* (38), 7268–7279.

(27) Ortega, E.; Sadaba, M. C.; Ortiz, A. I.; Cespon, C.; Rocamora, A.; Escolano, J. M.; Roy, G.; Villar, L. M.; Gonzalez-Porque, P. Tumoricidal Activity of Lauryl Gallate towards Chemically Induced Skin Tumours in Mice. *Br. J. Cancer* **2003**, *88* (6), 940–943.

(28) Kubo, I.; Xiao, P.; Fujita, K. Antifungal Activity of Octyl Gallate: Structural Criteria and Mode of Action. *Bioorg. Med. Chem. Lett.* **2001**, *11* (3), 347–350.

(29) Kubo, I.; Xiao, P.; Fujita, K. Anti-MRSA Activity of Alkyl Gallates. *Bioorg. Med. Chem. Lett.* **2002**, *12* (2), 113–116.

(30) Uozaki, M.; Yamasaki, H.; Katsuyama, Y.; Higuchi, M.; Higuti, T.; Koyama, A. H. Antiviral Effect of Octyl Gallate against DNA and RNA Viruses. *Antiviral Res.* **2007**, *73* (2), 85–91.

(31) Kubo, I.; Masuoka, N.; Xiao, P.; Haraguchi, H. Antioxidant Activity of Dodecyl Gallate. *J. Agric.*

Food Chem. **2002**, *50* (12), 3533–3539.

(32) Jurak, M.; Miñones, J. Interactions of Lauryl Gallate with Phospholipid Components of Biological Membranes. *Biochim. Biophys. Acta - Biomembr.* **2016**, *1858* (8), 1821–1832.

(33) Jurak, M.; Mroczka, R.; Łopucki, R. Properties of Artificial Phospholipid Membranes Containing Lauryl Gallate or Cholesterol. *J. Membr. Biol.* **2018**, *251* (2), 277–294.

(34) Jurak, M. Effect of Lauryl Gallate on Wetting Properties of Organized Thin Phospholipid Films on Mica. *J. Phys. Chem. B* **2016**, *120* (27), 6657–6666.

(35) Jurak, M. Surface Free Energy of Organized Phospholipid/Lauryl Gallate Monolayers on Mica. *Colloids Surfaces A Physicochem. Eng. Asp.* **2016**, *510*, 213–220.

(36) Jurak, M.; Mroczka, R.; Łopucki, R.; Wiącek, A. E. Structure and Wettability of Heterogeneous Monomolecular Films of Phospholipids with Cholesterol or Lauryl Gallate. *Appl. Surf. Sci.* **2019**, *493*, 1021–1031.

(37) Schmidt, R.; DeWolf, C. E. Monolayer Behavior of 1,2-Dipalmitoylgalloylglycerol, a Synthetic Lipid with Strong Cohesive Properties. *Langmuir* **2004**, *20* (8), 3284–3288.

(38) Zhao, Y. Monolayer Behavior of Phenolic Lipids : Experimental and Computational Studies, Concordia University, 2008.

(39) Taylor, C. D.; Anderson, M. R. Self-Assembled Monolayers of Positional Isomers of (12-Mercaptododecyloxy)Phenol: The Role of Molecular Structure on Interfacial Properties. *Langmuir* **2002**, *18* (1), 120–126.

(40) Azmi, A. A.; Ebralidze, I. I.; Dickson, S. E.; Horton, J. H. Characterization of Hydroxyphenol-Terminated Alkanethiol Self-Assembled Monolayers: Interactions with Phosphates by Chemical Force Spectrometry. *J. Colloid Interface Sci.* **2013**, *393*, 352–360.

(41) Dannenberg, J. J.; Jeffrey, G. A. An Introduction to Hydrogen Bonding. *J. Am. Chem. Soc.* **1998**, *120* (22), 5604–5604.

(42) Zhao, B.; Mulkey, D.; Brittain, W. J.; Chen, Z.; Foster, M. D. Synthesis and Characterization of Phenol- and o-Chlorophenol-Terminated Monolayers. *Langmuir* **1999**, *15* (20), 6856–6861.

(43) Adam, N. K. The Structure of Thin Films. Part IV. Benzene Derivatives. A Condition of Stability in Monomolecular Films. *Proc. R. Soc. A Math. Phys. Eng. Sci.* **1923**, *103* (723), 676–687.

(44) Giles, C. H.; Neustadter, E. L. 166. Researches on Monolayers. Part I. Molecular Areas and Orientation at Water Surfaces of Aromatic Azo-Compounds Containing Long Alkyl Chains. *J. Chem. Soc.* **1952**, No. 0, 918–923.

(45) Peikert, M.; Chen, X.; Chi, L.; Brezesinski, G.; Janich, S.; Würthwein, E.-U.; Schäfer, H. J. Phase Behavior and Molecular Packing of Octadecyl Phenols and Their Methyl Ethers at the Air/Water Interface. *Langmuir* **2014**, *30* (20), 5780–5789.

(46) Brezesinski, G.; Dobner, B.; Stefaniu, C.; Vollhardt, D. Monolayer Characteristics of a Long-Chain N,O-Diacyl Substituted Ethanolamine at the Air/Water Interface. *Langmuir* **2011**, *27* (9), 5386–5392.

(47) Wang, L.; Jacobi, S.; Sun, J.; Overs, M.; Fuchs, H.; Schaefer, H. J.; Zhang, X.; Shen, J.; Chi, L. Anisotropic Aggregation and Phase Transition in Langmuir Monolayers of Methyl/Ethyl Esters of 2,3-Dihydroxy Fatty Acids. *J. Colloid Interface Sci.* **2005**, *285* (2), 814–820.

(48) Hossain, M. M.; Iimura, K.; Yoshida, M.; Kato, T. Temperature Dependent Dendritic Domain Shapes in Langmuir Monolayers of Tetradecanoyl N-Ethanolamide at the Air-Water Interface. *J. Colloid Interface Sci.* **2011**, *353* (1), 220—224.

(49) Ariga, K.; Kunitake, T. Molecular Recognition at Air−Water and Related Interfaces: Complementary Hydrogen Bonding and Multisite Interaction. *Acc. Chem. Res.* **1998**, *31* (6), 371–378.

(50) Johann, R.; Brezesinski, G.; Vollhardt, D.; Möhwald, H. The Effect of Headgroup Interactions on Structure and Morphology of Arachidic Acid Monolayers. *J. Phys. Chem. B* **2001**, *105* (15), 2957–2965.

(51) Schulz, E. P.; Piñeiro, Á.; Miñones, J.; Miñones Trillo, J.; Frechero, M. A.; Pieroni, O.; Schulz, P. C. Effect of Ionization on the Behavior of N-Eicosanephosphonic Acid Monolayers at the Air/Water Interface. Experimental Determinations and Molecular Dynamics Simulations. *Langmuir* **2015**, *31* (8), 2269–2280.

(52) Gershfeld, N. L.; Pak, C. Y. O. The Surface Chemistry of Monooctadecyl Phosphate at the Air/Water Interface. A Study of Molecular Aggregation in Monolayers. *J. Colloid Interface Sci.* **1967**, *23* (2), 215–220.

(53) Wheeler, S. E. Local Nature of Substituent Effects in Stacking Interactions. *J. Am. Chem. Soc.* **2011**, *133* (26), 10262–10274.

(54) Hunter, C. A.; Sanders, J. K. M. The Nature of .Pi.-.Pi. Interactions. *J. Am. Chem. Soc.* **1990**, *112* (14), 5525–5534.

(55) Garg, N.; Carrasquillo-Molina, E.; Lee, T. R. Self-Assembled Monolayers Composed of Aromatic Thiols on Gold: Structural Characterization and Thermal Stability in Solution. *Langmuir* **2002**, *18* (7), 2717–2726.

(56) Zhang, Z.; Zheng, D.; Guo, Y.; Wang, H. Water Penetration/Accommodation and Phase Behaviour of the Neutral Langmuir Monolayer at the Air/Water Interface Probed with Sum Frequency Generation Vibrational Spectroscopy (SFG-VS). *Phys. Chem. Chem. Phys.* **2009**, *11* (6), 991–1002.

(57) Ulman, A. Formation and Structure of Self-Assembled Monolayers. *Chem. Rev.* **1996**, *96* (4), 1533–1554.

(58) Bain, C. D.; Troughton, E. B.; Tao, Y. T.; Evall, J.; Whitesides, G. M.; Nuzzo, R. G. Formation of Monolayer Films by the Spontaneous Assembly of Organic Thiols from Solution onto Gold. *J. Am. Chem. Soc.* **1989**, *111* (1), 321–335.

(59) Folkers, J. P.; Laibinis, P. E.; Whitesides, G. M. Self-Assembled Monolayers of Alkanethiols on Gold: Comparisons of Monolayers Containing Mixtures of Short- and Long-Chain Constituents

with Methyl and Hydroxymethyl Terminal Groups. *Langmuir* **1992**, *8* (5), 1330–1341.

(60) King, D. E. Oxidation of Gold by Ultraviolet Light and Ozone at 25 °C. *J. Vac. Sci. Technol. A* **1995**, *13* (3), 1247–1253.

(61) Xue, Y.; Li, X.; Li, H.; Zhang, W. Quantifying Thiol–gold Interactions towards the Efficient Strength Control. *Nat. Commun.* **2014**, *5* (1), 4348.

(62) Pensa, E.; Cortés, E.; Corthey, G.; Carro, P.; Vericat, C.; Fonticelli, M. H.; Benítez, G.; Rubert, A. A.; Salvarezza, R. C. The Chemistry of the Sulfur–Gold Interface: In Search of a Unified Model. *Acc. Chem. Res.* **2012**, *45* (8), 1183–1192.

(63) Ishida, T.; Yamamoto, S.; Mizutani, W.; Motomatsu, M.; Tokumoto, H.; Hokari, H.; Azehara, H.; Fujihira, M. Evidence for Cleavage of Disulfides in the Self-Assembled Monolayer on Au(111). *Langmuir* **1997**, *13* (13), 3261–3265.

(64) Bürgi, T. Properties of the Gold–sulphur Interface: From Self-Assembled Monolayers to Clusters. *Nanoscale* **2015**, *7* (38), 15553–15567.

(65) Stranick, S. J.; Parikh, A. N.; Allara, D. L.; Weiss, P. S. A New Mechanism for Surface Diffusion: Motion of a Substrate-Adsorbate Complex. *J. Phys. Chem.* **1994**, *98* (43), 11136–11142.

(66) Stranick, S. J.; Parikh, A. N.; Tao, Y.-T.; Allara, D. L.; Weiss, P. S. Phase Separation of Mixed-Composition Self-Assembled Monolayers into Nanometer Scale Molecular Domains. *J. Phys. Chem.* **1994**, *98* (31), 7636–7646.

(67) Trevor, D. J.; Chidsey, C. E. D.; Loiacono, D. N. In Situ Scanning-Tunneling-Microscope Observation of Roughening, Annealing, and Dissolution of Gold (111) in an Electrochemical Cell. In *Scanning Tunneling Microscopy*; Neddermeyer, H., Ed.; Springer Netherlands: Dordrecht, 1993; pp 209–212.

(68) Park, W.; Rhie, J.; Kim, N. Y.; Hong, S.; Kim, D.-S. Sub-10 Nm Feature Chromium Photomasks for Contact Lithography Patterning of Square Metal Ring Arrays. *Sci. Rep.* **2016**, *6*, 23823.

(69) Alom Ruiz, S.; Chen, C. S. Microcontact Printing: A Tool to Pattern. *Soft Matter* **2007**, *3* (2), 168–177.

(70) Ponzio, F.; Payamyar, P.; Schneider, A.; Winterhalter, M.; Bour, J.; Addiego, F.; Krafft, M.-P.; Hemmerle, J.; Ball, V. Polydopamine Films from the Forgotten Air/Water Interface. *J. Phys. Chem. Lett.* **2014**, *5* (19), 3436–3440.

(71) Müller, V.; Hinaut, A.; Moradi, M.; Baljozovic, M.; Jung, T. A.; Shahgaldian, P.; Möhwald, H.; Hofer, G.; Kröger, M.; King, B. T.; et al. A Two-Dimensional Polymer Synthesized at the Air/Water Interface. *Angew. Chemie Int. Ed.* **2018**, *57* (33), 10584–10588.

(72) Chen, L.; Wang, X.; Lu, W.; Wu, X.; Li, J. Molecular Imprinting: Perspectives and Applications. *Chem. Soc. Rev.* **2016**, *45* (8), 2137–2211.

(73) Alexander, C.; Andersson, H. S.; Andersson, L. I.; Ansell, R. J.; Kirsch, N.; Nicholls, I. A.; O'Mahony, J.; Whitcombe, M. J. Molecular Imprinting Science and Technology: A Survey of the Literature for the Years up to and Including 2003. *J. Mol. Recognit.* **2006**, *19* (2), 106–180.

(74) Petcu, M.; Cooney, J.; Cook, C.; Lauren, D.; Schaare, P.; Holland, P. Molecular Imprinting of a Small Substituted Phenol of Biological Importance. *Anal. Chim. Acta* **2001**, *435* (1), 49–55.

(75) Gryshchenko, A. O.; Bottaro, C. S. Development of Molecularly Imprinted Polymer in Porous Film Format for Binding of Phenol and Alkylphenols from Water. *Int. J. Mol. Sci.* **2014**, *15* (1), 1338–1357.

(76) Xue, X.; Wei, Q.; Wu, D.; Li, H.; Zhang, Y.; Feng, R.; Du, B. Determination of Methyl Parathion by a Molecularly Imprinted Sensor Based on Nitrogen Doped Graphene Sheets. *Electrochim. Acta* **2014**, *116*, 366–371.

(77) Pradeep, T.; Feng, B.; Ast, T.; Patrick, J. S.; Cooks, R. G.; Pachuta, S. J. Chemical Modification of Fluorinated Self-Assembled Monolayer Surfaces by Low Energy Reactive Ion Bombardment. *J. Am. Soc. Mass Spectrom.* **1995**, *6* (3), 187–194.

(78) Kim, T. K.; Yang, X. M.; Peters, R. D.; Sohn, B. H.; Nealey, P. F. Chemical Modification of Self-

Assembled Monolayers by Exposure to Soft X-Rays in Air. *J. Phys. Chem. B* **2000**, *104* (31), 7403–7410.

(79) Haensch, C.; Hoeppener, S.; Schubert, U. S. Chemical Modification of Self-Assembled Silane Based Monolayers by Surface Reactions. *Chem. Soc. Rev.* **2010**, *39* (6), 2323.

(80) Gooding, J. J.; Ciampi, S. The Molecular Level Modification of Surfaces: From Self-Assembled Monolayers to Complex Molecular Assemblies. *Chem. Soc. Rev.* **2011**, *40* (5), 2704–2718.

(81) Choi, I.; Kim, Y.; Kang, S. K.; Lee, J.; Yi, J. Phase Separation of a Mixed Self-Assembled Monolayer Prepared via a Stepwise Method. *Langmuir* **2006**, *22* (11), 4885–4889.

(82) Singh, A.; Dahanayaka, D. H.; Biswas, A.; Bumm, L. A.; Halterman, R. L. Molecularly Ordered Decanethiolate Self-Assembled Monolayers on Au(111) from in Situ Cleaved Decanethioacetate: An NMR and STM Study of the Efficacy of Reagents for Thioacetate Cleavage. *Langmuir* **2010**, *26* (16), 13221–13226.

(83) Medina-Plaza, C.; de Saja, J. A.; Fernández-Escudero, J. A.; Barajas, E.; Medrano, G.; Rodriguez-Mendez, M. L. Array of Biosensors for Discrimination of Grapes According to Grape Variety, Vintage and Ripeness. *Anal. Chim. Acta* **2016**, *947*, 16–22.

(84) Tang, N. Y.-W.; Badia, A. Self-Patterned Mixed Phospholipid Monolayers for the Spatially Selective Deposition of Metals. *Langmuir* **2010**, *26* (22), 17058–17067.

(85) Gyepi-Garbrah, S. H.; Šilerová, R. The First Direct Comparison of Self-Assembly and Langmuir–Blodgett Deposition Techniques: Two Routes to Highly Organized Monolayers. *Phys. Chem. Chem. Phys.* **2002**, *4* (14), 3436–3442.

(86) Slowinski, K.; Bilewicz, R.; Kublik, Z. Langmuir–Blodgett Monolayer Modified Electrodes Based on Thiol-Derived Bifunctional Alkanes. *Electrochem. commun.* **1999**, *1* (10), 437–440.

(87) Duschl, C.; Liley, M.; Corradin, G.; Vogel, H. Biologically Addressable Monolayer Structures Formed by Templates of Sulfur-Bearing Molecules. *Biophys. J.* **1994**, *67* (3), 1229–1237.

(88) Kageyama, M.; Yahiro, Y.; Karube, S.; Shiraku, T.; Kato, T.; Kato, N.; Kashiwai, T.; Nomura, M.; Nishida, Y.; Tagaki, N.; et al. Adsorption of Dimethyl Silicone onto Hair-Surface Models Prepared with Micro-Phase Separated Monolayers. *J. Oleo Sci.* **2014**, *63* (4), 355–363.

(89) Ihalainen, P.; Peltonen, J. Covalent Immobilization of Antibody Fragments onto Langmuir−Schaefer Binary Monolayers Chemisorbed on Gold. *Langmuir* **2002**, *18* (12), 4953–4962.

(90) Characteristic Features of Surfactants. In *Surfactants and Interfacial Phenomena*; John Wiley & Sons, Ltd, 2012; pp 1–38.

(91) Rogalska, E.; Bilewicz, R.; Brigaud, T.; Moujahid, C. El; Foulard, G.; Portella, C.; Stébé, M.-J. Formation and Properties of Langmuir and Gibbs Monolayers: A Comparative Study Using Hydrogenated and Partially Fluorinated Amphiphilic Derivatives of Mannitol. *Chem. Phys. Lipids* **2000**, *105* (1), 71–91.

(92) Langmuir, I. The Constitution and Fundamental Properties of Solids and Liquids. Ii. Liquids.1. *J. Am. Chem. Soc.* **1917**, *39* (9), 1848–1906.

(93) Harkins, W. D.; Feldman, A. Films. the Spreading of Liquids and the Spreading Coefficient. *J. Am. Chem. Soc.* **1922**, *44* (12), 2665–2685.

(94) P.Martin, M. S. *Langmuir-Blodgett Trough Operating Manual*, 6th ed.; Grunfeld, F., Ed.; Nima Technology Ltd: Coventry.

(95) Petty, M. C. *Langmuir-Blodgett Films: An Introduction.*; Decher, G., Ed.; Cambridge University Press, 1997; Vol. 9.

(96) Kaganer, V. M.; Loginov, E. B. Crystallization Phase Transitions and Phase Diagram of Langmuir Monolayers. *Phys. Rev. Lett.* **1993**, *71* (16), 2599–2602.

(97) Roldán-Carmona, C.; Giner-Casares, J. J.; Pérez-Morales, M.; Martín-Romero, M. T.; Camacho, L. Revisiting the Brewster Angle Microscopy: The Relevance of the Polar Headgroup. *Adv. Colloid Interface Sci.* **2012**, *173*, 12–22.

(98) Vollhardt, D.; Fainerman, V. B. Characterisation of Phase Transition in Adsorbed Monolayers at the Air/Water Interface. *Adv. Colloid Interface Sci.* **2010**, *154* (1), 1–19.

(99) Hénon, S.; Meunier, J. Microscope at the Brewster Angle: Direct Observation of First-order Phase Transitions in Monolayers. *Rev. Sci. Instrum.* **1991**, *62* (4), 936–939.

(100) Hönig, D.; Möbius, D. Reflectometry at the Brewster Angle and Brewster Angle Microscopy at the Air-Water Interface. *Thin Solid Films* **1992**, *210–211*, 64–68.

(101) Desbat, B.; Castano, S. Brewster Angle Microscopy and Imaging Ellipsometry. In *Encyclopedia of Biophysics*; Roberts, G. C. K., Ed.; Springer Berlin Heidelberg: Berlin, Heidelberg, 2013; pp 196–200.

(102) Vollhardt, D. Brewster Angle Microscopy: A Preferential Method for Mesoscopic Characterization of Monolayers at the Air/Water Interface. *Curr. Opin. Colloid Interface Sci.* **2014**, *19* (3), 183–197.

(103) Vollhardt, D. Effect of Interfacial Molecular Recognition of Non-Surface-Active Species on the Main Characteristics of Monolayers. *Adv. Colloid Interface Sci.* **2005**, *116* (1), 63–80.

(104) Bass, M.; DeCusatis, C.; Enoch, J.; Lakshminarayanan, V.; Li, G.; MacDonald, C.; Mahajan, V.; Van Stryland, E. *Handbook of Optics, Third Edition Volume I: Geometrical and Physical Optics, Polarized Light, Components and Instruments(Set)*; 2010.

(105) Garcia-Caurel, E.; Martino, A. De; Gaston, J.-P.; Yan, L. Application of Spectroscopic Ellipsometry and Mueller Ellipsometry to Optical Characterization. *Appl. Spectrosc.* **2013**, *67* (1), 1–21.

(106) Wasserman, S. R.; Tao, Y. T.; Whitesides, G. M. Structure and Reactivity of Alkylsiloxane Monolayers Formed by Reaction of Alkyltrichlorosilanes on Silicon Substrates. *Langmuir* **1989**, *5* (4), 1074–1087.

(107) Yakubovsky, D. I.; Arsenin, A. V; Stebunov, Y. V; Fedyanin, D. Y.; Volkov, V. S. Optical Constants and Structural Properties of Thin Gold Films. *Opt. Express* **2017**, *25* (21), 25574–25587.

(108) Simpson, G. J.; Sedin, D. L.; Rowlen, K. L. Surface Roughness by Contact versus Tapping Mode Atomic Force Microscopy. *Langmuir* **1999**, *15* (4), 1429–1434.

(109) *Langmuir-Blodgett Films*; Roberts, G., Ed.; Springer US: Boston, MA, 1990.

(110) Miller, D. M. R. *Novel Methods to Study Interfacial Layers, Volume 11*, 1st ed.; Elsevier, 2001.

(111) Kaganer, V. M.; Möhwald, H.; Dutta, P. Structure and Phase Transitions in Langmuir Monolayers. *Rev. Mod. Phys.* **1999**, *71* (3), 779–819.

(112) Kaganer, V. M.; Loginov, E. B. Symmetry and Phase Transitions in Langmuir Monolayers: The Landau Theory. *Phys. Rev. E* **1995**, *51* (3), 2237–2249.

(113) Kaganer, V. M.; Peterson, I. R.; Kenn, R. M.; Shih, M. C.; Durbin, M.; Dutta, P. Tilted Phases of Fatty Acid Monolayers. *J. Chem. Phys.* **1995**, *102* (23), 9412–9422.

(114) Tassler, S.; Pawlowska, D.; Janich, C.; Dobner, B.; Wölk, C.; Brezesinski, G. Lysine-Based Amino-Functionalized Lipids for Gene Transfection: The Influence of the Chain Composition on 2D Properties. *Phys. Chem. Chem. Phys.* **2018**, *20* (10), 6936–6944.

(115) Stefaniu, C.; Vilotijevic, I.; Santer, M.; Varón Silva, D.; Brezesinski, G.; Seeberger, P. H. Subgel Phase Structure in Monolayers of Glycosylphosphatidylinositol Glycolipids. *Angew. Chemie Int. Ed.* **2012**, *51* (51), 12874–12878.

(116) Ewen, B.; Strobl, G. R.; Richter, D. Phase Transitions in Crystals of Chain Molecules. Relation between Defect Structures and Molecular Motion in the Four Modifications of n-C33H68. *Faraday Discuss. Chem. Soc.* **1980**, *69* (0), 19–31.

(117) Muller, A. An X-Ray Investigation of Normal Paraffins Near Their Melting Points. *Proc. R. Soc. A Math. Phys. Eng. Sci.* **1932**, *138* (836), 514–530.

(118) Durbin, M. K.; Richter, A. G.; Yu, C.-J.; Kmetko, J.; Bai, J. M.; Dutta, P. Backbone Orientational Order in Fatty Acid Monolayers at the Air-Water Interface. *Phys. Rev. E* **1998**, *58* (6), 7686–7690.

(119) Gong, Z.; Kerr, D.; Hwang, H. L.; Henderson, J. M.; Suwatthee, T.; Slaw, B. R.; Cao, K. D.; Lin,

B.; Bu, W.; Lee, K. Y. C. Quantitative Analysis of Total Reflection X-Ray Fluorescence from Finely Layered Structures Using XeRay. *Rev. Sci. Instrum.* **2017**, *88* (3), 33112.

(120) Bu, W.; Hou, B.; Mihaylov, M.; Kuzmenko, I.; Lin, B.; Meron, M.; Soderholm, L.; Luo, G.; Schlossman, M. L. X-Ray Fluorescence from a Model Liquid/Liquid Solvent Extraction System. *J. Appl. Phys.* **2011**, *110* (10), 102214.

(121) Shapovalov, V. L.; Ryskin, M. E.; Konovalov, O. V; Hermelink, A.; Brezesinski, G. Elemental Analysis within the Electrical Double Layer Using Total Reflection X-Ray Fluorescence Technique. *J. Phys. Chem. B* **2007**, *111* (15), 3927–3934.

(122) Bu, W. Ion Distributions at Charged Aqueous Surfaces: Synchrotron X-Ray Scattering Studies, Iowa State University, Digital Repository: Ames, 2009.

(123) Laboratory, L. B. N. X-ray data booklet https://xdb.lbl.gov/ (accessed Dec 7, 2019).

(124) Nguyen, H. H.; Park, J.; Kang, S.; Kim, M. Surface Plasmon Resonance: A Versatile Technique for Biosensor Applications. *Sensors (Basel).* **2015**, *15* (5), 10481–10510.

(125) Šípová, H.; Homola, J. Surface Plasmon Resonance Sensing of Nucleic Acids: A Review. *Anal. Chim. Acta* **2013**, *773*, 9–23.

(126) Keith, P. L.; Heneriette, M.; Marie-Isabel, A. The Study of Biomolecular-Membrane Interactions Using Surface Plsamon Resonance Spectroscopyle. In *Membrane-active Peptides: Methods and Results on Structure and Function*; Castanho, M. A. R. B., Ed.; Internat'l University Line, 2010; p 114.

(127) Quideau, S.; Deffieux, D.; Douat-Casassus, C.; Pouységu, L. Plant Polyphenols: Chemical Properties, Biological Activities, and Synthesis. *Angew. Chemie Int. Ed.* **2011**, *50* (3), 586–621.

(128) Baxter, N. J.; Lilley, T. H.; Haslam, E.; Williamson, M. P. Multiple Interactions between Polyphenols and a Salivary Proline-Rich Protein Repeat Result in Complexation and Precipitation. *Biochemistry* **1997**, *36* (18), 5566–5577.

(129) Moehwald, H.; Brezesinski, G. From Langmuir Monolayers to Multilayer Films. *Langmuir* **2016**, *32* (41), 10445–10458.

(130) Czolkos, I.; Jesorka, A.; Orwar, O. Molecular Phospholipid Films on Solid Supports. *Soft Matter* **2011**, *7* (10), 4562–4576.

(131) Johann, R.; Vollhardt, D.; Möhwald, H. Study of the PH Dependence of Head Group Bonding in Arachidic Acid Monolayers by Polarization Modulation Infrared Reflection Absorption Spectroscopy. *Colloids Surfaces A Physicochem. Eng. Asp.* **2001**, *182* (1), 311–320.

(132) Fang, L.; Park, J. Y.; Ma, H.; Jen, A. K.-Y.; Salmeron, M. Atomic Force Microscopy Study of the Mechanical and Electrical Properties of Monolayer Films of Molecules with Aromatic End Groups. *Langmuir* **2007**, *23* (23), 11522–11525.

(133) Kundu, S.; Langevin, D. Fatty Acid Monolayer Dissociation and Collapse: Effect of PH and Cations. *Colloids Surfaces A Physicochem. Eng. Asp.* **2008**, *325* (1), 81–85.

(134) Peikert, M.; Chen, X.; Chi, L.; Brezesinski, G.; Janich, S.; Würthwein, E.-U.; Schäfer, H. J. Phase Behavior and Molecular Packing of Octadecyl Phenols and Their Methyl Ethers at the Air/Water Interface. *Langmuir* **2014**, *30* (20), 5780–5789.

(135) Holten-Andersen, N.; Mates, T. E.; Toprak, M. S.; Stucky, G. D.; Zok, F. W.; Waite, J. H. Metals and the Integrity of a Biological Coating: The Cuticle of Mussel Byssus. *Langmuir* **2009**, *25* (6), 3323–3326.

(136) Rahim, M. A.; Kristufek, S. L.; Pan, S.; Richardson, J. J.; Caruso, F. Phenolic Building Blocks for the Assembly of Functional Materials. *Angew. Chemie Int. Ed.* **2019**, *58* (7), 1904–1927.

(137) Wakasugi, K.; Iida, A.; Misaki, T.; Nishii, Y.; Tanabe, Y. Simple, Mild, and Practical Esterification, Thioesterification, and Amide Formation Utilizing p-Toluenesulfonyl Chloride and N-Methylimidazole. *Adv. Synth. Catal.* **2003**, *345* (11), 1209–1214.

(138) Smaby, J. M.; Kulkarni, V. S.; Momsen, M.; Brown, R. E. The Interfacial Elastic Packing Interactions of Galactosylceramides, Sphingomyelins, and Phosphatidylcholines. *Biophys. J.* **1996**,

70 (2), 868–877.

(139) Jacquemain, D.; Leveiller, F.; Weinbach, S. P.; Lahav, M.; Leiserowitz, L.; Kjaer, K.; Als-Nielsen, J. Crystal Structure of Self-Aggregates of Insoluble Aliphatic Amphiphilic Molecules at the Air-Water Interface. An x-Ray Synchrotron Study. *J. Am. Chem. Soc.* **1991**, *113* (20), 7684–7691.

(140) Vollhardt, D.; Brezesinski, G. Effect of Chirality on Monoacylglycerol Ester Monolayer Characteristics: 3-Monostearoyl-Sn-Glycerol. *Phys. Chem. Chem. Phys.* **2017**, *19* (10), 7009–7024.

(141) Vollhardt, D.; Stefaniu, C.; Brezesinski, G. Special Features of Monolayer Characteristics of N-Alkanoyl Substituted Threonine Amphiphiles. *Phys. Chem. Chem. Phys.* **2019**, *21* (1), 96–103.

(142) Jensen, T. R.; Kjaer, K. Structural Properties and Interactions of Thin Films at the Air-Liquid Interface Explored by Synchrotron X-Ray Scattering. In *Novel Methods to Study Interfacial Layers*; Möbius, D., Miller, R. B. T.-S. in I. S., Eds.; Elsevier, 2001; Vol. 11, pp 205–254.

(143) Böhm, C.; Leveiller, F.; Jacquemain, D.; Möhwald, H.; Kjaer, K.; Als-Nielsen, J.; Weissbuch, I.; Leiserowitz, L. Packing Characteristics of Crystalline Monolayers of Fatty Acid Salts, at the Air-Solution Interface, Studied by Grazing Incidence X-Ray Diffraction. *Langmuir* **1994**, *10* (3), 830–836.

(144) Yue, X.; Dobner, B.; Iimura, K.; Kato, T.; Möhwald, H.; Brezesinski, G. Weak First-Order Tilting Transition in Monolayers of Mono- and Bipolar Docosanol Derivatives. *J. Phys. Chem. B* **2006**, *110* (44), 22237–22244.

(145) Pascher, I.; Sundell, S. Molecular Arrangements in Sphingolipids. The Crystal Structure of Cerebroside. *Chem. Phys. Lipids* **1977**, *20* (3), 175–191.

(146) Stefaniu, C.; Vilotijevic, I.; Brezesinski, G.; Seeberger, P. H.; Varón Silva, D. A Comparative Structural Study in Monolayers of GPI Fragments and Their Binary Mixtures. *Phys. Chem. Chem. Phys.* **2014**, *16* (20), 9259–9265.

(147) Dwibedy, P.; R. Dey, G.; B. Naik, D.; Kishore, K.; N. Moorthy, P. Pulse Radiolysis Studies on

Redox Reactions of Gallic Acid: One Electron Oxidation of Gallic Acid by Gallic Acid–OH Adduct. *Phys. Chem. Chem. Phys.* **1999**, *1* (8), 1915–1918.

(148) Eslami, A. C.; Pasanphan, W.; Wagner, B. A.; Buettner, G. R. Free Radicals Produced by the Oxidation of Gallic Acid: An Electron Paramagnetic Resonance Study. *Chem. Cent. J.* **2010**, *4*, 15.

(149) Huguenin, J.; Ould Saad Hamady, S.; Bourson, P. Monitoring Deprotonation of Gallic Acid by Raman Spectroscopy. *J. Raman Spectrosc.* **2015**, *46* (11), 1062–1066.

(150) Kumar, J. K.; Oliver, J. S. Proximity Effects in Monolayer Films: Kinetic Analysis of Amide Bond Formation at the Air−Water Interface Using 1H NMR Spectroscopy. *J. Am. Chem. Soc.* **2002**, *124* (38), 11307–11314.

(151) Seul, M.; Andelman, D. Domain Shapes and Patterns: The Phenomenology of Modulated Phases. *Science (80-.).* **1995**, *267* (5197), 476–483.

(152) McConnell, H. M. Theory of Hexagonal and Stripe Phases in Monolayers. *Proc. Natl. Acad. Sci. U. S. A.* **1989**, *86* (10), 3452–3455.

(153) Melzer, V.; Vollhardt, D.; Weidemann, G.; Brezesinski, G.; Wagner, R.; Möhwald, H. Structure Formation and Phase Transitions in Gibbs and Langmuir Monolayers of Amphiphilic Acid Amides. *Phys. Rev. E* **1998**, *57* (1), 901–907.

(154) Hossain, M. M.; Iimura, K.; Kato, T. Temperature and Compression Rate Independent Domain Shape in Langmuir Monolayers of Di-n-Dodecyl Hydrogen Phosphate at the Air–water Interface. *J. Colloid Interface Sci.* **2008**, *319* (1), 295–301.

(155) Flores, A.; Ize, P.; Ramos, S.; Castillo, R. The Dioctadecylamine Monolayer: Textures, Phase Transitions, and Dendritic Growth. *J. Chem. Phys.* **2003**, *119* (11), 5644–5653.

(156) Hoffmann, F.; Stine, K. J.; Hühnerfuss, H. Appearance and Disappearance of Dendritic and Chiral Patterns in Domains of Langmuir Monolayers Observed with Brewster Angle Microscopy. *J. Phys. Chem. B* **2005**, *109* (1), 240–252.

(157) Davies, J. T.; Rideal, E. K. Properties of Monolayers. In *Interfacial Phenomena*; Elsevier, 1961; pp 217–281.

(158) Vollhardt, D.; Emrich, G.; Siegel, S.; Rudert, R. Phase Transition in Monolayers of Straight Chain and 2-Methyl Branched Alcohols at the Air−Water Interface. *Langmuir* **2002**, *18* (17), 6571–6577.

(159) Fainerman, V. B.; Vollhardt, D.; Johann, R. Arachidic Acid Monolayers at High PH of the Aqueous Subphase: Studies of Counterion Bonding. *Langmuir* **2000**, *16* (20), 7731–7736.

(160) Johann, R.; Vollhardt, D. Texture Features of Long-Chain Fatty Acid Monolayers at High PH of the Aqueous Subphase. *Mater. Sci. Eng. C* **1999**, *8–9*, 35–42.

(161) Ghaicha, L.; Chattopadhyay, A. K.; Tajmir-Riahi, H. A. Behavior of Stearic Acid Monolayers in Presence of Concentrated Ammonium Nitrate Solution Substrate. *Langmuir* **1991**, *7* (10), 2007–2009.

(162) Çakıroğlu, B.; Özacar, M. Tannic Acid Modified Electrochemical Biosensor for Glucose Sensing Based on Direct Electrochemistry. *Electroanalysis* **2017**, *29* (12), 2719–2726.

(163) Xu, L. Q.; Pranantyo, D.; Ng, Y. X.; Teo, S. L.-M.; Neoh, K.-G.; Kang, E.-T.; Fu, G. D. Antifouling Coatings of Catecholamine Copolymers on Stainless Steel. *Ind. Eng. Chem. Res.* **2015**, *54* (22), 5959–5967.

(164) Khedimallah, N.; Zazoua, A.; Sbartai, A.; Jaffrezic-Renault, N. A High Sensitivity Impedimetric Biosensor Using the Tannin From Quercusmacrolepis as Biorecognition Element for Heavy Metals Detection. *IEEE Trans. Nanobioscience* **2015**, *14* (7), 694–699.

(165) Chen, Y.; Meng, J.; Zhu, Z.; Zhang, F.; Wang, L.; Gu, Z.; Wang, S. Bio-Inspired Underwater Super Oil-Repellent Coatings for Anti-Oil Pollution. *Langmuir* **2018**, *34* (21), 6063–6069.

(166) Subramanian, N.; Schmidt, R.; Wood-Adams, P. M.; DeWolf, C. E. Space-Filling Trialkoxysilane: Synthesis and Self-Assembly into Low-Density Monolayers. *Langmuir* **2010**, *26* (24), 18628–18630.

(167) Lahann, J.; Mitragotri, S.; Tran, T.-N.; Kaido, H.; Sundaram, J.; Choi, I. S.; Hoffer, S.; Somorjai, G. A.; Langer, R. A Reversibly Switching Surface. *Science (80-.).* **2003**, *299* (5605), 371–374.

(168) Moehwald, H.; Brezesinski, G. From Langmuir Monolayers to Multilayer Films. *Langmuir* **2016**, *32* (41), 10445–10458.

(169) Vollhardt, D.; Fainerman, V. B. Progress in Characterization of Langmuir Monolayers by Consideration of Compressibility. *Adv. Colloid Interface Sci.* **2006**, *127* (2), 83–97.

(170) Datta, A.; Kmetko, J.; Richter, A. G.; Yu, C.-J.; Dutta, P.; Chung, K.-S.; Bai, J.-M. Effect of Headgroup Dissociation on the Structure of Langmuir Monolayers. *Langmuir* **2000**, *16* (3), 1239–1242.

(171) Boehm, C.; Leveiller, F.; Jacquemain, D.; Moehwald, H.; Kjaer, K.; Als-Nielsen, J.; Weissbuch, I.; Leiserowitz, L. Packing Characteristics of Crystalline Monolayers of Fatty Acid Salts, at the Air-Solution Interface, Studied by Grazing Incidence X-Ray Diffraction. *Langmuir* **1994**, *10* (3), 830–836.

(172) Miclette Lamarche, R.; DeWolf, C. Strong Headgroup Interactions Drive Highly Directional Growth and Unusual Phase Co-Existence in Self-Assembled Phenolic Films. *ACS Appl. Mater. Interfaces* **2019**, *11* (48), 45354–45363.

(173) Matharu, Z.; Bandodkar, A. J.; Gupta, V.; Malhotra, B. D. Fundamentals and Application of Ordered Molecular Assemblies to Affinity Biosensing. *Chem. Soc. Rev.* **2012**, *41* (3), 1363–1402.

(174) Yuan, M.; Zhan, S.; Zhou, X.; Liu, Y.; Feng, L.; Lin, Y.; Zhang, Z.; Hu, J. A Method for Removing Self-Assembled Monolayers on Gold. *Langmuir* **2008**, *24* (16), 8707–8710.

(175) Meister, A.; Weygand, M. J.; Brezesinski, G.; Kerth, A.; Drescher, S.; Dobner, B.; Blume, A. Evidence for a Reverse U-Shaped Conformation of Single-Chain Bolaamphiphiles at the Air−Water Interface. *Langmuir* **2007**, *23* (11), 6063–6069.

(176) Flores, A.; Ize, P.; Ramos, S.; Castillo, R. The Dioctadecylamine Monolayer: Textures, Phase Transitions, and Dendritic Growth. *J. Chem. Phys.* **2003**, *119* (11), 5644–5653.

(177) Ueno, M.; Kawanabe, M.; Meguro, K. Monolayer Properties of Some α, ω-Diols. *J. Colloid Interface Sci.* **1975**, *51* (1), 32–35.

(178) Zhang, L.; Jiang, S.; Liu, M. Configuration and Photochemical Reaction of a Bolaamphiphilic Diacid with a Diazo Resin in Monolayers and Langmuir–Blodgett Films. *J. Colloid Interface Sci.* **2003**, *261* (2), 417–422.

(179) Ducharme, D.; Max, J. J.; Salesse, C.; Leblanc, R. M. Ellipsometric Study of the Physical States of Phosphatidylcholines at the Air-Water Interface. *J. Phys. Chem.* **1990**, *94* (5), 1925–1932.

(180) Riddick, J.A., Bunger, W.B. and Sakano, T. K. *Organic Solvents: Physical Properties and Methods of Purification.*, 4th ed.; John Wiley and Sons: New York, 1986.

(181) Banerjee, R.; Sanyal, M. K.; Bera, M. K.; Gibaud, A.; Lin, B.; Meron, M. Reversible Monolayer-to-Crystalline Phase Transition in Amphiphilic Silsesquioxane at the Air-Water Interface. *Sci. Rep.* **2015**, *5*, 8497.

(182) Behyan, S.; Gritzalis, D.; Schmidt, R.; Kebede, E.; Cuccia, L. A.; DeWolf, C. Structural Organization and Phase Behaviour of Meta-Substituted Dioctadecylaminobenzoquinones at the Air/Water Interface. *Phys. Chem. Chem. Phys.* **2019**, *21* (5), 2345–2350.

(183) Allara, D. L.; Atre, S. V; Elliger, C. A.; Snyder, R. G. The Formation of a Crystalline Monolayer of Folded Molecules by Solution Self-Assembly of Alpha,Omega-Alkanedioic Acids on Silver. *J. Am. Chem. Soc.* **1991**, *113* (5), 1852–1854.

(184) Jacquemet, A.; Terme, N.; Benvegnu, T.; Vié, V.; Lemiègre, L. Collapsed Bipolar Glycolipids at the Air/Water Interface: Effect of the Stereochemistry on the Stretched/Bent Conformations. *J. Colloid Interface Sci.* **2013**, *412*, 72–81.

(185) Chen, P.; Gao, P.; Liu, M. Parallel Aligned Nanostripe Arrays in the Spreading Film of a Bolaamphiphile at the Air/Water Interface. *Colloids Surfaces A Physicochem. Eng. Asp.* **2006**, *284–285*, 140–146.

(186) Weissbuch, I.; Guo, S.; Edgar, R.; Cohen, S.; Howes, P.; Kjaer, K.; Als-Nielsen, J.; Lahav, M.;

Leiserowitz, L. Oriented Crystalline Thin Films of Tetracosanedioic Acid and Its Metal Salts at the Air–Aqueous Solution Interface. *Adv. Mater.* **1998**, *10* (2), 117–121.

(187) Chi, L. F.; Jacobi, S.; Anczykowski, B.; Overs, M.; Schäfer, H.-J.; Fuchs, H. Supermolecular Periodic Structures in Monolayers. *Adv. Mater.* **2000**, *12* (1), 25–30.

(188) Liu, X.; Wang, T.; Liu, M. Interfacial Assembly of a Series of Cinnamoyl-Containing Bolaamphiphiles: Spacer-Controlled Packing, Photochemistry, and Odd–Even Effect. *Langmuir* **2012**, *28* (7), 3474–3482.

(189) Perron, N. R.; Brumaghim, J. L. A Review of the Antioxidant Mechanisms of Polyphenol Compounds Related to Iron Binding. *Cell Biochem. Biophys.* **2009**, *53* (2), 75–100.

(190) Miclette Lamarche, R.; DeWolf, C. E. ω-Thiolation of Phenolic Surfactants Enables Controlled Conversion between Extended, Bolaform and Multilayer Conformations. *Unpubl. Work*.

(191) Prodan, A.; Brand, H.; Imangaliyev, S.; Tsivtsivadze, E.; van der Weijden, F.; de Jong, A.; Paauw, A.; Crielaard, W.; Keijser, B.; Veerman, E. A Study of the Variation in the Salivary Peptide Profiles of Young Healthy Adults Acquired Using MALDI-TOF MS. *PLoS One* **2016**, *11* (6), 1–15.

(192) Rajasingam, A.; Schmidt, R.; Woo, S.; DeWolf, C.; Forgione, P. Efficient Preparation of Novel Phenolic Surfactants for Self-Assembled Monolayers. *Synth. Commun.* **2014**, *44* (8), 1066–1075.

(193) Bu, W.; Mihaylov, M.; Amoanu, D.; Lin, B.; Meron, M.; Kuzmenko, I.; Soderholm, L.; Schlossman, M. L. X-Ray Studies of Interfacial Strontium–Extractant Complexes in a Model Solvent Extraction System. *J. Phys. Chem. B* **2014**, *118* (43), 12486–12500.

(194) Schwartz, D. K. Langmuir-Blodgett Film Structure. *Surf. Sci. Rep.* **1997**, *27* (7), 245–334.

(195) Hobson, R. J.; Ladd, M. F. C.; Povey, D. C. Substituted Phenols as Ligands III: Crystal and Molecular Structure of Bis(4-Formyl-2-Methoxyphenolato)Bis(Pyridine)Copper(II) Monohydrate. *J. Cryst. Mol. Struct.* **1973**, *3* (6), 377–388.

(196) Masoud, M. S.; Hagagg, S. S.; Ali, A. E.; Nasr, N. M. Synthesis and Spectroscopic Characterization

of Gallic Acid and Some of Its Azo Complexes. *J. Mol. Struct.* **2012**, *1014*, 17–25.

(197) Lorenz, C. D.; Travesset, A. Atomistic Simulations of Langmuir Monolayer Collapse. *Langmuir* **2006**, *22* (24), 10016–10024.

(198) Huo, Q.; Russev, S.; Hasegawa, T.; Nishijo, J.; Umemura, J.; Puccetti, G.; Russell, K. C.; Leblanc, R. M. A Langmuir Monolayer with a Nontraditional Molecular Architecture. *J. Am. Chem. Soc.* **2000**, *122* (33), 7890–7897.

(199) Wang, W.; Zhang, H.; Feng, S.; San Emeterio, J.; Mallapragada, S.; Vaknin, D. Iron Ion and Iron Hydroxide Adsorption to Charge-Neutral Phosphatidylcholine Templates. *Langmuir* **2016**, *32* (30), 7664–7670.

(200) Giner-Casares, J. J.; Brezesinski, G.; Möhwald, H.; Landsmann, S.; Polarz, S. Polyoxometalate Surfactants as Unique Molecules for Interfacial Self-Assembly. *J. Phys. Chem. Lett.* **2012**, *3* (3), 322–326.

(201) Li, S.; Du, L.; Tsona, N. T.; Wang, W. The Interaction of Trace Heavy Metal with Lipid Monolayer in the Sea Surface Microlayer. *Chemosphere* **2018**, *196*, 323–330.

(202) Severino, J. F.; Goodman, B. A.; Reichenauer, T. G.; Pirker, K. F. Is There a Redox Reaction between Cu(II) and Gallic Acid? *Free Radic. Res.* **2011**, *45* (2), 123–132.

(203) Kakinoki, S.; Hirano, Y.; Oka, M. On the Stability of Polyproline-I and II Structures of Proline Oligopeptides. *Polym. Bull.* **2005**, *53* (2), 109–115.

(204) Ruggiero, M. T.; Sibik, J.; Orlando, R.; Zeitler, J. A.; Korter, T. M. Measuring the Elasticity of Poly-L-Proline Helices with Terahertz Spectroscopy. *Angew. Chemie* **2016**, *128* (24), 6991–6995.

(205) He, H.; Huang, Y.; Zhang, Q.; Wang, J.-R.; Mei, X. Zwitterionic Cocrystals of Flavonoids and Proline: Solid-State Characterization, Pharmaceutical Properties, and Pharmacokinetic Performance. *Cryst. Growth Des.* **2016**, *16* (4), 2348–2356.

(206) Takeda, K.; Andoh, Y.; Shinoda, W.; Okazaki, S. Structure of Hydrated Crystal (Lc), Tilted Gel

(Lβ′), and Liquid Crystal (Lα) Phases of Linear Alkylbenzene Sulfonate (LAS) Studied by X-Ray Diffraction and Molecular Dynamics Simulation. *Langmuir* **2019**, *35* (27), 9011–9019.

(207) Trommeshauser, D.; Galla, H. J. Interaction of a Basic Amphipathic Peptide from the Carboxyterminal Part of the HIV Envelope Protein Gp41 with Negatively Charged Lipid Surfaces. *Chem. Phys. Lipids* **1998**, *94* (1), 81—96.

(208) Hädicke, A.; Schwieger, C.; Blume, A. Cospreading of Anionic Phospholipids with Peptides of the Structure (KX)4K at the Air–Water Interface: Influence of Lipid Headgroup Structure and Hydrophobicity of the Peptide on Monolayer Behavior. *Langmuir* **2017**, *33* (43), 12204–12217.

(209) Zhang, L.; Liu, Y.; Wang, Y. Deprotonation Mechanism of Methyl Gallate: UV Spectroscopic and Computational Studies. *Int. J. Mol. Sci.* **2018**, *19* (10).

(210) Hall, R. A.; Hayes, D.; Thistlethwaite, P. J.; Grieser, F. Characterization of Air—water Monolayers Using Pressure—area Isotherms in Conjunction with UV-Visible Spectroscopic Methods: The Effect of PH on the Ionization of 4-Octadecyloxy-1-Naphthoic Acid and 4-Heptadecyl-7-Hydroxycoumarin Monolayers. *Colloids and Surfaces* **1991**, *56*, 339–356.

(211) Conry, R. R. Copper: Inorganic & Coordination Chemistry Based in Part on the Article Copper: Inorganic & Coordination Chemistry by Rebecca R. Conry & Kenneth D. Karlin Which Appeared in the Encyclopedia of Inorganic Chemistry, First Edition. In *Encyclopedia of Inorganic Chemistry*; American Cancer Society, 2006.

(212) Grundl, T.; Delwiche, J. Kinetics of Ferric Oxyhydroxide Precipitation. *J. Contam. Hydrol.* **1993**, *14* (1), 71–87.

Appendix

Appendix Table 1. Fitted peak positions in Qxy and Qz and corresponding full width at half maximum (FWHM). TW denotes a peak that was too weak to properly fit accurately in either position and/or width. DNS denotes systems for which a low Qxy scan was not performed. For the pH 11 subphase, the new set of peaks appears at pH 11 already with 10 minutes relaxation time but were too weak to fit and are therefore not listed in the table. After 60 minutes relaxation only the new set of peaks are visible. The out-of-plane peak seen for ODG on subphases from water to pH 11 could also be fit as two peaks yielding an intermediate tilt, in between NN and NNN, but the difference in tilt azimuth was minimal (120° vs 118°).

Water									
π (mN/m)		$Q_{xy}1$ ($Å^{-1}$)	Q_z1 ($Å^{-1}$)	$Q_{xy}2$ ($Å^{-1}$)	Q_z2 ($Å^{-1}$)	$Q_{xy}3$ ($Å^{-1}$)	Q_z3 ($Å^{-1}$)	$Q_{xy}4$ ($Å^{-1}$)	Q_z4 ($Å^{-1}$)
5	Position	0.963	0	1.279	0.783	1.638	0	1.863	0
	FWHM	0.025	TW	0.058	0.288	0.026	0.288	0.053	1.113
20	Position	0.965	0	1.284	0.767	1.642	0	1.873	0
	FWHM	0.034	TW	0.059	0.309	0.031	0.309	0.055	0.995
40	Position	DNS	DNS	1.289	0.759	1.652	0	1.877	0
	FWHM	DNS	DNS	0.058	0.290	0.026	0.290	0.082	1.002
pH 9									
		$Q_{xy}1$	Q_z1	$Q_{xy}2$	Q_z2	$Q_{xy}3$	Q_z3	$Q_{xy}4$	Q_z4
5	Position	0.962	0	1.279	0.785	1.638	0	1.862	0
	FWHM	0.024	TW	0.059	0.337	0.024	0.337	0.044	1.236
20	Position	0.960	0	1.281	0.784	1.643	0	1.868	0
	FWHM	0.022	TW	0.061	0.299	0.031	0.299	0.037	0.985

pH 10									
		$Q_{xy}1$	Q_z1	$Q_{xy}2$	Q_z2	$Q_{xy}3$	Q_z3	$Q_{xy}4$	Q_z4
5	Position	0.962	0	1.282	0.785	1.637	0	1.863	0
	FWHM	0.236	TW	0.062	0.318	0.028	1.282	0.041	1.447
20	Position	0.962	0	1.286	0.768	1.646	0	1.872	0
	FWHM	0.041	TW	0.071	0.277	0.040	0.277	0.055	0.930
pH 11, 10 minutes relaxation time									
		$Q_{xy}1$	Q_z1	$Q_{xy}2$	Q_z2	$Q_{xy}3$	Q_z3	$Q_{xy}4$	Q_z4
1	Position	TW	TW	1.280	0.812	1.642	0	TW	TW
	FWHM	TW	TW	0.059	0.3	0.023	0.3	TW	TW
20	Position	DNS	DNS	1.288	0.700	1.647	0	1.870	TW
	FWHM	DNS	DNS	0.040	0.3	0.048	0.3	0.040	TW
pH 11, 60 minutes relaxation time									
		$Q_{xy}1$	Q_z1	$Q_{xy}2$	Q_z2	-	-	-	-
5	Position	1.348	0.726	1.461	0	-	-	-	-
	FWHM	0.180	0.382	0.080	0.383	-	-	-	-

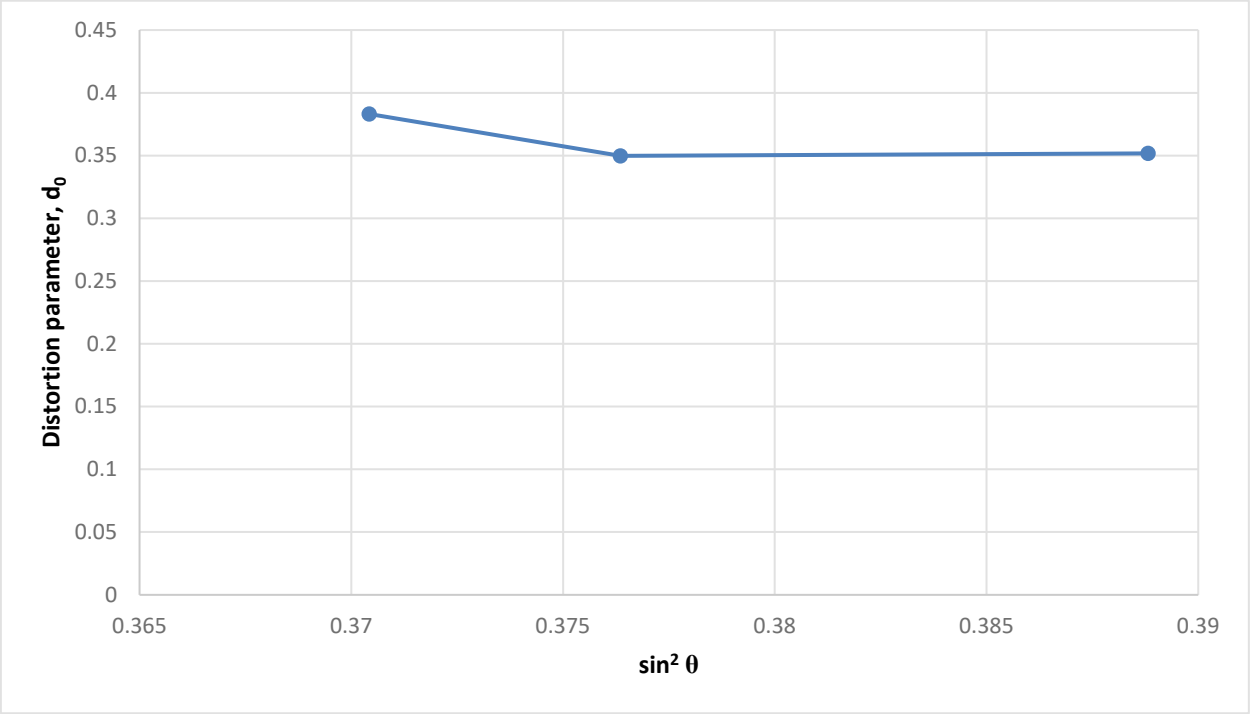

Appendix Figure 1. Distortion value derived from GIXD analysis as a function of $\sin^2$ of the tilt angle for ODG on a water subphase

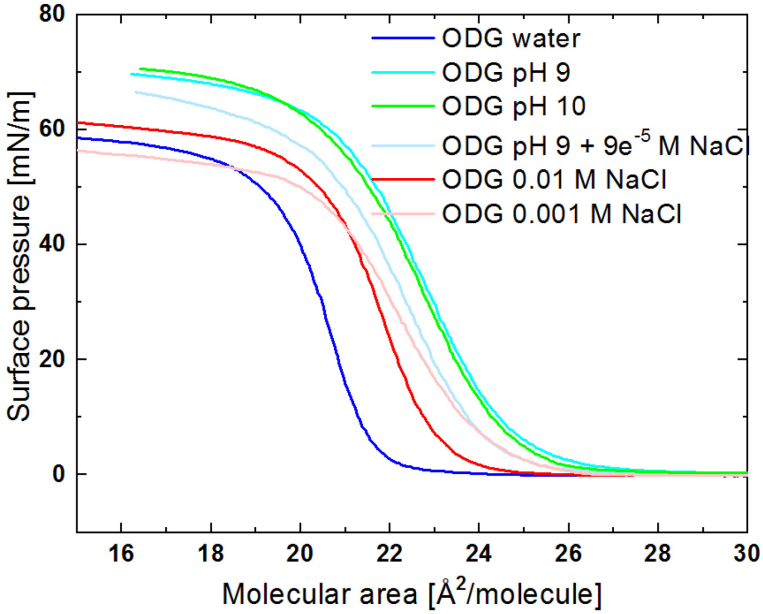

Appendix Figure 2. Surface pressure-molecular area isotherms of ODG as a function of subphase, NaCl was added to increase the ionic strenght of the subphase to be equivalent to subphase of higher pH.

Appendix Table 2. Fitted peak positions in Qxy and Qz and corresponding full width at half maximum (FWHM). TW denotes a peak that was too weak to properly fit accurately in either position and width. The out-of-plane peak seen for ODG SH on subphases water and pH 10 could also be fit as two peaks yielding an intermediate tilt, in between NN and NNN, but the difference in tilt azimuth was minimal (120° vs 118°).

Water									
π (mN/m)		Qxy1 (Å-1)	Qz1 (Å-1)	Qxy2 (Å-1)	Qz2 (Å-1)	Qxy3 (Å-1)	Qz3 (Å-1)	Qxy4 (Å-1)	Qz4 (Å-1)
1	Position	-	-	1.28723	0.78753	1.6476	0	1.86447	0
	Width	-	-	0.05166	0.26929	0.01888	0.26929	0.01824	TW
20	Position	-	-	1.28594	0.78509	1.65153	0	1.8715	0
	Width	-	-	0.05188	0.29212	0.0252	0.29212	0.03387	0.90995
pH 10									
		Qxy1	Qz1	Qxy2	Qz2	Qxy3	Qz3	Qxy4	Qz4
5	Position	0.96327	TW	1.28596	0.7976	1.65126	0	1.86838	0
	Width	0.00907	TW	0.06423	0.3	0.03823	0.3	0.11275	TW
15	Position	1.50249	0.34062	1.51362	0	-	-	-	-
	Width	0.10056	0.35989	0.08771	0.35989	-	-	-	-
pH 11, 10 minutes relaxation time									
		Qxy1	Qz1	-	-	-	-	-	-
1	Position	none	None	-	-	-	-	-	-
	Width	none	None	-	-	-	-	-	-
10	Position	None	None	-	-	-	-	-	-
	Width	None	none	-	-	-	-	-	-
15	Position	1.48199	0	-	-	-	-	-	-
	Width	0.11939	0.611	-	-	-	-	-	-

Appendix Table 3. Film thickness pre- and post-ethanol wash determined by ellipsometric measurements of ODG SH deposited onto gold by LB from the air-water interface.							
		Deposition pressure (mN/m)					
subphase		5	10	15	20	25	35
water	Pre-wash	1.11 ± 0.17	1.42 ± 0.42	1.31 ± 0.64	-	3.09 ± 0.49	3.20 ± 0.08
	Post-wash	1.08 ± 0.11	1.06 ± 0.32	1.20 ± 0.48	-	2.27 ± 0.36	2.25 ± 0.08
PH 10	Pre-wash	1.04 ± 0.11	2.37 ± 0.50	-	2.68 ± 0.50	-	-
	Post-wash	0.89 ± 0.15	1.72 ± 0.59	-	2.2 ± 0.45	-	-
pH 11	Pre-wash	0.95 ± 0.60	1.27 ± 0.02	1.51 ± 0.21	1.52 ± 0.10	1.69 ± 0.13	-
	Post-wash	1.00 ± 0.46	1.07 ± 0.19	1.41 ± 0.16	1.40 ± 0.11	1.53 ± 0.21	-

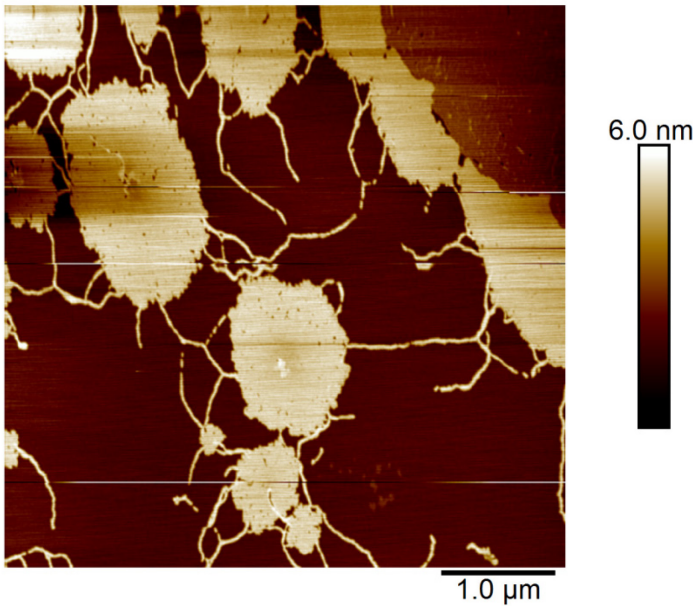

Appendix Figure 3. AFM image of ODG SH deposited onto mica from a pH 10 subphase at a surface pressure of 16 mN/m after 10 minutes relaxation time.

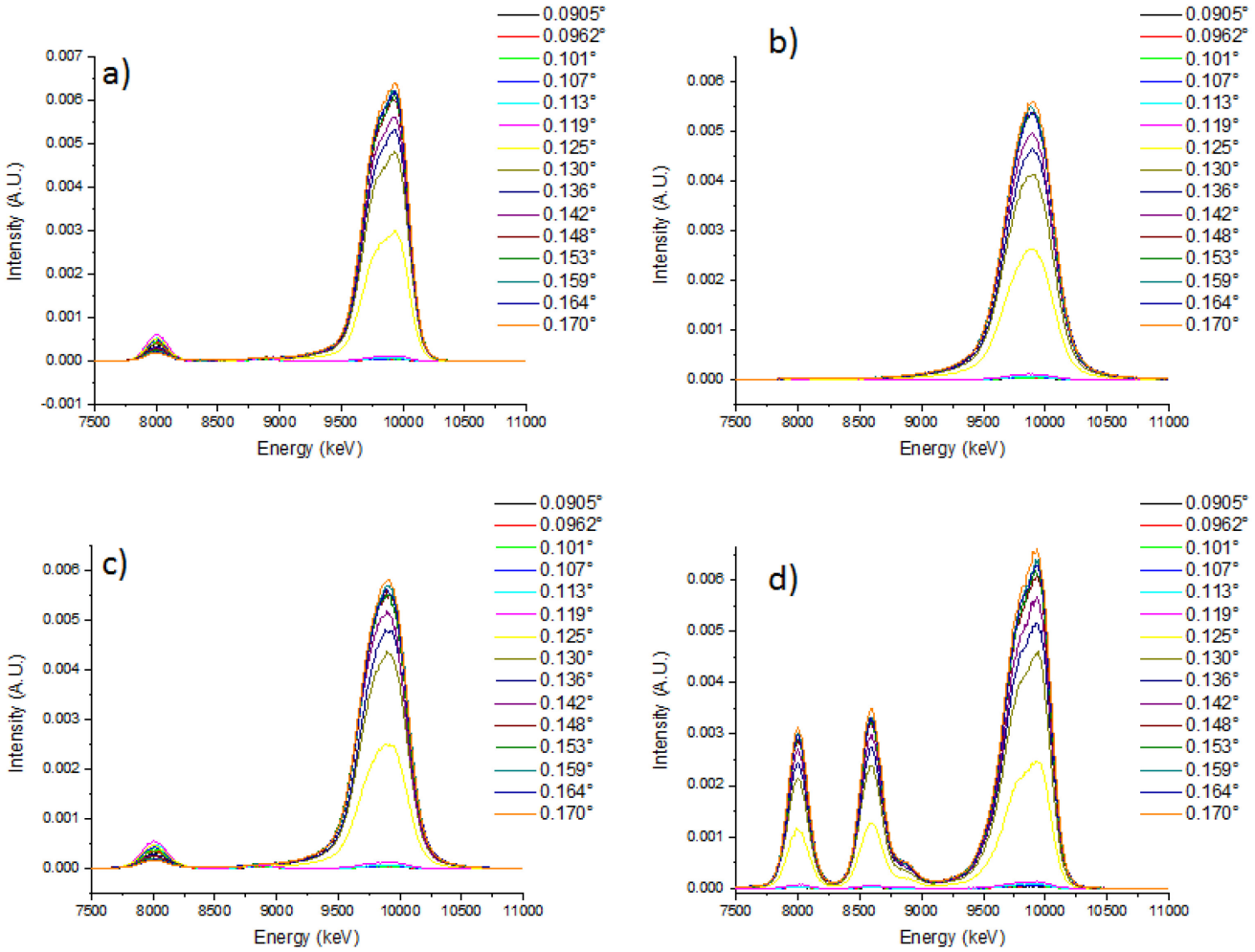

Appendix Figure 4. X-ray fluorescence near total reflection raw data. The $K\alpha_1$ and $K\alpha_2$ (K-L_3 and K-L_2 in IUPAC notation) are too close to distinguish. Cu lines are $K\alpha_1$= 8 047.78 keV, $K\alpha_2$= 8 027.83 keV, (in addition the $K\beta_1$ (K-M_3) line for Cu was visible but not used (at 8 905.29 keV) Zn lines are $K\alpha_1$= 8 638.86 KeV, $K\alpha_2$= 8 615.78 KeV). Direct beam at 10 000 keV. LDG SH to metal ratio of 1:10 (along with subphase metal concentration), pressure of 2 mN/m, a) Cu ($2.48e^{-6}$ M), b) Zn ($1.66e^{-6}$ M), c) Cu and Zn ($2.48e^{-6}$ M and $2.42e^{-6}$ M). d) Reference used with metal concentration of 0.02 M of $CuCl_2$ and $ZnCl_2$.

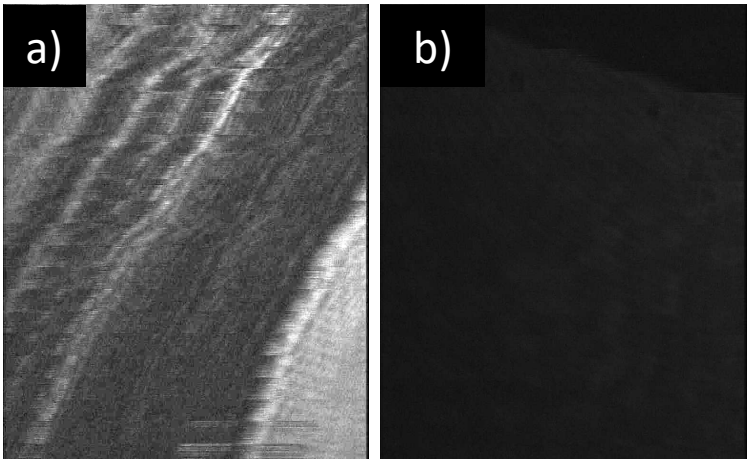

Appendix Figure 5. Brewster angle microscopy images of a) LDG SH on 1:10 subphase of copper, before any compression is applied (image quality is low due to the high movement of the domains at the surface of water). b) LDG SH on 1:1 subphase of copper at the critical area

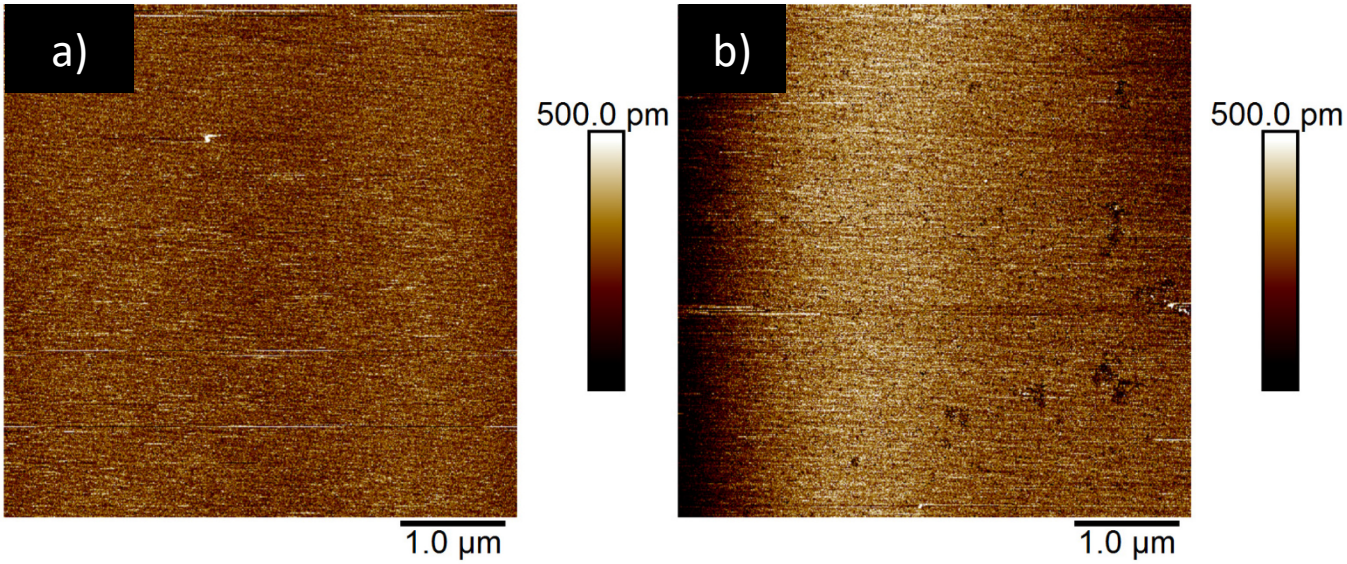

Appendix Figure 6. Atomic force microscopy images of LDG SH monolayers deposited by Langmuir-Blodgettry onto mica substrates at pressure of 5 mN/m. a) ultrapure water subphase, b) lipid:ZnCl2 ratio of 10.

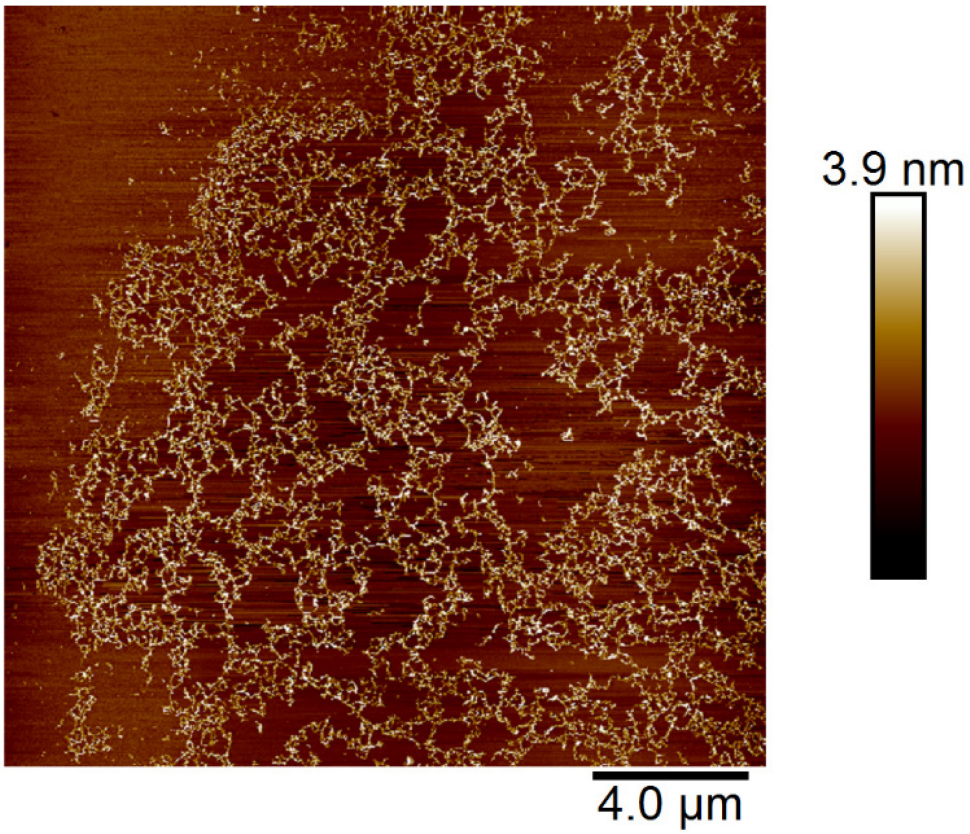

Appendix Figure 7. Atomic force microscopy images of ODG SH monolayers deposited by Langmuir-Blodgettry onto mica substrates at pressure of 5 mN/m, ODG SH:CuCl2 ratio of 1:10.

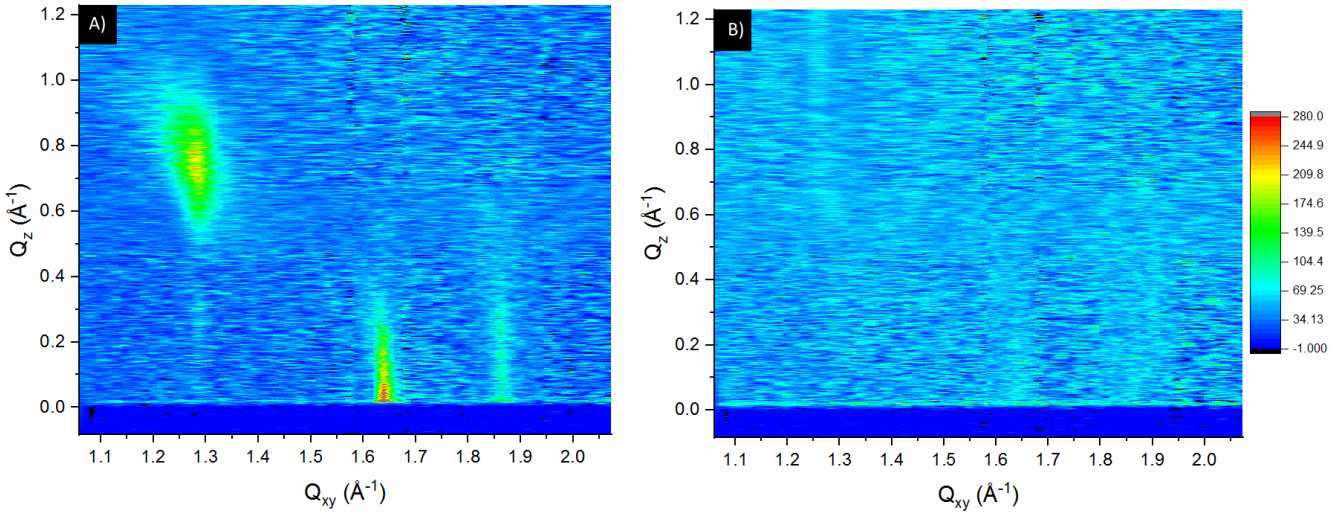

Appendix Figure 8. GIXD contour plots of the diffracted X-ray intensity of ODG as a function of the in-plane (Qxy) and out-of-plane (Qz) vector components over subphase with lipid:metal ratio of 1:10 at pressure 5 mN/m a) $ZnCl_2$, b) $CuCl_2$

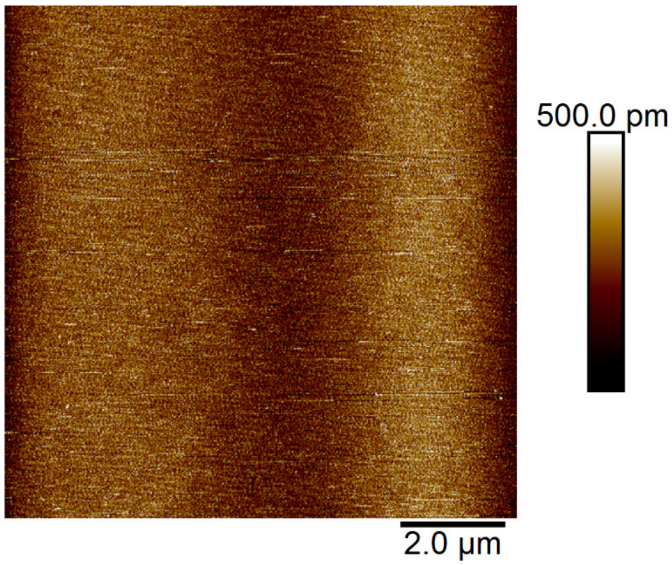

Appendix Figure 9. Atomic force microscopy images of LDG SH monolayers deposited by Langmuir-Blodgettry onto mica substrates at pressure of 5 mN/m, LDG SH:$ZnCl_2$ ratio of 1:10

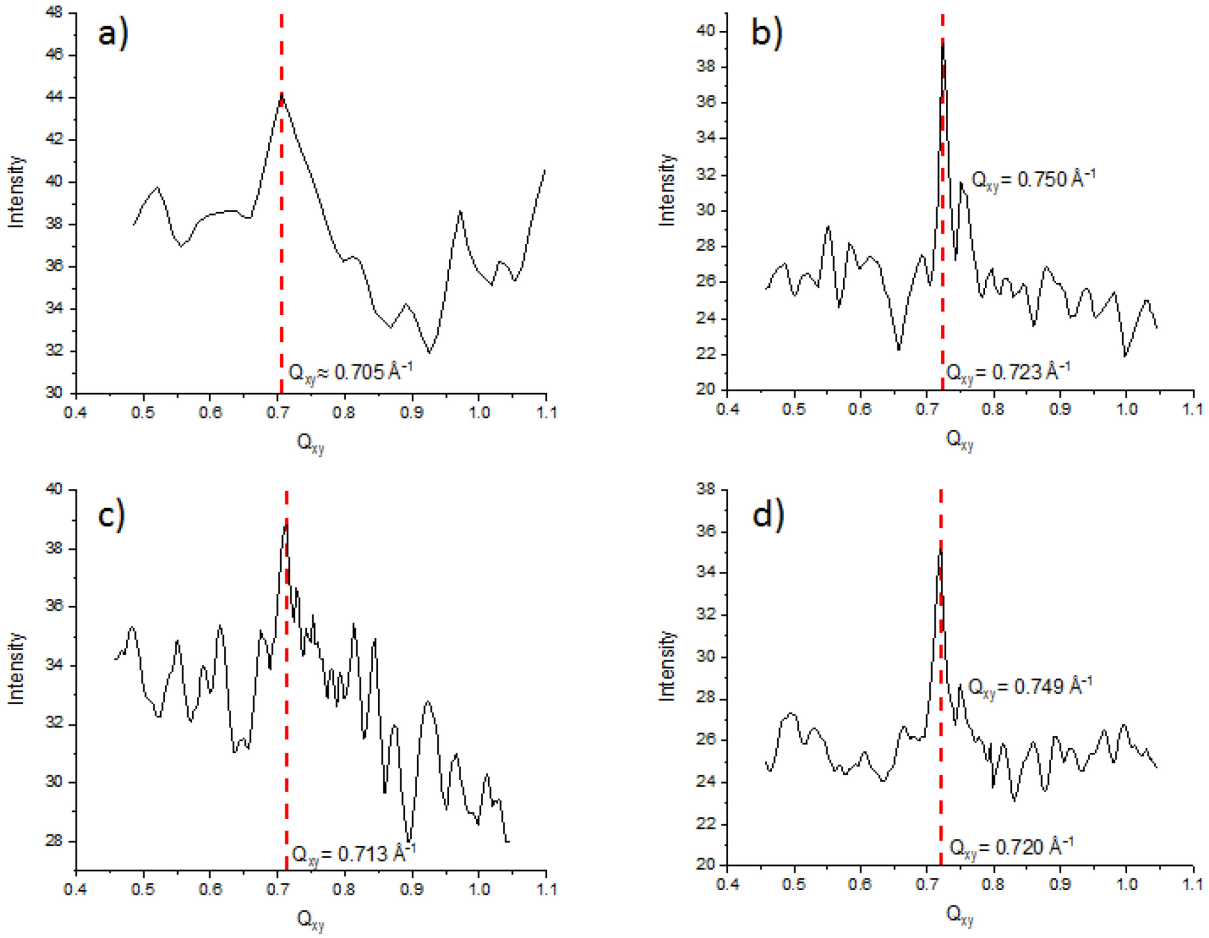

Appendix Figure 10. Integrated in-plane GIXD intensity of monolayer on a 1:1 lipid:poly-L-proline ratio: a) LDG SH, 5 mN/m (only rough scan available), b) LDG SH, 20 mN/m, c) ODG SH, 5 mN/m, d) ODG SG, 15 mN/m

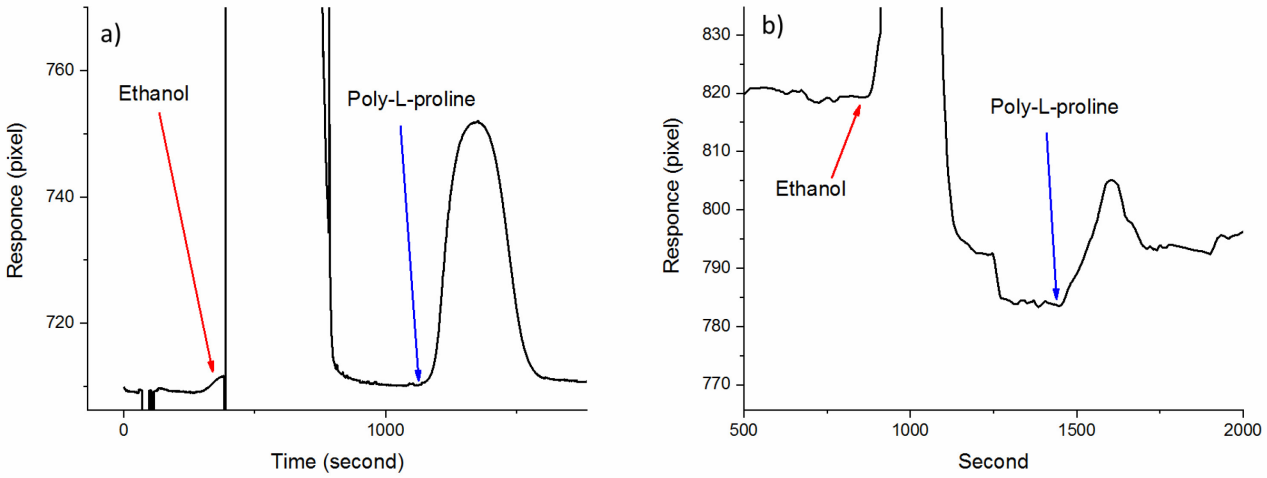

Appendix figure 11. SPR response of deposited film onto gold, a) LDG SH, depo at 15 mN/m, b) LDG:LDG SH 50:50 deposited at 25 mN/m. Red arrow indicate moment where pure ethanol is flowed over the chips, which cause a large change in response, blue arrow indicate moment when a solution of poly-L-proline is flowed over the chips.